OPTICAL MODELING OF AMORPHOUS AND METAL INDUCED CRYSTALLIZED SILICON WITH AN EFFECTIVE MEDIUM APPROXIMATION

THEOPHILLUS FREDERIC GEORGE MULLER

A thesis submitted in partial fulfillment of the requirements for the degree of Doctor Philosophiae in the Department of Physics, University of the Western Cape.

Supervisor: Prof. D. Knoesen, University of the Western Cape

Co-supervisor: Prof. C. J. Arendse, University of the Western Cape

October 2009

To my parents.

ACKNOWLEDGEMENTS

Our Heavenly Father, Who sustains everything.

I am grateful to the following without whose assistance, advice, guidance and friendship this thesis would not have been possible:

My supervisor, Prof. Dirk Knoesen of the Physics Department of the University of the Western Cape (UWC), for giving me this opportunity, his kindness, expertise, guidance, and encouragement is very much appreciated.

Prof. Christopher Arendse, co-supervisor of this thesis, for the guidance, discussions and friendship. Thank you for always insisting on the details.

Prof. Werner van der Weg, formerly of the Debye Institute, Utrecht University, the Netherlands, for cultivating my initial interest in this field of study, and for awarding me the van der Weg scholarship.

Prof. Ruud Schropp, for extending a generous welcome to the Section Nanophotonics in the Debye Institute, and the opportunity to work as a member of his distinguished group.

Prof. Jatin Rath, Debye Institute, Netherlands, for advice and interesting, stimulating discussions.

The National Research Foundation, iThemba Labs and the Physics Department at UWC, for the financial assistance during the course of this investigation. Without the Africa Scholarship from Utrecht University this work would not have been possible.

Prof. Reginald Madjoe, of the Physics Department at UWC, for friendship, training in aspects of metallization, and the mentoring in the teaching environment.

Dr. Sylvain Halindintwali, for being a great team-member through the years, the input, enthusiasm and the lively discussions.

Prof. Robert Lindsay, for the support.

Prof. Catherine Cress and Dr. Roderick Julies for their encouragement.

The late Proffs. Ryno Swanepoel and Igor Krylov, great mentors from whom I have learned much.

Former UWC Physics staff: Prof. Daniel Adams, Prof. Edmund Zingu, Prof. J. R. Botha, Dr. Randall Carollissen and the late Dr. Terrence Marais, for their encouragement and teaching of experimental techniques in the early years.

Former staff at the iThemba Labs Institute, Dr. Rene Pretorius, Dr. Chris Theron, Dr. Vic Prozesky, and Mr. Karl Springhorn for teaching me experimental techniques in the early years.

The fellow students and post-docs in the SID group, section Nanophotonics, Debye Institute: Silvester (Zomer), for all the assistance. Silvester, Jan-Willem, Marites and Rey, Vasco, Hongbo, Hanno, Monica, Yanchao, Jessica, Minne, Arjen, Ruud, Lourens, Gerben and Ronald, for the friendship and the wonderful time. Thanks to Pascal, Joep, Gijs, Diederik, Govert and Timon for their interest.

The supporting and academic staff at Section Nanophotonics, Debye Institute for assistance, advice and extending a hand of friendship: Karine, Caspar, Martin, Arjan, Ruurd, Theo, Wim, Henrik, Roberto, Pedro, Ernst, Arjen. Profuse thanks to Rhiny for always taking care of the details for my visits to their institute.

The friends and colleagues over the years, for their friendship and encouragement: Basil, Ken, Adrian, Danielle, Gerald, Sanobia, Denzel, Rohan, Mornay, Angela, Shirese, Lindy, Shefon, Ivanka and Berneshia.

My fellow students in the group, Messrs. Brian van Heerden, Lebogang (Chester) Kotsedi, Aaron Malape, Clive Oliphant, David (Eddie) Motaung and Francious Cummings for their interest and assistance.

The other post-graduate students of the Physics Department at UWC for their interest, and the undergraduate students for whom we strive.

Owen and the gang, for your encouragement and friendship.

The old friends from way back.

My family, for their encouragement and for believing in me, and for their love:
My mother Eunice and my father William, for all the sacrifices; Alan, Janine, Euan, Kieran, Ilona, Shafiek, Rushney, Liam, Keziah, William, Liezl, Damian, Lindseigh and Grant.

All those who had a bearing on the outcome of this investigation.

DECLARATION

I declare that

"OPTICAL MODELING OF AMORPHOUS AND METAL INDUCED CRYSTALLIZED SILICON WITH AN EFFECTIVE MEDIUM APPROXIMATION"

is my own work and that all the sources used or quoted have been indicated and acknowledged by means of complete references.

Theophillus Frederic George Muller **Date**

Keywords

OPTICAL MODELING OF AMORPHOUS AND METAL INDUCED CRYSTALLIZED SILICON WITH AN EFFECTIVE MEDIUM APPROXIMATION

Theophillus Frederic George Muller

Metal induced crystallization
Polycrystalline silicon
Annealing
Effective medium approximation
Optical modeling
Absorption
Band gap
Phase Transition
Protocrystalline silicon
Structural order

ABSTRACT

'OPTICAL MODELING OF AMORPHOUS AND METAL INDUCED CRYSTALLIZED SILICON WITH AN EFFECTIVE MEDIUM APPROXIMATION '

Theophillus Frederic George Muller

PhD thesis, Department of Physics, University of the Western Cape

Hydrogenated amorphous silicon (a-Si:H) is second only to crystalline silicon in volume manufacturing of solar cells due to its attractive characteristics for solar panel manufacturing. These are lower manufacturing costs, and the fact that it can be deposited on any surface, and in any shape even on flexible substrates. The metal induced crystallization of hydrogenated amorphous silicon has been the subject of intense scrutiny in recent years. By combining the technology of hydrogenated amorphous silicon thin films with the superior characteristics of c-Si material, it is hoped that more efficient solar cells can be produced.

In this thesis we report on the metal-mediated-thermally induced changes of the structural and optical properties of hydrogenated amorphous silicon deposited by hot-wire CVD, where aluminium and nickel were used to induce crystallization. The metal-coated amorphous silicon was subjected to a thermal annealing regime of between 150 and 520°C. The structural measurements, obtained by Raman spectroscopy, show partial crystallization occurring at 350 °C. At the higher annealing temperatures of 450°C and 520°C complete crystallization occurs. Reflection and transmission measurements in the UV-visible range were then used to extract the optical properties. By adopting the effective medium approximation a single optical model could be constructed that could

successfully model material that was in different structural phases, irrespective of metal contamination. Changes in the absorption of the material in various stages of transition were confirmed with a directly measured absorption technique, and the modelled absorption closely followed the same trends

This study forms part of the larger overall solar cell research project, of which the primary aim is to eventually develop a silicon solar panel that optimises the characteristics for best performance.

October 2009

CONTENTS

CHAPTER 1

Introduction

1.1 PHOTOVOLTAICS

The sun derives its energy from the nuclear fusion processes in its core and radiates energy from its surface in the form of electromagnetic waves. The electromagnetic spectrum peaks between wavelengths 200 nm – 3000 nm [1.1], from the ultraviolet to the near infrared range. While the energy of the sun is free and plentiful, the use of solar energy as an environmentally favourable energy source to help address the energy needs of growing economies and to improve the basic living conditions of a growing global population has been a viable option for many years.

In this regard the term photovoltaic refers to the direct conversion of solar energy or sunlight into electrical power by means of a photovoltaic or solar cell. The efficiency of a photovoltaic device is expressed as the ratio of the electrical output power to the incident power from the sun. The efficiencies of real solar cells are however, still low due to various technological limitations relating to the material properties and cell structures. Thin semiconductor films are utilised in place of high quality bulk materials to drive down the manufacturing costs of solar cells while maintaining reasonable efficiencies. Photovoltaic semiconducting materials must be readily available, non-toxic and exhibit a good photovoltaic efficiency with long-term stability. Manufacturing processes must be easy and reproducible and have the potential for large area production [1.2]. Hydrogenated amorphous silicon (a-Si:H) solar cells have fulfilled this role in the past and are still widely manufactured, but due to the Staebler-Wronski effect [1.3], which cause the degradation of electronic properties under exposed solar illumination, the next generation of Si thin film materials such as hydrogenated protocrystalline Si, nano- or-

microcrystalline Si (nc/μc-Si:H) and polycrystalline (pc-Si:H) have been developed. These materials are normally manufactured by chemical vapour deposition (CVD) techniques such as plasma-enhanced (PECVD) or hot-wire (HWCVD) methods. A silicon-containing gas such as silane (plus hydrogen gas sometimes) is used as a source and transformed into plasma or cracked on a metal wire catalyst respectively; by adding quantities of boron or phosphorous-containing gases during the deposition process p or n doped silicon layers can be obtained. The p and n layers have excess holes and electrons as charge carriers, respectively. For a-Si:H more dopant atoms have to be incorporated into the reaction chamber compared to c-Si. The doping efficiency, which is defined as the fraction of the introduced dopant atoms that are electrically active, is very low for a-Si:H, while in c-Si the doping efficiency is of the order of unity. In a-Si:H it can range from 10^{-4} to 10^{-2}, depending on the deposition conditions [1.4].

1.2 AMORPHOUS AND CRYSTALLINE SILICON

The disorder of the atomic structure is the main feature that distinguishes amorphous from crystalline materials, as shown in figure 1.1.

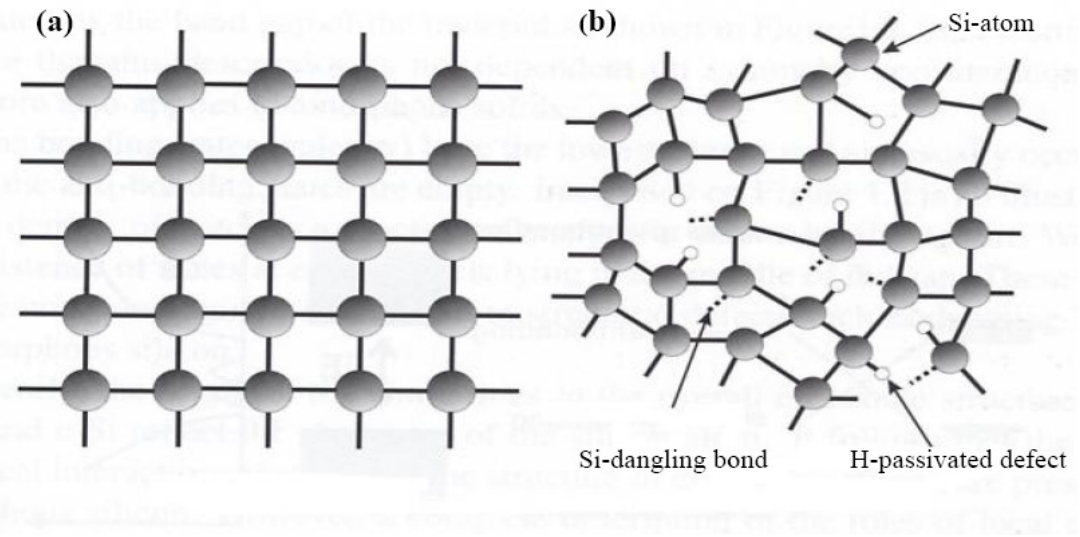

Figure 1.1 Comparison between the structure of (a) c-Si (b) a-Si:H.

This difference in the atomic arrangement in the crystalline and amorphous phases can influence many of the properties of the material. The electrons associated with isolated atoms have a well-defined set of discrete energy levels available to them. In a crystal several atoms are packed closer together and the original individual energy levels spread out and form bands. The density-of-states (DOS) function gives the number of allowed states per energy level. In a perfect crystalline semiconductor, the number of allowed states in the energy gap is zero. In a semiconductor at a temperature of absolute zero its valence band (VB) is completely filled with electrons and the conduction (CB) completely empty. No electrical conduction is then possible; all electrons are bonded to their atoms.

Silicon is covalently bonded overall in both its crystalline and amorphous phases; they tend to have similar overall electronic structure and comparable band gaps. One major difference between the crystalline and amorphous phase is that amorphous silicon (a-Si) has a large number of states in the forbidden energy gap. In the amorphous state short-range order still exists but long-range order has been lost. The large number of states in the gap can be associated with the defects characteristic of the amorphous state, but the density of these defect states depends on the method used to prepare the amorphous film.

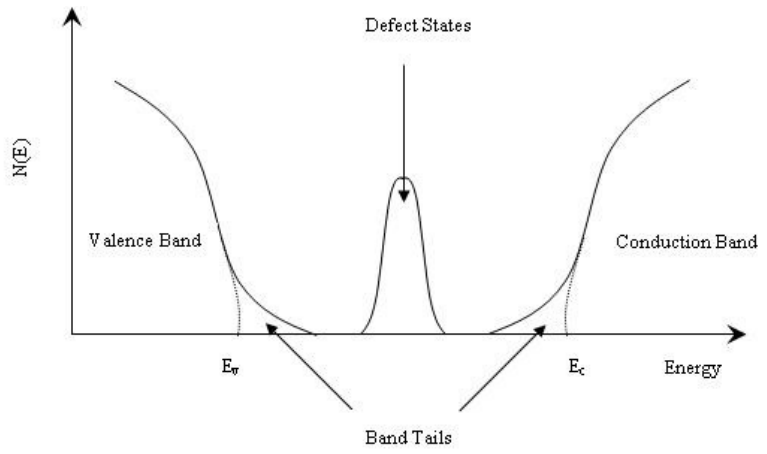

Figure 1.2 Schematic of the DOS of a-Si [1.4]

Because crystalline silicon (c-Si) has an indirect band gap, it necessitates three particles (a photon, electron and phonon) to assist with the excitation of an electron from the VB to the CB; this is necessary to conserve both energy and momentum in the system. The result is a low value for the absorption coefficient, and rather thick and expensive layers are necessary to absorb most of the useful solar radiation. Since the concept of crystal momentum cannot be defined in an amorphous material, it follows that the momentum conservation rule for optical processes does not hold for a-Si. Only a photon and an electron are then required to excite an electron from the VB to the CB. This makes a-Si behave like a direct band-gap semiconductor, leading in turn to a larger value for the absorption coefficient of a-Si compared to c-Si for visible light.

In a-Si each atom also has a possibility of alternative bonding configuration; with the result that fluctuations in the Si-Si bond angles and inter-atomic distances occur. Bond angles in a-Si can deviate up to 10%, or from 7° to 14° from the tetrahedral value of 109.5° [1.4]. The average bond angle variation reflects the degree of structural disorder in the material. Alternative bonding configuration also causes the broadening of the VB and CB edges; and the states that are formed by the broadening of the edges are known as tail states as shown in figure 1.2. The presence of the band tails is caused by the disorder of the amorphous material, i.e. defects due to stretched and weak bonds and departures from standard bond lengths and angles that affect the transport of carriers in amorphous silicon. The abundance of defect states in the band gap is caused by unsaturated or dangling bonds, corresponding to atoms missing a neighbour, at those sites where periodicity is lost, and by the incorporation of foreign atoms that are substituted into the network. These dangling bonds can act as recombination centres for the electrons and holes and thereby diminish the electronic properties of the material. In pure a-Si the dangling bond density is of the order of 10^{20} cm^{-3} [1.4 - 1.5]. The high defect density makes it impossible to change the position of the Fermi-level by introducing foreign atoms that have either a shortage or excess of electrons that can act as charge carriers. Only by introducing hydrogen into the amorphous silicon network, can the dangling bonds be saturated or passivated. Monovalent hydrogen bonds to the dangling bonds, and

the resulting material is then known as hydrogenated amorphous silicon (a-Si:H). The effect of the hydrogen is such that the electrons of the a-Si:H can be controlled to make the alloy a conducting material; the defect density of the new material reduces by several orders of magnitude to about 5×10^{15} cm^{-3} in material that contains ~ 10 at.% hydrogen.

The structure of a-Si:H appears to consist of voids embedded in the amorphous network with boundaries that are covered with hydrogen. Device-quality a-Si:H has a void fraction of only 1%, while material with poor opto-electronic properties have void fractions of ~ 20% [1.6]. The voids are of diameter ~ 10Å [1.4]. The hydrogen also influences the band gap: in a-Si:H the band gap can vary from 1.6 eV to 1.8 eV, since the band gap varies with hydrogen concentration [1.7]. The band gap of c-Si is 1.1 eV [1.8]. Further deterioration in the transport of the carriers is caused by the light-induced creation of metastable defects. Due to the presence of weak Si-Si bonds (strained bonds) and the relative ease of diffusive motion of hydrogen, metastable dangling bonds can be created by the breaking of the weak bonds. This is in addition to the dangling bond density initially present; and the effect is known as the Staebler-Wronski effect [1.3] after its discoverers. The creation of the metastable defects is enhanced by the illumination of the material and the light-induced change manifests itself as a shift of the Fermi-level towards mid-gap, and is accompanied by a reduction of the dark- and photoconductivity. Upon illumination the material has a roughly one order of magnitude-higher concentration from the as-deposited dangling bonds initially present in device-quality material, which reduces the lifetime of the free carriers significantly. Solar cell performance characteristics deteriorate as a result of the enhancement of the recombination losses that occur. The 10^{17} cm^{-3} defect concentration at which the Staebler-Wronski effect saturates does impose a limitation to the maximum obtainable conversion efficiency in an a-Si:H based solar cell and is still an important drawback in hydrogenated amorphous silicon technology. However, the excess defects can be removed by the thermal annealing of the material from 1 to 3 hours at a temperature above 150 °C. To reduce the degradation of the as-deposited a-Si:H a low hydrogen content in the material is suggested; combined with a favourable microstructure. Hydrogen dilution during the growth process has also been used to obtain more stable

materials and solar cells to reduce the possible degradation of the material [1.7]. It is generally believed that excess hydrogen in the chamber passivates the dangling bonds at the growing surface of the film thus allowing the impinging species more time to find favourable sites. The resulting structure would therefore be more ordered.

Hydrogenated μc-Si is a two-phase amorphous and crystalline mixture with < 20 nm size crystallites embedded in the amorphous network, while hydrogenated polycrystalline silicon (pc-SiH or poly-Si:H) is single-phase crystalline with grain boundaries and crystallites > 20 nm for the smallest crystal dimension. Most hydrogen atoms are incorporated at grain boundaries or grain boundary tissue [1.9]. In microcrystalline Si the crystalline part makes the material more crystal-like as far as absorption is concerned, and the material exhibits smaller optical absorption than a-Si due to the indirect band gap component. The microcrystalline silicon, though, is quite efficient in absorbing the long-wavelength photons [1.10]. Intrinsic pc-Si:H solar cells benefit from absorption of photons with energies in the range 1.1 eV to 1.75 eV, where most a-Si:H shows little or no response.

1.3 SOLAR CELLS

The operation of solar cells is based on the formation of a junction between two dissimilar materials in terms of photoelectric properties [1.11]. The simplest junction is in the form of the p-n junction, an interface between n- and p- regions of one semiconductor. The material develops a strong electric field when the two pieces (n- and p-) are brought into contact; electrons from the n-region near the interface diffuse into the p-side, leaving behind a layer which is positively charged by the donors. Similarly, holes diffuse in the opposite direction, leaving behind a negatively charged layer stripped of holes. This results in a boundary region that contains practically no mobile charge carriers, and is known as the depletion region. This charge distribution results in an electric field in the junction. Incident light generates electron-hole pairs on both sides of the junction, in the n-type emitter and in the p-type base. The generated charge carriers – positive holes and negative electrons are swept apart by the electric field and diffuse over

the junction, thus producing an electric current across the device. The electrical current that is generated in the semiconductor is extracted by contacts at the front and rear of the cell. Basic solar cells, as shown in figure 1.3, consist of single crystalline or polycrystalline material that contains a thin n-type layer (emitter) on a p-type substrate (base). A thin layer of anti-reflective coating is used to maximize photon collection and minimize light reflection from the top surface. The charge exits the device through contacts on the p- and n-sides of the device and an external current is generated. Upon illumination the top contact structure allows light to pass through so that the photons can be absorbed by the semi-conducting material. The absorption of photons of energy just higher or equal to the band gap cause the electrons in the material to be excited from the valence to the conduction band and leave a hole in the valence band. The efficiency η of a solar cell is measured at maximum power under standard test conditions, 100 mW/cm^2, standard reference AM 1.5 spectrum, and temperature 25°C.

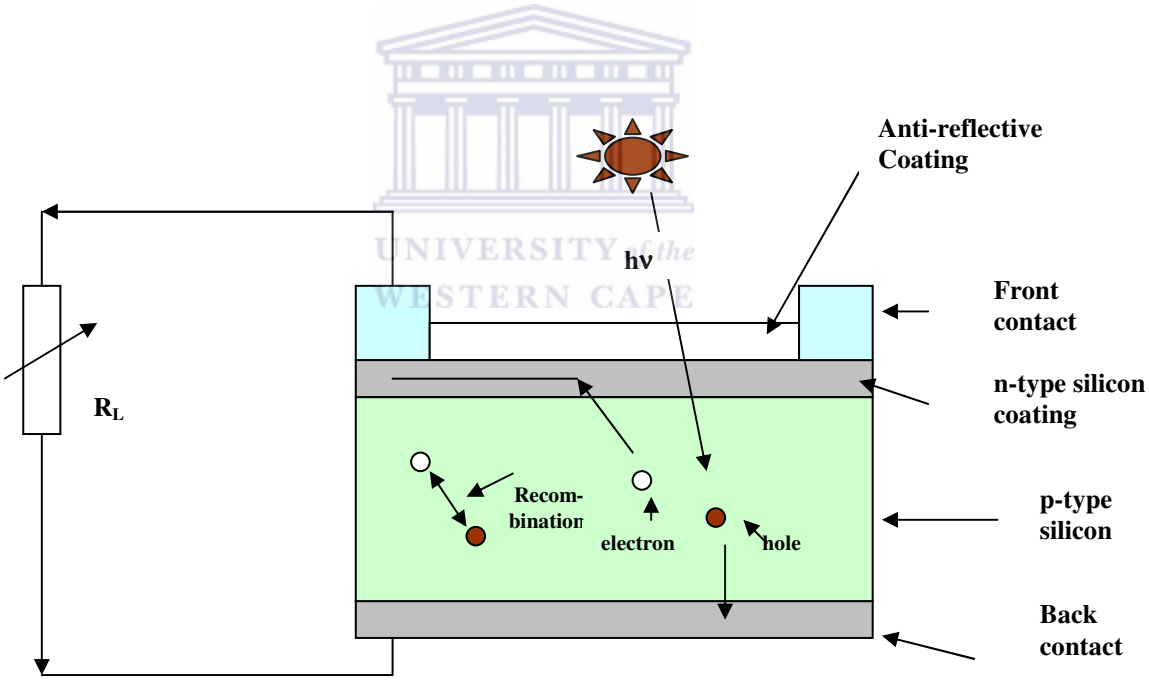

Figure 1.3 A schematic of a basic crystalline silicon solar cell.

For a-Si:H solar cells the cell thickness necessary to absorb the solar radiation can be much smaller than for c-Si, but the simple structure of the c-Si solar cell is not feasible;

this is due to the highly defective doped layers containing a large number of dangling bonds resulting in the shortening of the mean free path of the charge carriers owing to the presence of the recombination centers (dangling bonds). The solution is to sandwich an intrinsic layer between the n- and p-layers to serve as the active layer where light collection and charge separation can take place. Because the carriers can move only a short distance before they recombine, the cell thickness has to be small to collect the photo-generated carriers efficiently. The p- and n-layers serve to produce an internal electric field over the intrinsic layer, and the orientation of the field is such that the carriers, generated in the depletion region, are strongly attracted towards the region in which they are the majority carriers. The generated carriers are collected due to the large electric field. It is preferable to have light enter the cell through a very thin p-type layer so that the region of maximum photo-generation in the i-layer is also the region of highest electric field, between the heavily doped p-layer and the intrinsic layer. A transparent conducting oxide (TCO) contact layer covers the p-layer and a metal (ohmic) contact layer covers the n-layer.

1.4 INDUCED CRYSTALLIZATION

In our context the term ‘phase change’ refers to the transition from the amorphous to crystalline phase if the necessary thermal energy is available. Such a process is inhibited by the activation barrier; in the case of the transition from amorphous to crystalline phase the covalent bonds of the Si atoms need to be broken and rearranged. The reduction of the Gibbs free energy of the system plays an important role in this thermodynamic process to obtain the new thermodynamically favourable crystalline phase. Under moderate heating conditions, a-Si transforms directly into c-Si. Under rapid heating conditions, a-Si, if heated above its melting temperature, transforms to the metallic liquid state (l-Si) [1.12]. Upon cooling, this phase solidifies to either the amorphous or the crystalline phase, depending on the quench rate [1.13] and the presence of a seed for crystallization [1.14]. The kinetics of phase change models [1.15] assumes the existence of germ nuclei which become growth nuclei at a certain nucleation rate. Further, the phase transition takes

place at a certain growth rate until nucleation ends and neighbouring growth nuclei collide such that further growth is limited.

The preparation of thin large-grained polycrystalline silicon (poly-Si) films on inexpensive glass substrates for large area electronics such as solar cells is now becoming increasingly important, as on the long term thin film technology with absorber thicknesses of a few μm will lead to significant cost reductions. Already μc-Si:H by PECVD or HWCVD, consisting of nano-sized columnar crystallites perpendicular to the substrate, with width of ~ 100 nm is used in solar cells with reasonable efficiencies of ~ 10% . But it is still difficult to deposit crystalline silicon from the gas phase with grain size larger than cell thickness, which is the ideal. Polycrystalline cells with such grain sizes will combine the benefits of established crystalline silicon wafer technologies with thin film technology and lead to establishing cell efficiencies that can rival the more expensive wafer technology efficiencies of ~ 15% [1.16].

Now, solid phase crystallization (SPC) refers to the crystallization of deposited amorphous Si layers on a substrate, while re-crystallization refers to the crystallization of previously amorphized (by ion-implantation) layers of a c-Si wafer. Instead of plain, direct deposition, polycrystalline silicon by SPC or crystallization by laser annealing has so far also been investigated for thin film transistor and solar cell applications [1.17 – 1.18]. Films transformed by SPC yield grain sizes of the order of the film thickness, 1 μm, and long annealing times are the order of the day. Such a layer can function as a template for further, subsequent epitaxial growth of the absorber layer by other techniques [1.16]. It is referred to as a seed layer.

Due to the specific constraints in the crystallization methods (i.e. they are expensive) an alternative technique, Metal Induced Crystallization (MIC) was developed that offered the attractive advantages of fast crystallization times at low temperatures on cheap substrates using simple equipment [1.19]. The annealing process normally occurs in vacuum, or under air, nitrogen and other gas atmospheres. Eutectic and compound-forming metals, upon interaction with the silicon and subsequent crystallization thereof,

result in silicon alloys and compounds as by-products respectively. One such method is aluminum-induced crystallization (AIC) of amorphous silicon (a-Si), one of a few metal-induced crystallization (MIC) processes. It is based on the annealing step which transforms, for example, an initial glass/Al/a-Si stack into a glass/poly-Si/Al(Si) structure at temperatures below the eutectic temperature of the Al/Si system (T_{eu} = 577 °C). Layered sequences such as substrate/a-Si/Al/a-Si at reduced temperatures [1.20] and Al evaporated on top of the amorphous silicon [1.21] have also been investigated. In figure 1.4 a possible mechanism for a substrate/a-Si/Al system is illustrated. Si films deposited by various methods have been successfully crystallized. It was shown [1.22] that a thin oxide layer between the initial Al and a-Si layer is required for the aluminum-induced layer exchange; the oxide layer acts as a permeable barrier and has pronounced influence on the kinetics of the process. The role of the oxide film is to determine the Si transport across the Si—Al interface that controls the nucleation process and thus the size of the Si grains [1.23]. Adjacent Al and Si layers of similar thickness exchange layer positions [1.24]. The layer exchange occurs during isothermal annealing at temperatures significantly below the eutectic temperature of 577 °C and results in the growth of large-grained poly-Si films. The overall layer exchange of the Si and the Al films is influenced by the following parameters [1.25]: (i) temperature, (ii) ratio of layer thicknesses, (iii) annealing time, (iv) polycrystalline nature of the aluminum, (v) layer sequence and (vi) the interface between the Al and a-Si layers. Ottaviani *et al.* [1.26] described the steps in the eutectic system as (i) dissociation of the silicon atoms from the amorphous phase into the metal, (ii) diffusion of silicon atoms through the metal, and (iii) crystallization of the dissolved silicon by either nucleation of clusters or agglomeration on existing crystallites.

Energetically, the driving force is the higher Gibbs energy of the amorphous phase compared with the crystalline phase. The faster crystallization is due to the kinetically fast reaction path where the metal serves as solvent medium for the amorphous material and as catalyst. Aluminum as example forms a shallow acceptor 0.067 eV above the valence band [1.1]. This heavily doped p^+ layer can be used as the back-contact of a solar cell structure, as proposed in the scheme glass/poly-Si(p^+)/poly-Si(p)/a-Si:H(n^+)/TCO as solar cell structure in figure 1.5 [1.16].

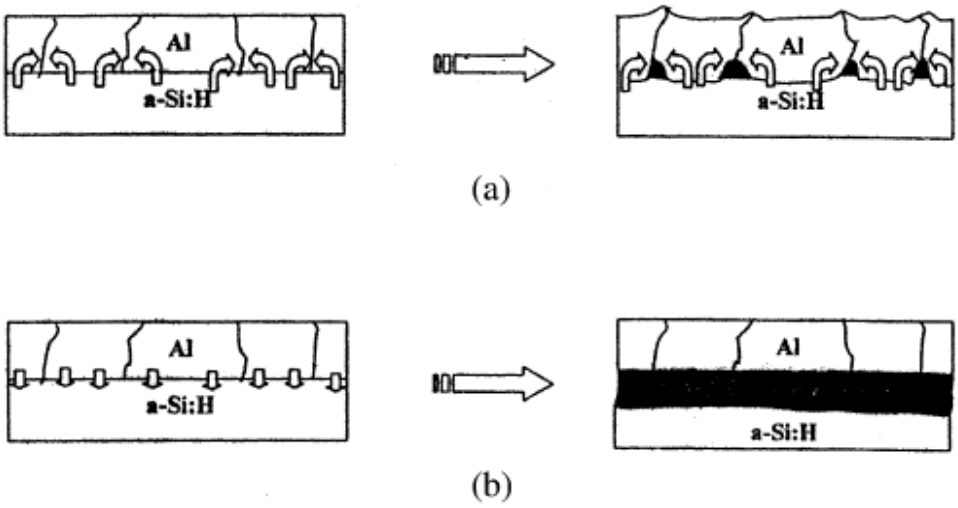

Figure 1.4 Diagram sketching possible mechanism of Al/a-Si interaction [1.27].

The Toyota group has fabricated a solar cell with almost similar structure by using a silane-free process. Even though the measured efficiency was only 0.005% their modeling has shown that the simulated efficiency could be a high as 13% in single junction cells if impurities can be suppressed and the cell parameters optimized [1.28].

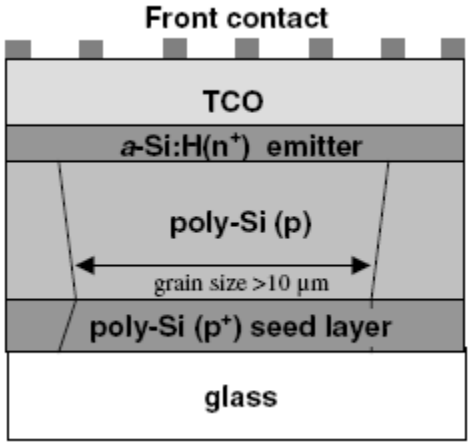

Figure 1.5 Scheme of polycrystalline Si thin-film solar cell [1.16].

Ni is an example of a compound-forming metal. Ni in contact with silicon, will probably form a thin layer of NiSi, but mostly the $NiSi_2$ phase will be formed. The chemical potential for Ni is lower at the $NiSi_2$/a-Si interface than at the $NiSi_2$/c-Si interface, thus the Ni diffuses to the a-Si side while at the same time Si diffuses in the opposite direction. The silicide phase thus moves through the a-Si and leaves crystalline Si behind [1.29], as schematically illustrated in figure 1.6.

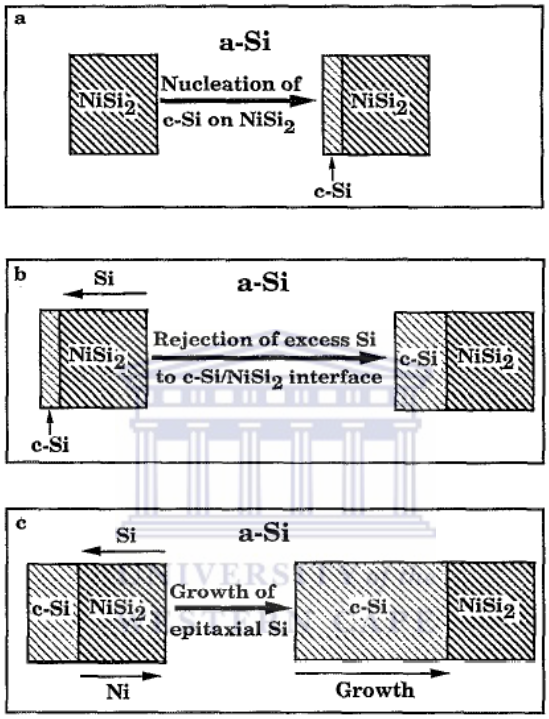

Figure 1.6 Possible growth mechanism of c-Si at the $NiSi_2$/a-Si interface [1.29].

The non-eutectic metals can be used in metal-induced lateral crystallization (MILC) processes, where the a-Si crystallizes in a lateral direction as well [1.30]. The silicides remain in the film while the metal in the eutectic/Si system can be removed. Ni creates deep level acceptor levels at 0.230 eV above the valence band and at 0.350 eV below the conduction band in c-Si [1.31]. Thus Ni enhances carrier recombination and strongly decreases the minority carrier lifetime. In photovoltaic application the photogenerated

minorities make minority carrier life time crucial for good solar cells. Thus Al is preferred over Ni in photovoltaic applications [1.32].

1.5 AIMS AND OUTLINE

In the investigation the a-Si:H films were deposited using the HWCVD process. The MIC process has been extensively performed in laboratories worldwide, and has found application in semiconducting devices already. However, scant attention has been paid to the important optical properties, even if the material is earmarked for inclusion in photovoltaic devices. This work therefore aims to develop a generic technique in order to extract the optical properties of crystallized silicon thin films produced by the MIC technique, irrespective of the metal used as catalyst.

A brief overview of the analysis techniques used, namely Optical Transmission and Reflection, FTIR, XRD, Raman Scattering and Conductivity analysis are given in chapter 2. A detailed theoretical background of the major technique used to extract the optical properties is given such that the major precepts are placed in context when building optical models. In chapter 3 the material properties of μc-Si:H films under the influence of a variation in hydrogen dilution are explored and discussed. The building of an optical model is discussed that led to the inclusion of voids and crystallites; this forms the frame for a successive model in a later chapter on MIC Si:H thin films.

In chapter 4 the same model as in chapter 3 is used to investigate thermally annealed proto-Si:H under the same annealing regime as the later MIC films. Changes in the structure of these films are discussed and correlated with the optical properties. Chapter 5 discusses the effects and results of the MIC process fully, with regards to structural and optical properties. Differences between the application and products obtained with aluminum and nickel as catalyst metals are highlighted. Finally, the investigation is summarized in Chapter 6.

REFERENCES

1.1 S.M. Sze, in 'Semiconductor Devices', John Wiley & Sons, New York (1985)

1.2 A.Goetzenberger, C. Hebling, Solar Energy Materials & Solar Cells 62, (2000) 1

1.3 D. L. Staebler and C. R. Wronski, Appl. Phys. Lett. 31, (1977) 292

1.4 R. A. Street, in 'Hydrogenated Amorphous Silicon', Cambridge Solid State Science Series, Cambridge (1991)

1.5 W.E. Spear and P.G. Lecomber, Phil. Mag. 33, (1976) 935

1.6 M. J. van den Boogaard, PhD Thesis, Utrecht University, Utrecht, The Netherlands (1992)

1.7 H. Meiling, PhD Thesis, Utrecht University, Utrecht, The Netherlands (1991)

1.8 T. Markvart, in 'Solar Electricity', John Wiley & Sons, Chichester (2000)

1.9 R Schropp and M Zeman, in 'Amorphous and microcrystalline silicon solar cells: Modeling, materials and device technology', Kluwer academic publishers, Boston (1998)

1.10 J. Meier, R. Fluckiger, H. Keppner and A. Shah, Appl. Phys. Lett. 65, (1994) 860

1.11 R. J. van Overstraeten and R. P. Mertens, in 'Physics, Technology and Use of Photovoltaics', Modern Energy Studies, Adam Hilger Ltd., Bristol and Boston (1986)

1.12 O. Thompson, G. J. Galvin, J. W. Mayer, P. S. Peercy, J. M. Poate, D. C. Jacobson, A. G. Cullis and N. G. Chew, Phys. Rev. Lett. 52, (1984) 2360

1.13 O. Thompson, J. W. Mayer, A. G. Cullis, H. C. Webber, N. G. Chew, J. M. Poate and D. C. Jacobson, Phys. Rev. Lett 50, (1983) 86

1.14 'Laser Annealing of Semiconductors', editors M.Poate and J. W. Mayer, (Academic Publishers, New York (1982)

1.15 M. Castro, F. Dominguer-Adame, A. Sanchez, T. Rodriquez, Appl. Phys. Lett. 75(15), (1999) 2205

1.16 W. Fuhs, S. Gall, B. Rau, M. Schmidt, J. Schneider, Solar Energy 7, (2004) 961

1.17 D. Toet, B. Koopmans, R.B. Bergmann, B. Richards, P.V. Santos, M. Albrecht, J. Krinke, Thin Solid Films 296, (1997) 49

1.18 G. Fortunato, L. Mariucci, R. Carluccio, A. Pecora, V. Foglietti, Applied Surface Science 154–155, (2000) 95

1.19 D. Dimova-Malinovska, J. Optoelectronics and Advanced Materials 7(1), (2005) 99

1.20 S. R. Stiffler, M. O. Thompson and P. S. Peercy, Phys. Rev. Lett. 60, (1988) 2519

1.21 G. Radnoczi, A. Robertsson, H. T. G. Hentzel, S. I. Gong, M. –A. Hasan, J. Appl. Phys. 69 (9), (1991) 6394

1.22 S. Gall, J. Scheider, M. Muske, I. Sieber, O. Nast, W. Fuhs, Proccedings of the 18th European Photovoltaic Solar Energy Conference, Rome, Italy (2002) 87

1.23 J. Scheider, J. Klein, M. Muske, S. Gall, W. Fuhs, J. Non-Cryst. Sol. 338 – 340, (2004) 127

1.24 O. Nast, T. Puzzer, L. M. Koschier, A. B. Sproul and S. R. Wenham, Appl. Phys. Lett. 73, (1998) 3214

1.25 O. Nast, A. J. Hartmann, J. Appl. Phys. 88 (2), (2002) 716

1.26 G. Ottaviani, D. Sigurd, V. Marrello, J. W. Mayer, J. O. McCaldin, J. Appl. Phys., 45(4), (1974) 1730

1.27 A. M. Al-Dhafiri, H. A. El-Jammal, A. Al-Shariah, H. A. Naseem, W. D. Brown, Thin Solid Films 422, (2002) 14

1.28 T. Ito, H. Fukushima, M. Yamaguchi, Solar Energy Materials and Solar Cells 83, (2004) 91

1.29 C. Hayzelden, J. l. Batstone, J. Appl. Phys. 73(12), (1993) 8279

1.30 Z. Jin, G. A. Bhat, M. Yeung, H. S. Kwok, M. Wong, J. Appl. Phys. 84(1), (1998) 194

1.31 H. Kitagawa, S. Tanaka, H. Nakashima, M. Yoshida, J. Electr. Mat. 20(6), (1991) 441

1.32 J. M. Schneider, PhD Thesis, Berlin Technical University, Berlin (2005)

CHAPTER 2

Experimental Methods

2.1 DEPOSITION EQUIPMENT

The amorphous silicon thin films were deposited in the multi-chamber high vacuum deposition system known as PASTA (process equipment for amorphous silicon thin-film applications) [2.1] at the Surfaces, Interfaces and Devices group at the Debye Institute, Utrecht University. It is an interconnected, five chamber system allowing for the transport of samples during the different stages of deposition of doped and intrinsic layers to manufacture a solar cell. The background pressure in all the chambers is kept at ~ 10^{-8} mbar. Depositions of p, intrinsic and n type PECVD layers, and intrinsic and n-doped HWCVD layers can be performed. The samples used in this study were intrinsic HWCVD protocrystalline a-Si:H, abbreviated proto-Si:H. The intensive study of M. van Veen [2.2] led to the establishment of optimum deposition conditions for proto-Si:H; typically, the substrate temperature is around 250°C. Further details of the deposition process and parameters are also given in her study.

For this study Corning 2000 glass and (100) c-Si substrates were used as substrates during the deposition process. The proto-Si:H thin films were metalized in a thermal evaporation chamber. After sectioning the samples in smaller pieces they were annealed in a conventional tube furnace with continous nitrogen flow in order to produce crystallized silicon via the metal induced crystallization method (MIC).

2.2 ANALYTICAL TECHNIQUES

2.2.1 OPTICAL ANALYSIS

2.2.1.1 INTRODUCTION

Hydrogenated amorphous silicon, and by extension nano/micro and polycrystalline silicon are important materials for the manufacturing of photovoltaic devices. Since it is important to understand the optical behaviour of a device it is normal to measure the reflection spectrum and/or the transmission optical spectrum of the thin film. The index of refraction and the absorption coefficient of amorphous silicon can be determined as functions of the wavelength λ, by performing calculations on the transmission/reflection spectrum data of the thin silicon at photon energies in the range from 1.3 – 3.1 eV; i.e. from ultraviolet through visible to near-infrared light. This in turn leads to the establishment of the energy gap of the material, and other optical characteristics of the material.

For hydrogenated amorphous silicon the values of the optical functions are strongly dependent on the material properties that are in turn determined by the deposition conditions. Hence unique values for the optical functions, as in the case of crystalline silicon, cannot be obtained. In fact, the optical functions can more conveniently be described in terms of the preparation conditions which are readily controlled. This can also be extended to nano/microcrystalline silicon, while the treatment to obtain the polycrystalline silicon material can also be important if it is not directly deposited.

2.2.2.2 THEORY

Interaction of electromagnetic radiation with solids

An overview of the basic theory of the interaction of radiation with a solid is necessary in order to appreciate the elements that constitute an optical model when extracting the properties of the silicon thin films. The overview is taken from reference 2.3.

Some solids are transparent and some opaque. Some solids surfaces can be strongly reflecting whilst others tend to absorb incident radiation, depending on the frequency of radiation. Electromagnetic waves are solutions of Maxwell's equations. By disregarding magnetic effects, $\mu = 1$ and these equations can be written as:

$$\begin{aligned} \nabla \times \vec{H} &= \frac{\varepsilon}{c}\frac{\partial \vec{E}}{\partial t} + \frac{4\pi\sigma}{c}\vec{E}, \\ \nabla \cdot \vec{E} &= 0, \\ \nabla \times \vec{E} &= -\frac{\mu}{c}\frac{\partial \vec{H}}{\partial t}, \\ \nabla \cdot \vec{H} &= 0 \end{aligned} \qquad (2.1)$$

where H is the magnetic field, E the electric field, ε the product of permittivity ε_0 of vacuum multiplied by a dimensionless number ε_r called the relative permittivity, and $\mu = \mu_r\mu_0$ the magnetic permeability, while c is the speed of light in a vacuum. The difference between propagation in free space and propagation in the solid is expressed by the two coefficients ε and σ, which are called the dielectric constant and conductivity respectively. The dielectric constant defines the magnitude of the displacement currents due to time variation of E and the conductivity is a measure of real currents created by the electric field. The magnetic field may be eliminated between these equations such that

$$\nabla^2 \vec{E} = \frac{\varepsilon}{c^2}\frac{\partial^2 \vec{E}}{\partial t^2} + \frac{4\pi\sigma}{c^2}\frac{\partial \vec{E}}{\partial t} \ . \tag{2.2}$$

This represents a wave propagated with dissipation. If we choose the frequency, ω, and write

$$\vec{E} = \vec{E}_0 \exp\{i(\vec{K}\cdot\vec{r} - \omega t)\}, \tag{2.3}$$

then our wave equation requires

$$-\vec{K}^2 = -\varepsilon\frac{\omega^2}{c^2} - \frac{4\pi i\omega\sigma}{c^2},$$

which is more conveniently expresses as

$$K = \frac{\omega}{c}\left(\varepsilon + \frac{4\pi\sigma i}{\omega}\right)^{\frac{1}{2}}. \tag{2.4}$$

Thus, in general the propagation constant K is a complex number. In free space we should have

$$K = \frac{\omega}{c}\ , \tag{2.5}$$

as for a wave traveling with the velocity of light. In the medium the velocity is modified such that the phase velocity is divided by a complex refractive index

$$N = \left(\varepsilon + \frac{4\pi\sigma i}{\omega}\right)^{\frac{1}{2}}. \tag{2.6}$$

The whole theory of the optical properties, as observed macroscopically, can be expressed in terms of N. For example if we have a disturbance of frequency ω trying to propagate as a plane wave in the z-direction, and

$$N = n + ik \tag{2.7}$$

for the real and imaginary parts of N, then the propagation constant becomes

$$K = \frac{n\omega}{c} + \frac{ik\omega}{c} \tag{2.8}$$

so that the wave becomes

$$\vec{E} = \vec{E}_0 \exp\left\{ i\omega\left(\frac{nz}{c} - t \right)\right\} \exp\left(-\frac{k\omega z}{c} \right). \tag{2.9}$$

The velocity is reduced to c/n, and the wave is damped, as it progresses, by a fraction $\{ \exp(-2\pi k/n) \}$ per wavelength.

The damping of the wave is associated with the absorption of electromagnetic energy. To calculate the energy Maxwell's equations are used to find the current density associated with the damped wave. This is the right hand side of the first equation

$$\vec{J} = \left(-\frac{i\omega\varepsilon}{c} + \frac{4\pi\sigma}{c} \right)\vec{E}$$

$$= -\frac{i\omega}{c} N^2 \vec{E}. \tag{2.10}$$

The rate of production of Joule heat is the real part of

$$\vec{J}\cdot\vec{E} = -\frac{i\omega}{c}N^2E^2. \tag{2.11}$$

Thus the absorption coefficient – the fraction of energy absorbed on passing through unit thickness of the material is given by

$$\eta = \frac{\mathrm{Re}\left(\vec{J}\cdot\vec{E}\right)}{\left|\vec{E}\right|^2} = \frac{2nk\omega}{c}. \tag{2.12}$$

The situation where radiation is incident upon a plane surface as in the case of normal incidence uses a solution of Maxwell's equations having the form of the damped wave inside the medium, but matched to an incident and reflected wave outside. Thus, for z > 0

$$E_x = E_0\exp\{i\omega(Nz/c - t)\}, \tag{2.13}$$

whilst for z < 0, in the free space outside,

$$E_x = E_1\exp\{i\omega(z/c - t)\} + E_2\exp\{-i\omega(z/c + t)\}, \tag{2.14}$$

corresponding to a wave of amplitude E_1, traveling to the right and a wave of amplitude E_2, traveling to the left. On the boundary

$$E_0 = E_1 + E_2. \tag{2.15}$$

There are also magnetic fields associated with these waves, with magnetic vector in the y-direction for example. By applying Maxwell's equations to calculate H_y for example, the waves at the boundary can then be described as:

$$NE_0 = E_2 - E_1 \tag{2.16}$$

when matched to the wave outside. Thus, the ratio of the complex amplitudes of the reflected and incident waves is

$$\frac{E_2}{E_1} = \frac{1-N}{1+N}, \tag{2.17}$$

which corresponds to a real reflection coefficient,

$$R = \left|\frac{1-N}{1+N}\right|^2 = \frac{(n-1)^2 + k^2}{(n+1)^2 + k^2} \tag{2.18}$$

in terms of the real and imaginary parts of the complex refractive index N.

Independent measurement of the reflection coefficient and of the absorption coefficient is sufficient to fix the values of n and k. These are, therefore, the optical constants which are normally used. In practice the experiments may be much more complicated e.g. reflection at an angle to the surface, or transmission through a thin film, but the results ought, in principle all to be described by these two coefficients. However, the coefficients n and k are not quite independent of one another, they are linked by dispersion relations. The quantity N^2 is an example of a generalized susceptibility, α, in a relation like

$$D = \alpha E \tag{2.19}$$

between a generalized 'displacement' D and a 'force' E. When a linear relation of this kind is considered as a function of frequency – that, as a function of time – it must satisfy the requirements of causality; there must be no displacement until after the application of the force. This condition requires that the real and imaginary parts of the complex function

$$\alpha(\omega) = \alpha_1(\omega) + i\alpha_2(\omega) \tag{2.20}$$

should satisfy the Kramers-Kronig relations

$$\alpha_1(\omega) = \frac{2}{\pi}\int_0^\infty \frac{\omega'\alpha_2(\omega')d\omega'}{\omega'^2-\omega^2} + const.$$

and

$$\alpha_2(\omega) = -\frac{2\omega}{\pi}\int_0^\infty \frac{\alpha_1(\omega')d\omega'}{\omega'^2-\omega^2}. \qquad (2.21)$$

In our case, the real and imaginary parts of N^2 are

$$N^2 = (n^2 - k^2) + 2nki\,, \qquad (2.22)$$

so that we have the conditions

$$n^2(\omega) - k^2(\omega) = \frac{2}{\pi}\int_0^\infty \frac{\omega' 2n(\omega')k(\omega')d\omega'}{\omega'^2-\omega^2} + const$$

and

$$2n(\omega)k(\omega) = -\frac{2\omega}{\pi}\int_0^\infty \frac{\{n^2(\omega') - k^2(\omega')\}d\omega'}{\omega'^2-\omega^2}. \qquad (2.23)$$

In each integral the principal part is taken. From these relations, if we know, say, the absorption coefficient as a function of frequency for all frequencies, then we can evaluate both n(ω) and k(ω) separately.

Extraction of optical functions

Computational methods for obtaining the expressions for the optical parameters were first developed by Tomlin *et al.* [2.4 – 2.5]. A very useful method to extract the important optical parameters [2.6 – 2.7] of the amorphous silicon layer can be used for standard UV-Vis reflection and transmission spectra. For transmission the light is incident normal to the sample surface. The sample consists of a thin layer of thickness d, on a finite

transparent substrate that has a thickness several orders of magnitude larger than d, as shown in figure 2.1:

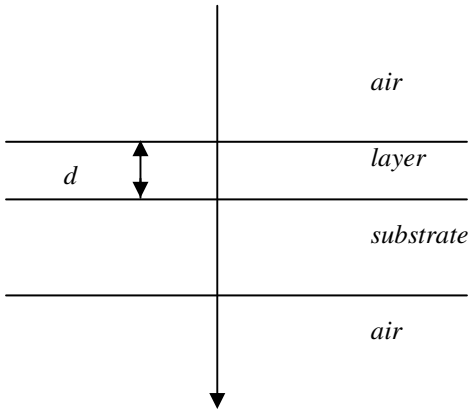

Figure 2.1 General case of light incident on thin film and thick finite substrate.

In such a set-up it can be assumed that the thin film layer is uniform and homogenous, while the transparent, thick and finite substrate is non-uniform. The light is incident from the side of the thin film, where the ambient medium is atmospheric air with refractive index 1. This represents the actual case where a-Si:H is in the form of a uniform thin film on a transparent substrate, with the transmission spectrum displaying an interference pattern due to the a-Si:H layer alone. The optical functions can be determined from the transmission spectrum T(λ) as measured with a spectrophotometer.

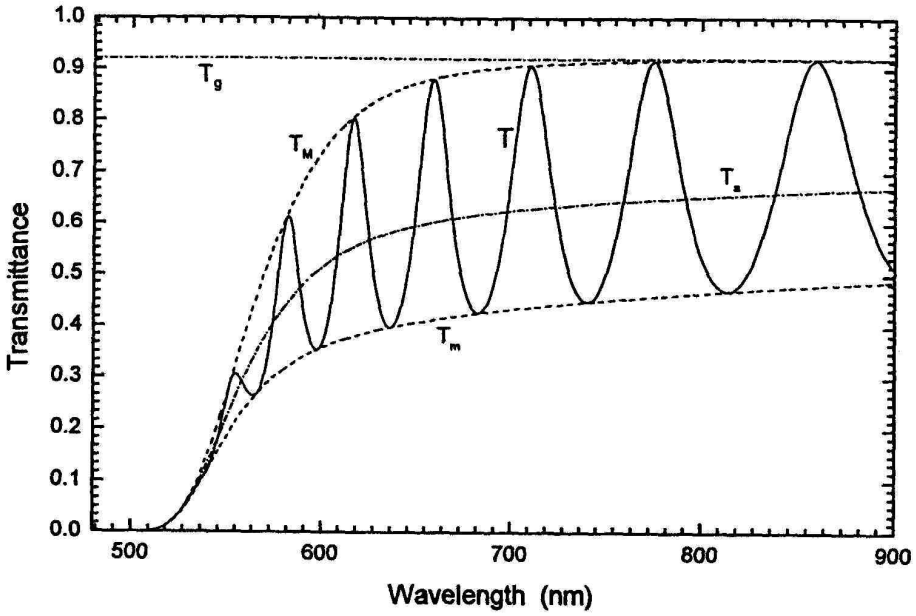

Figure 2.2 A typical transmission spectrum of a thick non-uniform film [2.7]

In figure 2.2 the maxima and minima points of the typical transmission spectrum are connected by the maxima and minima envelopes, respectively, according to the Swanepoel method [2.7]. The optical characteristics of the layer and substrate are described by their complex index of refraction, $\mathbf{n_1} = n_1 - \mathbf{i}k_1$ for the film and $\mathbf{n_2} = n_2 - \mathbf{i}k_2$ for the substrate. The real parts of the expressions are called the refractive index and the imaginary parts are called the extinction coefficients respectively. The extinction coefficient is related to the absorption coefficient α by $I = I_0 e^{-\alpha/x}$ and $\alpha = 4\pi\frac{k}{\lambda}$, where α is defined in terms of the intensity at depth x in the film, when the intensity at the surface x = 0 is I_0.

Thickness inhomogeneity features can also be resolved by an adaptation of the method [2.8]. However, once other inhomogeneities like crystallites and foreign particles with different dielectric functions materials are present in the material alternative methods need to be utilized. The most applicable of the methods make use of effective media theories (EMT's).

Effective medium approximation

The objective of effective-medium theory is to determine the optical properties of heterogeneous or composite systems that can be more accurately described as mixtures of separate regions of two or more materials, each with its own dielectric identity [2.9]. We assume that the characteristic dimensions of the microstructure are large enough (≥ 10 – 20 Å) so that individual regions essentially retain bulk dielectric response. The microstructure, should however be small (≤ 0.1 – 0.2λ) compared to the wavelength of light. The macroscopic electric and magnetic fields of Maxwell's equations will not vary appreciably over any single region.

If a material consists of separate regions, each with their own dielectric functions and the sizes of the regions are small compared to the wavelength of light, then the materials can be considered as a uniform effective medium [2.10]. It will have an equivalent uniform dielectric function by taking into account the effect of screening charges that accumulate on boundaries between microscopically different regions of a composite material. Suppose that the total fraction of materials a and b in a sample are f_a and f_b , where

$$f_a + f_b = 1. \tag{2.24}$$

Then

$$\varepsilon_{eff} = f_a \varepsilon_a + f_b \varepsilon_b , \tag{2.25}$$

which is the optical equivalent of capacitors in parallel if ε_b is the dielectric function of a material. Also, the optical equivalent of capacitors in series is

$$\frac{1}{\varepsilon_{eff}} = \frac{f_a}{\varepsilon_a} + \frac{f_b}{\varepsilon_b} . \tag{2.26}$$

The Maxwell-Garnett approach [2.11] assumes that each region is spherical, surrounded by the host material and well separated from the neighbouring regions. This is expressed as

$$\frac{\varepsilon-\varepsilon_b}{\varepsilon+2\varepsilon_b}=f_a\frac{\varepsilon_a-\varepsilon_b}{\varepsilon_a+2\varepsilon_b}\ , \tag{2.27}$$

where $f_a=(4\pi/3)r_a^{\,3}/V$

is the volume fraction occupied by the material *a* and *V* is the total volume of the system. This can be written in two-dimensional coordinates and screening effects can be taken into account. Bruggeman [2.12] resolved inherent difficulties in the Maxwell-Garnett expression by considering that inclusions should be treated as being surrounded in the effective medium itself. The general expression then becomes

$$0=f_a\frac{\varepsilon_a-\varepsilon_h}{\varepsilon_a+s\varepsilon_h}+f_b\frac{\varepsilon_b-\varepsilon_h}{\varepsilon_b+s\varepsilon_h} \tag{2.28}$$

which is known as the Bruggeman effective medium approximation, with a and p different types of particles and h denotes the host material. If the composite is isotropic in three-dimensions then we set $s = 2$ in general. While the Maxwell-Garnett approach describes an isotropic matrix containing spherical inclusions that are isolated from each other (cermet microstructure), the Bruggemann theory allows for like materials to contact like materials and therefore accounts for correlations due to the self consistent determination of the dielectric properties (aggregate microstructure).

The optical band gap

To obtain the optical band gap it is necessary to first review the role that the density of states and the conductivity of the amorphous layer play in the optical processes that are active in the bulk of the material. The photoconductivity of the amorphous thin film is defined by [2.13]:

$$\sigma(\omega) = \frac{2\pi e^2 \hbar^3 \Omega}{m^2 \hbar \omega} \int \{f(E) - f(E + \hbar\omega)\} N(E) \left|P(\omega)\right|^2 N(E + \hbar\omega) dE \qquad (2.29)$$

When interband transitions occur, N(E) and N(E + $\hbar\omega$) refer to the density of states in the valence bands and conduction bands respectively. Ω is the size of the volume element containing one electron while f(E) is the Fermi-Dirac distribution. P(ω) is the constant momentum matrix element for absorption. The strength of optical absorption is given by the logarithmic fraction of photons absorbed per cm^2 of the material. This makes the absorption coefficient α proportional to the product of the density of those occupied states and the density of those unoccupied states that can be bridged by the energy $h\nu$ or $\hbar\omega$ of the incident photon, if the transition probability is the same for all states. A good approximation for the interband transitions is the Fermi-Dirac distribution where the temperature T = 0 K. Equation 2.29 then simplifies to

$$\sigma(\omega) = \frac{2\pi e^2 \hbar^3 \Omega}{m^2 \hbar \omega} \int N(E) \left|P(\omega)\right|^2 N(E + \hbar\omega) dE \,. \qquad (2.30)$$

Equation 2.30 can be rewritten as

$$\alpha(\omega) = \frac{2\pi e^2 \hbar^3 \Omega}{m^2 \hbar \omega \varepsilon_0 n(\omega) c} \int N(E) \left|P(\omega)\right|^2 N(E + \hbar\omega) dE \,, \qquad (2.31)$$

since the absorption coefficient is related to the photoconductivity by

$$\alpha(\omega) = \frac{\sigma(\omega)}{\varepsilon_0 n(\omega) c}. \tag{2.32}$$

The density of states is shown in figure 2.3:

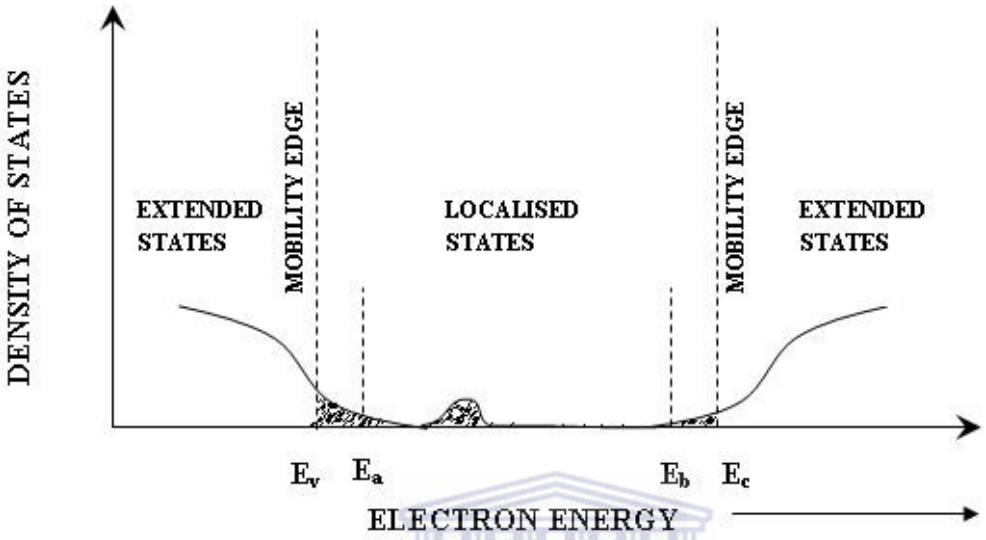

Figure 2.3 Density of states diagram of an amorphous material [2.14].

E_a and E_b are localised states amongst the states in the mobility edges of the valence and conduction bands respectively. The density of states are:

$$N = N_v \left(\frac{E_a - E}{E_a - E_v} \right)^p \quad \text{for } E \le E_a$$

$$N = N_c \left(\frac{E - E_b}{E_c - E_b} \right)^q \quad \text{for } E \ge E_b, \tag{2.33}$$

while p and q describe the density of states distribution in the valence and conduction bands respectively. Substituting equations 2.32 and 2.33 into equation 2.31 and integrating over all possible transitions; yields the solution for the absorption coefficient:

$$\alpha(\omega) = \frac{2\pi e^2 \hbar^3 \Omega}{m^2 \hbar\omega \varepsilon_0 n(\omega) c} \frac{\Gamma(p+1)\Gamma(q+1)}{\Gamma(p+q+2)} \times \frac{N_v N_c}{(E_a - E_v)^p (E_c - E_b)^q} \left\langle \left| P(\omega) \right|^2 \right\rangle (\hbar\omega - E_g)^{1+p+q} \tag{2.34}$$

The momentum transition matrix element P(ω) for absorption is also averaged over the range of energies. For reasons of simplicity, P(ω), is assumed to be independent of ω. It follows that

$$\left[\alpha(\omega) n(\omega) \hbar\omega\right]^{1/(1+p+q)} = B_g (\hbar\omega - E_g), \tag{2.35}$$

where B_g is a constant and E_g is the optical band gap.

If the density of states distribution is taken to be parabolic in both the valence and conduction bands (p = q = ½); then the equation describes the Tauc gap [2.15]. The Tauc band gap is determined by extrapolating $[\alpha(\omega)n(\omega)\hbar\omega]^{1/2}$ versus $\hbar\omega$ to $\alpha(\omega) = 0$; for $\alpha(\omega) \geq 10^3$ cm^{-1}. If the density of states distribution is taken to be linear (p = q = 1) instead of parabolic, then the equation describes the Cubic or Bezemer gap [2.16] , where the straight line section on the axis of the graph $[\alpha(\omega)n(\omega)\hbar\omega]^{1/3}$ versus $\hbar\omega$ is extrapolated to $\alpha(\omega) = 0$. The cubic plot is linear over a larger energy range than the Tauc plot and is normally 0.1 to 0.2 eV smaller than the Tauc gap.

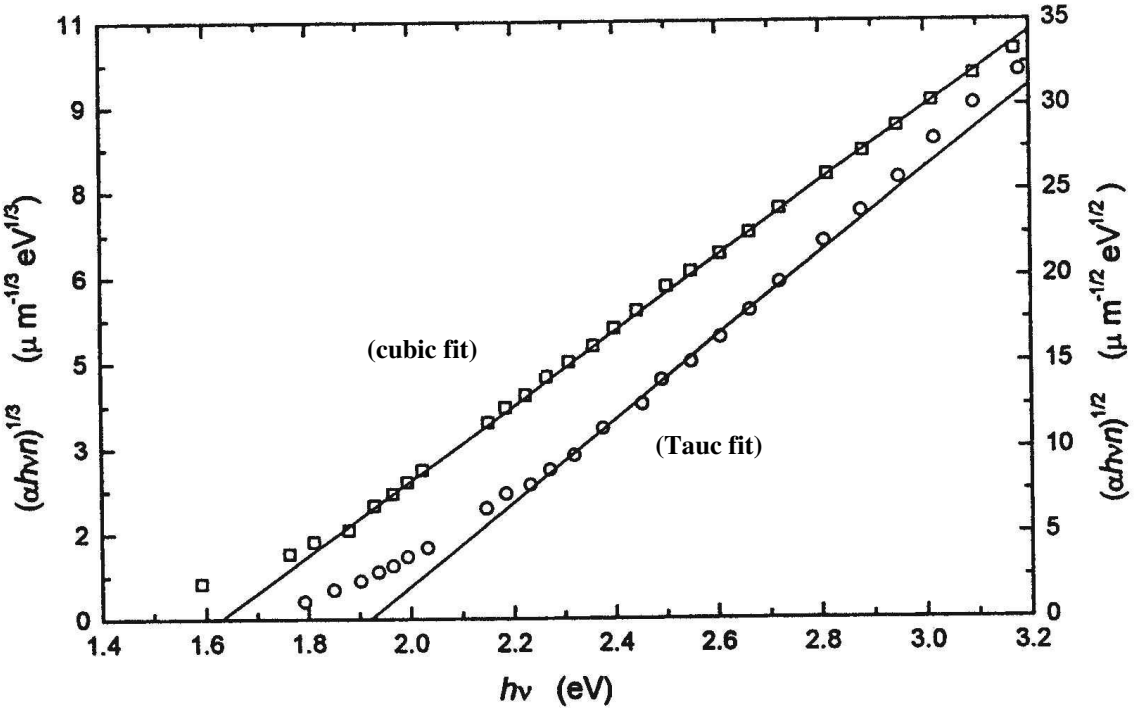

Figure 2.4 Straight line fit to obtain the optical band gap [2.7].

Experimentally the Tauc optical bandgap can be obtained by fitting a straight-line on the section of the curve of $(\alpha h\nu n)^{\frac{1}{2}}$ vs $h\nu$ that appears linear. The cut-off on the x-axis serves as the optical band gap.

The O'Leary, Johnson, Lim (OJL) fitting model of the optical band gap

The OJL method [2.17] employs an elementary empirical model for the distribution of electronic states and determines the corresponding optical absorption spectrum of an amorphous semiconductor, which provides us with a means of interpreting the physical significance of optical absorption data.

In their notation the conduction-band density of states (DOS) function is given by

$$N_c(E) = \frac{\sqrt{2} m_c^{*3/2}}{\pi^2 h^3} \begin{cases} \sqrt{E - V_c}, E \geq V_c + \dfrac{\gamma_c}{2} \\ \sqrt{\dfrac{\gamma_c}{2}} \exp\left(-\dfrac{1}{2}\right) \exp\left(\dfrac{E - V_c}{\gamma_c}\right), \\ E < V_c + \dfrac{\gamma_c}{2} \end{cases} \tag{2.36}$$

where m_c* represents a DOS effective mass which is associated with the conduction band, V_c denotes the conduction band disorderless band edge, γ_c reflects the breadth of the conduction band tail, and $V_c + \gamma_c/2$ denotes the transition point between square-root and linear-exponential distributions of states, $N_c(E)$ and its first derivative being continuous at this point. Similarly, we assume that the valence-band DOS function

$$N_v(E) = \frac{\sqrt{2} m_v^{*3/2}}{\pi^2 h^3} \begin{cases} \sqrt{\dfrac{\gamma_v}{2}} \exp\left(-\dfrac{1}{2}\right) \exp\left(\dfrac{V_v - E}{\gamma_v}\right) \\ E \geq V_v - \dfrac{\gamma_v}{2}, \\ \sqrt{V_v - E}, E < V_V - \dfrac{\gamma_v}{2} \end{cases} \tag{2.37}$$

where m_v * represents a DOS effective mass, which we associate with the valence band, V_v denotes the valence band disorderless band edge, γ_v reflects the breadth of the valence band tail, and $V_V - \frac{\gamma_v}{2}$ denotes the transition point between square-root and linear-exponential distributions of states, $N_v(E)$ and its first derivative being continuous at this point.

As the band tailing, which occurs in amorphous semiconductors, is fundamentally related to the disorder that characterizes these materials, the tail breadth parameters, γ_c and γ_v provide a measure of this disorder. To study the effect of disorder, the sensitivity of $N_c(E)$ to variations in γ_c was tested. In the disorderless limit, where $\gamma_c \rightarrow 0$, the conduction-band

DOS function terminates abruptly at the disorderless band edge V_c, while for finite γ_c, a distribution of tail states appeared below the mobility edge. As γ_c increased from this disorderless limit, the total number of localized tail states increased, and the distribution of tail states further encroached into the gap. Similar results for the valence band DOS $N_v(E)$ was observed. This elementary empirical model for the distribution of electronic states was found to be consistent with experiment.

It was also demonstrated that the Tauc gap was not simply equal to the difference between V_c and V_v, as might have been expected from the analysis of Tauc *et al.*, but that rather the disorder parameters, γ_v and γ_c were are also seen to play a role in determining the magnitude of the Tauc band gap. The study also provides a quantitative means of reducing the uncertainty experienced experimentally in the determination of the Tauc band gap due to questions as to where linearization of data should be performed. Thus the elementary empirical model for the distribution of electronic states was used to determine the form of the optical absorption spectrum, how the Tauc gap and the absorption tail breadth are related to the parameters that characterize the underlying distribution of electronic states.

2.2.2.3 EXPERIMENTAL SET-UP

The UV-Vis characterization reflection and transmission spectra were simultaneously recorded at the same spot. The spectra were taken with the thin layer facing the light source. The spectrophotometer consisted of a halogen lamp, two diode-array spectrometers, optical fibres and a sample stage, supplied by M. Theiss hard- and software [2.18]. The diode arrays have 512 pixels over a wavelength range from 380 to 1050 nm. The analysis of the spectra were performed with the Scout® software, which makes use of the O' Leary, Johnson, Lim (OJL) fitting procedure described above to model amorphous semiconducting materials.

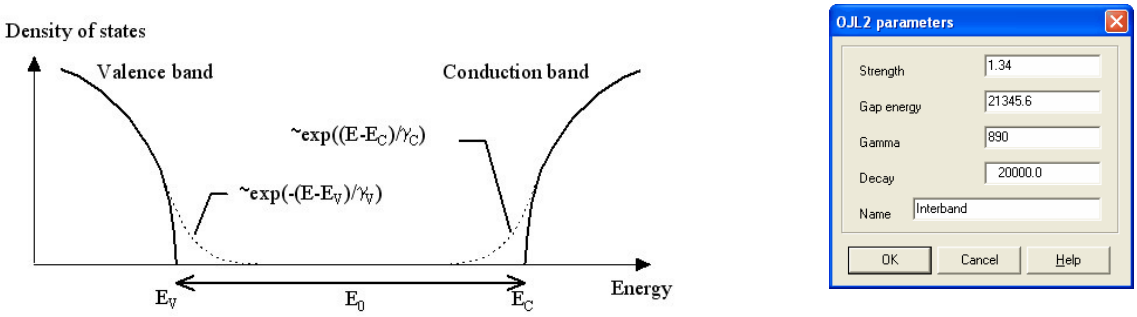

Figure 2.5 OJL parameters used in the fitting of amorphous semiconducting RT spectra [2.18].

Scout® makes use of the fact that in most cases it is the electric field of the probing light wave that interacts with the sample. Hence excitations can be observed in optical experiments that are going along with a polarization. The polarization P induced by an externally applied electric field E in a homogeneous material is given by the electric susceptibility χ:

$$P = \varepsilon_0 \chi E \,. \tag{2.38}$$

The dielectric function ε which connects the dielectric displacement and the electric field vector is closely related to the susceptibility by:

$$\begin{aligned} D &= \varepsilon_0 \varepsilon E, \\ \varepsilon &= 1 + \chi \end{aligned} \,. \tag{2.39}$$

The frequency dependence of the susceptibility is very characteristic for a material since it incorporates vibrations of the electronic system and the atomic cores as well as contributions from free charge carriers. The complex refractive index $n + ik$ is the square root (with positive imaginary part) of the dielectric function. Thus in order to use a

material in SCOUT® its optical constants have to be defined. The OJL model described above are implemented in the software to describe amorphous semiconductors. Expressions for the joint density of states are given for the optical transitions from the valence band to the conduction band. Parabolic bands are assumed with tail states decaying exponentially into the band gap, as shown in figure 2.5. The imaginary part of the dielectric function is proportional to the combined density of states obtained from the above assumption on the density of states of the valence and conduction band. Without modification, the original expression for the imaginary part of the dielectric function would increase to infinity with increasing energy. Due to this unrealistic behaviour the construction of the real part of the dielectric function by two Fourier transforms is not possible. Therefore, a so-called decay parameter has been added to the original expressions to drag down the imaginary part to zero. The fit parameters of the OJL interband transition model are the energy gap E_0, the tail state exponent of the valence band γ and the overall strength of the transition. In addition, Scout® allows for the creation of mixed phase composites. The effective medium approximation (EMA) of Bruggeman is also a built-in feature of the software. Figure 2.6 is a flowchart of an example of a porous microcrystalline silicon layer built in Scout® using an Effective Medium Approximation, while Appendix A shows the various screens encountered during the construction of such a model.

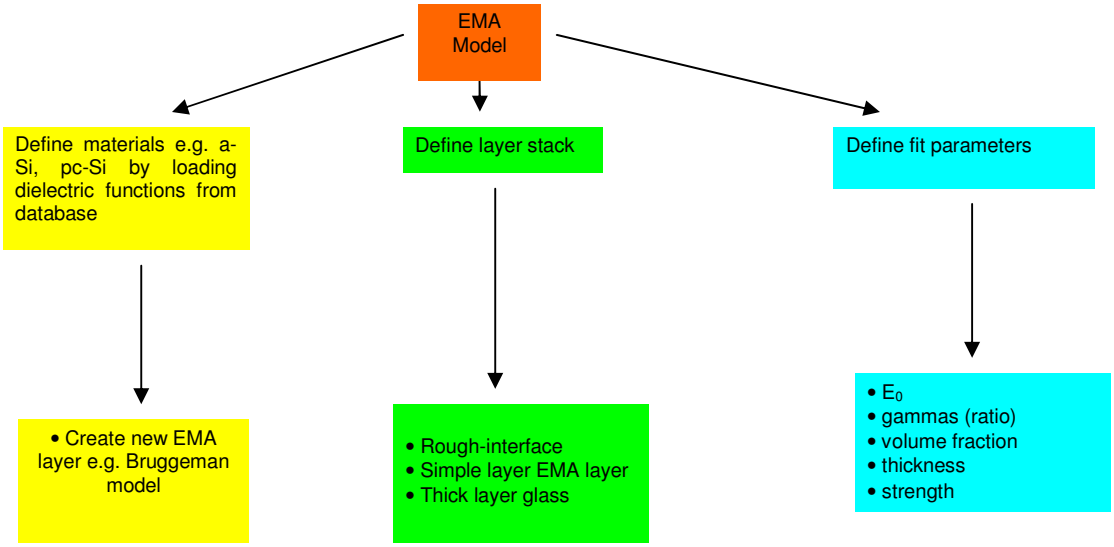

Figure 2.6 Creating an EMA optical model in Scout®.

2.2.2 FOURIER TRANSFORM INFRARED SPECTROSCOPY

2.2.2.1 INTRODUCTION

Fourier-Transform Infrared (FTIR) is the preferred method of infrared spectroscopy. It is a non-destructive technique that is easy to perform and provides a precise measurement of the vibrational motion of polyatomic molecules.

In polyatomic molecules, the frequencies of molecular vibrations can be used to identify the various types of bonds and functional groups present in the molecule. The frequencies of these molecular vibrations usually lie in the infrared region of the electromagnetic spectrum. For infrared spectroscopy, the electric dipole moment of the molecule must change during vibration in order for a particular vibration mode to be infrared active. Therefore H_2 molecules in a-Si:H cannot be detected with FTIR spectroscopy [2.19]. Infrared absorption spectroscopy rather gives qualitative information about bond structures containing hydrogen in the amorphous silicon host matrix, and quantitative

information about the relative amount of bonded hydrogen in the different bonding structures. These features of FTIR analysis are important, since besides the hydrogen content, the exact bonding configuration of silicon and hydrogen atoms can also affect the quality of hydrogenated silicon films [2.19].

Since the measured interferogram signal cannot be measured directly, a means of decoding the individual frequencies is accomplished by using the Fourier Transformation mathematical technique via computer code, which presents the user with the desired spectral information for analysis.

2.2.2.2 THEORY

The relationship between the transmission spectrum and the absorption coefficient $\alpha(\omega)$, is given by:

$$\alpha(\omega) = -\frac{\ln[T(\omega)]}{d}, \tag{2.40}$$

where d is the thickness of the a-Si:H layer.

Infrared transmission I(ω) as a function of vibrational frequency ω was measured by first collecting a background spectrum of the c-Si substrate to eliminate absorption by the c-Si substrate. Unlike glasses, semiconductors like silicon have good infrared transparency and are not sensitive to humidity. Hence the substrate chosen for the characterization of thin films are mono-crystalline silicon wafers of orientation <100>. The sample (thin film layer on c-Si substrate) was subsequently measured and the spectrum of the thin film produced.

A procedure known as the Brodsky-Cardona-Cuomo (BCC) correction [2.20] was introduced by Brodsky *et al.* to account for the effect of incoherent reflections, since multiple reflections occur in both the substrate (incoherent reflections) and the thin film. The Si:H film and the substrate are assumed to have the same refractive index; and the

overestimated value of the absorption coefficient can be corrected by relating α_{BCC} to the measured transmission T(ω) by [2.20]:

$$T(\omega) = \frac{4T_0 e^{-\alpha_{BCC} d}}{[(1+T_0)^2 - (1-T_0)^2 e^{-2\alpha_{BCC} d}]}, \tag{2.41}$$

where

d is the film thickness,

T_0 the baseline transmission when $\alpha(\omega) = 0$ and

$T_0 = 0.54$ for crystalline silicon.

The effect of the coherent reflections in the Si:H film was eliminated by Maley *et.al.* [2.21 – 2.22] by devising a solution to add to the BCC correction, given by:

$$\alpha_{TRUE} = \frac{\alpha_{BCC}}{1.72 - 12\omega d}; \text{ for } \omega d \leq 0.06$$

or

$$\alpha_{TRUE} = \alpha_{BCC} \quad ; \text{for } \omega d > 0.06 \tag{2.42}$$

Vibrational Modes

The phonon vibrational modes for a-Si:H occur in three energy bands [2.23]:

(i) a broad peak at 630 cm^{-1} which is always present;

(ii) a group of sharp lines at 800 cm^{-1} – 900 cm^{-1} whose shape and intensity depend on deposition conditions; and

(iii) modes in the range 2000 cm^{-1} – 2200 cm^{-1} with a similar dependence on deposition.

The generally accepted assignments of the Si-H_x vibrational modes to absorption bands are given in table 2.1:

ENERGY (cm^{-1})	**BONDING CONFIGURATION**	**VIBRATIONAL MODE**
630	Si-H, $Si-H_2$, $(Si-H_2)_n$, $Si-H_3$	Rocking
845	$(Si-H_2)_n$	Bending
880	$Si-H_2$	Bending
890	$(Si-H_2)_n$	Bending
2000	Si-H (isolated)	Stretching
2070 – 2100	Si-H (on voids), $Si-H_2$, $(Si-H_2)_n$	Stretching
2130	$Si-H_3$	Stretching

Table 2.1 Generally accepted assignments of the $Si-H_x$ vibrational modes to absorption bands [2.23].

The following points are important considerations when analyzing an FTIR spectrum:

(i) the integrated absorption of the Si-H wagging mode at 630 cm^{-1} provides a good measure of the total bonded hydrogen content within the amorphous silicon film

(ii) all the Si-H bonds will contribute to the 630 cm^{-1} band

(iii) it is generally agreed that the stretching band at 2000 cm^{-1} correlates with dispersed Si-H groups and the stretching band at 2090 cm^{-1} correlates with SiH_2 and clustered $(SiH_2)_n$ groups

(iii) an empirical correlation exists between the 2090 cm^{-1} band and film inhomogeneities such as microvoids that may be dispersed throughout the material or that are associated with a columnar microstructure.

Thus it can be said that superior electronic properties are found in material in which the

2000 cm^{-1}absorption significantly exceeds the 2090 cm^{-1} absorption. A large quantity of SiH_2-groups usually indicates poor material. A typical FTIR spectrum of an a-Si:H film is shown in figure 2.7:

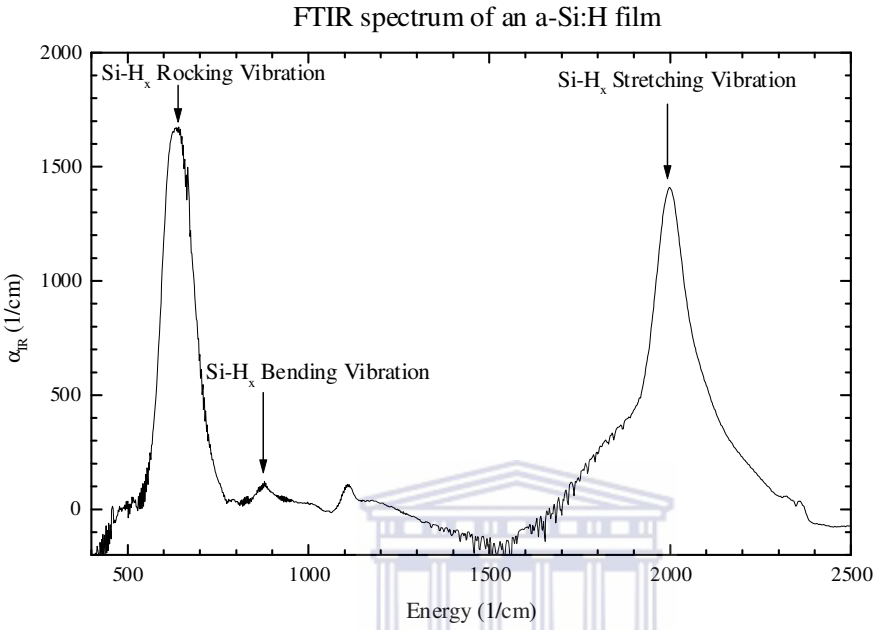

Figure 2.7 An example of an FTIR spectrum of an a-Si:H film.

The appearance of the spectra are convoluted due to the overlapping of several modes. FTIR spectra need to be deconvoluted into Gaussian shapes for all absorption bands as shown in figure 2.8:

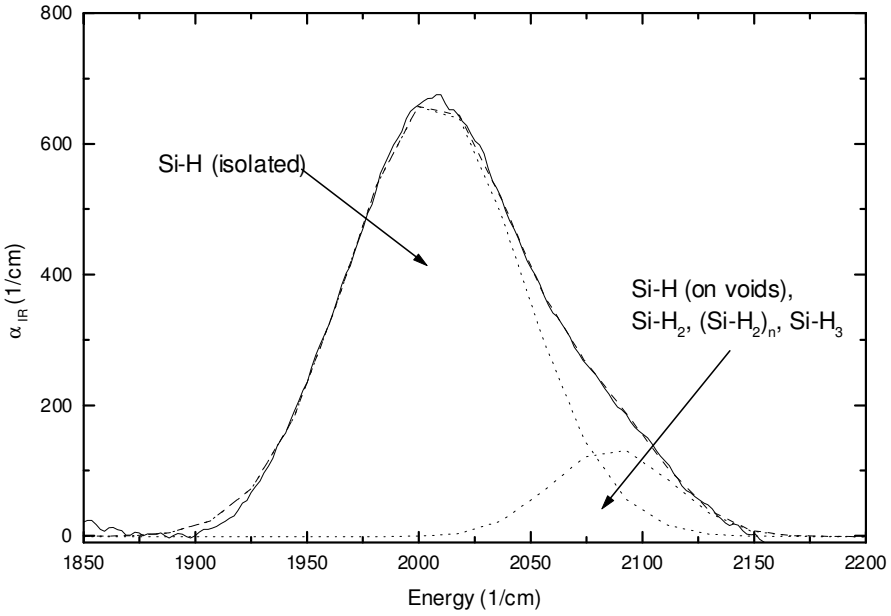

Figure 2.8 Extracted simulation of the 2000 cm^{-1} and 2100 cm^{-1} stretching modes.

Hydrogen concentration

The integrated absorption of each mode ω, I_ω, is given by:

$$I_\omega = \int_{-\infty}^{+\infty} \frac{\alpha(\omega)}{\omega} d\omega . \tag{2.43}$$

The hydrogen concentration in the sample can then be calculated from the bonded state of the 2000 cm^{-1} and 2100 cm^{-1} stretching modes, since they also provide information about the microstructure of a-Si:H [2.21]:

$$[H]_{stretching} = \frac{N_H}{(N_{Si} + N_H)} \times 100\% ,$$

$$N_H = A_\omega . I_\omega , \tag{2.44}$$

where N_{Si} is the average density of a-Si:H = 5.3 x 10^{22} cm^{-3},

I_ω is the integrated absorption strength of the specific mode, and

A_ω is a proportionality constant for the stretching mode.

The calculation of the concentration of bonded hydrogen from the stretching modes can be done according to the method described by Daey Ouwens [2.24]. This method yields the concentration of bonded hydrogen from these FTIR stretching modes as:

$$[H]_{stretching} = \frac{[(I_{2000} + I_{2100}) \times 0.176 - 2.732]}{0.53} \text{ at.\%}; \quad \text{for [H]>3 at.\%}$$

$$[H]_{stretching} = \frac{[(I_{2000} + I_{2100}) \times 0.065]}{0.53} \text{ at.\%} \quad ; \text{for [H]} \leq 3 \text{ at.\%} \qquad (2.45)$$

Since the 2000 cm^{-1}mode manifests isolated monohydride bonding and the 2100 cm^{-1} mode hydrogen bonded in Si-H_2, $(Si\text{-}H_2)_n$ multihydrides and Si-H inside voids, it is possible to define a microstructure parameter R^*, a measure for the material quality, given by:

$$R^* = \frac{I_{2100}}{(I_{2000} + I_{2100})}. \qquad (2.46)$$

Hydrogenated amorphous silicon films with good opto-electronic properties will have a low R^* value, which means that the presence of structural inhomogeneities in the sample is heavily outweighed by the hydrogen bonded in the isolated phase. Values of $R^* < 0.1$ indicate device-quality films.

In this thesis the preference will be to use the integrated area of the 640 cm^{-1} mode as a measure of the bonded hydrogen content in the film due to the fact that different

proportionality constants are used by researchers to determine the bonded hydrogen concentration in the a-Si:H films.

2.2.2.3 EXPERIMENTAL

Infrared transmission of a thin film sample deposited on a silicon wafer was measured by using Fourier Transform Infrared Spectroscopy. The FTIR spectra were collected with a DIGILAB FTS-40 FTIR spectrometer with a liquid-nitogen-cooled HgCdTe detector (Debye Institute, Utrecht University). The ambient temperature in the FTIR set-up amounted to 21°C.

Since the spectrophotometer is a single-beam instrument, it is necessary to measure a background spectrum prior to collecting a spectrum of a sample. A spectrum of a silicon <100> wafer similar to the one used for depositing the thin film was measured with an open beam; subsequently a sample with a deposited thin film layer was placed in the path of the beam. A spectrum was then produced with background subtracted from the spectrum of the sample. The resultant plot is then the spectrum of the thin film layer.

For a series of successive measurements on one day, only one background measurement was taken. All the spectra were measured in the range of wavenumbers 400 – 4000 cm^{-1}, with a resolution of 4 cm^{-1}.

2.2.4 X-RAY DIFFRACTION

2.2.4.1 INTRODUCTION

X-rays are photons with wavelengths of the order of a fraction of a nanometre compared with the hundreds of nanometres of light waves; thus their wavelengths are comparable to the interatomic distances in crystals. Diffraction pattern analysis plays an important role in diverse applications such as solving molecular structures, identifying compounds, and the fabrication of materials [2.25], making it an excellent tool to obtain information

regarding the crystalline nature of thin layers of hydrogenated silicon on a substrate [2.26 – 2.29].

2.2.4.2 THEORY

X-ray diffraction (XRD) was used to verify crystallinity of thin Si films, and the orientation of the crystallites present in MIC films. The technique makes use of the diffraction of a monochromatic X-ray beam and during the measurement the intensity of the diffracted radiation is measured as a function of 2θ, which is the angle between the sample surface being irradiated, and the incident X-ray beam. This is referred to as the θ-2θ configuration. Intensity peaks are the found at specific angles according to the Bragg Law [2.25]:

$$2d \sin\theta = n\lambda, \tag{2.47}$$

where

λ is the wavelength of the incident radiation,
d is the interplanar spacing, and
n is an integer constant.

The angle θ is also known as the Bragg angle. Since the angle of reflection off a plane surface is equal to the angle of incidence, the Bragg angle also defines the scattering angle, which is the angle between the incident radiation and the scattered radiation and is equal to 2θ.

The interplanar spacing d, of a set of parallel crystallographic lattice planes, is defined by the dimensions of the crystal unit cell. There exists an infinite number of such families of parallel planes in any given crystalline lattice, and each is associated with a particular Bragg angle θ. Each set of planes is characterized by the three indices hkl, and the resultant diffracted beam is termed the hkl-reflection. For a cubic crystalline structure the

interplanar distance d can be calculated from the three lattice vectors specifying a three-dimensional crystal unit cell by [2.25]:

$$d_{hkl} = \frac{a}{\sqrt{h^2 + k^2 + l^2}}, \tag{2.48}$$

where

a is the lattice parameter of the unit cell and

h, k, and l are the conventional Miller indices.

The inverse relationship between θ and d has given rise to the notion of a reciprocal lattice, which completely describes the crystal in that each reciprocal lattice point is related to a set of planes in the crystal and represents the orientation and spacing of that set of planes. The peak position is given by the lattice distance and lattice parameters, and the intensity is then a quantitative statement. Diffraction thus makes it possible to distinguish between the different phases of material. The size of the measured crystallites determines the width of the XRD peaks, and the average diameter of the crystallites with a certain orientation can be estimated by using Scherrer's formula [2.25]:

$$t = \frac{0.9\lambda_{X-ray}}{B\cos\theta_B}, \tag{2.49}$$

where B is the full width at half maximum of the measured peak in radians, and θ_B the peak angle.

2.5.4.3 EXPERIMENTAL SET-UP

X-Ray diffraction spectra were obtained at the CSIR, Pretoria, South Africa by means of a Panalytical X-ray powder diffractometer operating at 45 kV and 40 mA, collected in reflection geometry at 2θ-values ranging from 5 to 70° with a step size of 0.026°. A Copper $K_{\alpha 1}$ radiation with a wavelength of 1.5406 Å was used as the X-ray source.

The (hkl) values as a function of 2θ were calculated by accompanying computer software. The corresponding geometry of the cell that allows reflection at an angle is found by comparing the experimentally observed angle at which a peak is detected with spectra from a database.

2.2.5 RAMAN SCATTERING

In Raman Spectroscopy laser light is incident on the material that result in the inelastic Raman scattering of the light on phonons in the material. The shift in the wavelength of the scattered light is equal to the energy of the phonon that has been created [2.30]:

$$h\upsilon_s = h\upsilon_0 \pm \Delta E\,, \tag{2.50}$$

where $h\nu_s$ is the energy of the scattered light, $h\nu_0$ the energy of the incident light and ΔE the energy shift that corresponds to the energy of a phonon that has been created (Stokes scattering) of annihilated (anti-Stokes scattering). In our measurements the Stokes scattering in the range between 0 and 1200 cm^{-1} of a 514.5 nm line of a Spectra Physics Ar^+-ion laser, using a Spex triple-grating monochromator and a Roper Scientific CCD camera, was recorded. The phonon density of states is reflected in Raman shift spectrum.

2.2.6 PHOTOTHERMAL DEFLECTION SPECTROSOPY

One of the sensitive methods to measure the sub-bandgap absorption is the photothermal deflection spectroscopy (PDS) technique [2.31]. It allows for determination of the density of the mid-gap states in amorphous silicon, as well as the indirect band gap of micro and polycrystalline Si films. The sample is illuminated by a chopped, monochromatic pump beam while immersed in an optically transparent and thermally conductive liquid, namely Fluorinert FC-40. Absorption by the sample may occur at certain wavelengths and the liquid can absorb the energy when the heat is dissipated from the sample into the liquid. Thus, a laser beam parallel to the sample surface will deflect such that the deflection signal can be measured by a position sensitive detector connected to a lock-in amplifier.

The angle of deflection of the probe beam is expressed with relation to the absorption coefficient α as [2.32]:

$$\Delta\Phi \propto\sim L\frac{dn}{dT}I_0\alpha d\,, \tag{2.51}$$

where L is the width of the pump spot parallel to the direction of the laser beam, $\frac{dn}{dT}$ is the derivative of the refractive index of the liquid with respect to the temperature, I_0 is the pump beam intensity, and d the thickness of the sample. By measuring both the deflection of the laser beam and the intensity of the pump beam at different wavelengths a relative absorption spectrum of thin film can be obtained. For short wavelengths all light is absorbed in the film and the absorption spectrum becomes flat; thus the data can be scaled to absorption coefficients obtained from RT measurements in the region in the region mentioned above where such that an absolute spectrum is obtained. A complete description of the experimental set up and analysis of a-Si:H films is given in [2.32].

2.2.7 ELECTRICAL CONDUCTIVITY

Electrical characterization of thin silicon films deposited on Corning glass consisted of measuring the dark and photoconductivity of the specific film. Two coplanar Ag electrodes, each with a length *l* in mm were evaporated onto the film of thickness *d* such that the parallel contacts had a separation distance *w* in mm. When applying a voltage *V* between the electrodes the current *I* can be measured. The conductivity is then calculated from

$$\sigma = \frac{Iw}{Vld}\,, \tag{2.52}$$

where I is the measured current, V is the applied voltage and d the film thickness.

The dark conductivity was measured in complete darkness while the photoconductivity was measured using an Oriel solar simulator with a Xe lamp source operating under standard AM1.5 conditions, in other words 100 mW/cm^2 power flux.

REFERENCES

2.1 R. E. I. Schropp, K. F. Feenstra, E. C. Molenbroek, H. Meiling, J. K. Rath, Phil. Mag. B 76, (1997) 309

2.2 M. van Veen, PhD Thesis, Utrecht University, Utrecht, The Netherlands (2003)

2.3 J. M. Ziman, in 'Principles of the Theory of Solids', Cambridge University Press (1964)

2.4 S. G. Tomlin, J. Phys. D 2, (1968) 1667

2.5 S. G. Tomlin, J. Phys. D 5, (1972) 847

2.6 R. Swanepoel, J. Phys. E: Sci. Instrum. 16, (1983) 1214

2.7. R. Swanepoel, in 'Properties of amorphous silicon and its alloys' editor Tim Searle, Emis data-review series, University of Sheffield, U. K. (1998)

2.8 R. Swanepoel, J. Phys. E: Instrum. 17, (1984) 896

2.9 D. E. Aspnes, in 'Handbook of Optical Constants of solids', edited by Edward D. Palik, Academic Press, San Diego (1998)

2.10 In Kyo Kim, PhD Thesis, North Carolina State University, Raleigh, USA (2006)

2.11 J.C.Maxwell Garnett, Philos. Trans. R. Soc. London 203, (1904) 385

2.12 D.A.G. Bruggeman, Ann. Phys. 24, (1935) 636

2.13 N. F. Mott and E. A. Davis, in 'Electronic Processes in Non-Crystalline Materials', Clarendon Press, Oxford, U.K. (1971)

2.14 R. Zallen, in 'The Physics of Amorphous Solids', John Wiley & Sons (1983)

2.15 J. Tauc, in 'Optical Properties of Solids', editor. F. Abeles, North-Holland Publ., Amsterdam (1972)

2.16 R. H. Klazes, M. H. L. M. van den Broek, J. Bezemer and S. Radelaar, Phil. Mag. B 45, (1982) 377

2.17 S.K.O'Leary, S.R.Johnson, P.K.Lim, J.Appl. Phys. Vol. 82(7), (1997) 3334

2.18 www.mtheiss.com

2.19 W. S. Lau, in 'Infrared Characterization for Microelectronics', World Scientific, Singapore (1999)

2.20 M. H. Brodsky, M. Cardona and J. J. Cuomo, Phys. Rev. B 16, (1977) 3556

2.21 A. A. Langford, M. L. Fleet, B. P. Nelson, W. A. Lanford and N. Maley,

Phys. Rev. B 45 (23), (1992) 13367

2.22 N. Maley, Phys. Rev. B 46 (4) , (1992) 2078

2.23 R. A. Street, in 'Hydrogenated Amorphous Silicon', Cambridge Solid State Science Series, New York (1991)

2.24 J. Daey Ouwens and R.E. Schropp, Mater. Res. Soc. Symp. Proc. 297, (1995) 27

2.25 B. D. Cullity, in 'Elements of X-ray diffraction', Addison-Wesley Publishing Company, Reading, Massachusetts (1978)

2.26 P. Brogueira, J. P. Conde, S. Arekat and V. Chu, J. Appl. Phys. 79 (11), (1996) 8748

2.27 D. L. Williamson, Mater. Res. Soc. Symp. Proc. 557, (1999) 251

2.28 A. H. Mahan, J. Yang, S. Guha and D. L. Williamson, Mater. Res. Soc. Symp. Proc. 557, (1999) 269

2.29 Guha, J. Yang, D. L. Williamson, J. D. Cohen, and A. H. Mahan, Appl. Phys. Lett. 74 (13), (1999) 1860

2.30 Charles Kittel, in 'Introduction to Solid State Physics', seventh edition, John Wiley and sons, New York (1996)

2.31 W. B. Jackson, N. M. Amer, A. C. Boccara, D. Fournier, Appl. Opt. 20, (1981) 1333

2.32 E. H. C. Ullersma, PhD Thesis, Utrecht University, Utrecht, The Netherlands (1998)

CHAPTER 3

Optical Modeling of the dielectric function of μc-Si:H

3.1 INTRODUCTION

For decades hydrogenated amorphous silicon has been the mainstay of the silicon photovoltaic industry, but has been superseded by a new phase material. A decade ago, the new-phased, hydrogenated microcrystalline silicon (μ-Si:H) was beginning to be exploited for incorporation into photovoltaic devices and its properties were investigated in more detail; much progress was made such that nowadays it has become standard for microcrystalline layers to be incorporated into solar cells [3.1 – 3.2]. During the chemical vapour deposition process, the silane concentration determined by the flow ratio of silane in hydrogen gas is varied to control the microstructure of the hydrogenated microcrystalline silicon, affecting the optoelectronic properties of the material [3.3]. Thus it is still of importance to optimize deposition regimes within the two major deposition techniques, namely plasma enhanced chemical vapour deposition (PECVD) and the relatively newer hot wire chemical vapour deposition (HWCVD) where fast deposition times can combine with device quality silicon material [3.4]. The optical properties of the silicon layers then need to conform to the standard of quality of material normally manufactured in the more established, slower deposition regimes.

UV-VIS spectroscopy provides a fast and non-destructive method to characterize amorphous and nano or microcrystalline silicon materials optically. The methods for the analysis of the optical properties and the extraction of the thickness of hydrogenated

amorphous silicon (a-Si:H) thin films from transmission and/or reflection spectra obtained by UV-VIS spectroscopy have been refined to a satisfactorily level during the past decades. They generally differ by calculation method [3.5 – 3.7]. A well-known method is that of Swanepoel [3.5], which makes use of minima and maxima envelopes drawn around the transmission curve. This elegant method works rather well for thin amorphous silicon films with thickness between 200 and 1000 nm, but breaks down for very thin films due to the absence of interference fringes in the transmission spectrum, which are necessary for the calculation of the thickness of the film. The method has also been applied to thin films of nano/microcrystalline silicon films [3.8], but nc-Si:H and μc-Si:H thin films consist of crystalline and amorphous phases of silicon together with voids. As such, the effect of crystallites embedded in the bulk of the material is not taken into account in the method, such as in the case of spectroscopic ellipsometry [3.9].

Earlier, the Utrecht group performed a study on microcrystalline silicon to determine the thickness of μc-Si:H layers fast and accurately down to a thickness of 20 nm [3.10], using commercially available software called Scout® [3.11] to model the reflection (R) and transmission (T) spectra with an amorphous semiconductor dielectric function. The thickness and optical properties extracted from Scout® were confirmed and correlated with other measurement techniques. The single phased, one layer optical modeling on the spectroscopic measurements yielded very valuable information. Yet, additional steps are to be considered to ensure that the optical model is an accurate physical representation of the thin films under study. This implies that the model must be sufficiently representative of the intrinsic optical functions over the measured spectral range. This work therefore extends the built-in capabilities of the Scout® software such that material description in the software program correlates more clearly with the actual physical material under investigation. The software models the dielectric function of the microcrystalline thin film by including crystallites and voids in the semiconductor matrix. The inclusive model described in this chapter is also a building block in the analysis of R and T spectra of crystallized silicon by the metal induced solid phase crystallization method, which will be described in a follow-up chapter. For such material the dielectric function of a single

layer amorphous semiconductor turned out to be incapable in modeling the optical properties of such a multi-phased material satisfactorily.

3.2 EXPERIMENTAL DETAILS

A porous μc-Si:H sample of thickness < 500 nm deposited in the ASTER system (Process equipment for Amorphous Semiconductor Thin film Applications), at Utrecht University was first subjected to the inclusive modeling. The deposition conditions of the series of samples from which this sample was selected were described elsewhere [3.12]. The modeling method efficiency was to be confirmed on relatively thin and thicker layers of μc-Si:H, which were found to be extremely difficult to analyse earlier. A μ-Si:H series of samples was prepared by the HWCVD process in the PASTA chamber at Utrecht University [3.4]. The substrate temperature was typically around 250°C while the hydrogen dilution was varied to obtain silicon films of increasing crystallinity. The series formed a subset for a project where high growth rate material by HWCVD was manufactured [3.4]. The films were deposited on Corning 2000 glass and 300 μm thick c-Si wafers. The latter samples were used for FTIR measurements, while the glass samples were used for UV-VIS and Raman spectroscopy measurements. For the UV-VIS characterization, reflection and transmission spectra were simultaneously recorded at the same spot, with the thin layer facing the light source.

The hydrogen bonding configurations were probed by Fourier-Transform Infrared Spectroscopy (FTIR) in the vibration modes reflected in the IR absorption spectra. The measurements were performed with a Bio-Rad (Digilab) FTS-40 spectrometer. The absorption spectrum of the sample was corrected for the absorption of the substrate. Further corrections included those for multiple reflections in the substrate and coherent reflections within the layer, the BCC corrections [3.13 – 3.14]. Raman Spectroscopy was used to obtain information about the crystalline nature of the silicon thin films. The recorded Raman shift spectrum contains the transverse-optic (TO) mode of crystalline silicon at 510 - 520 cm^{-1} as well as the longitudinal acoustic (LA) mode at 330 cm^{-1}, longitudinal-optic (LO) mode at 445 cm^{-1} and transverse optical (TO) mode at 480 cm^{-1}

of amorphous silicon. The crystalline ratio R_c in the penetration region of the sample is defined by the contributions of the different phases to the crystalline TO mode as follows: $R_c = \frac{I_{510} + I_{520}}{I_{480} + I_{510} + I_{520}}$, where I_x denotes the integrated intensity of the contribution centred on x cm^{-1}.

The sub-bandgap absorption was measured with the photothermal deflection spectroscopy (PDS) technique, with which it is possible to measure the absorption in the thin films to values of αd down to 10^{-5} [3.15]. The experimental detail was described in detail by Ullersma [3.15]. To obtain absolute absorption spectra the data was scaled to the $\alpha(E)$ data from the reflection/transmission measurements, after the interference fringes in the PDS spectra were suppressed according to the method proposed by Neri *et al*. [3.16].

3.3 RESULTS AND DISCUSSION

3.3.1 THE OPTICAL MODEL-1.

The basic building block in the description of the μc-Si:H is the amorphous silicon matrix component. The Scout® software has a built-in master a-Si model based on the OJL interband transition model [3.17]. With this model, parameters are set up to describe an amorphous semiconductor thin film; these are shapes of conduction and valence band densities of states, the energy gap between the band edges and the width of the exponential band tails. From the initial fit parameters the program calculates the simulated R and T spectra together with the associated optical constants over the specified energy range. The simulated spectra are then compared to the measured ones. The program then changes the initial fit parameters and calculates new R and T spectra such that if the comparison with the measured spectra results in a smaller deviation, then the program replaces the initial fit parameters. This iterative process is repeated until no further improvement of the deviation can be achieved. If the absorption coefficient as a function of frequency (energy) for all frequencies is known, then both n and k can be evaluated as functions of frequency, separately since they satisfy the condition for

Kramers-Kronig relations. From dispersion relations the complex refractive index $n + ik$ is established as the square root (with positive imaginary part) of the dielectric function. Both the dielectric function and the refractive index are optical constants associated with the material under study. Internal calculations by the SCOUT® software use the dielectric function for all computations, for example the refractive index $n + ik$ and the absorption coefficient are both computed from the dielectric function. This is made possible by the assumption that the imaginary part of the dielectric function is proportional to the combined density of states of the valence and conduction band. In this manner the optical functions of the material like the optical absorption over the measured photon energy range, and the thickness of the film under consideration are achieved as end results of a simulation on transmission and reflection spectra measured simultaneously on the same spot of the sample.

The goodness of fit value is expressed as the deviation of the simulated spectra from the measured spectra. The values of goodness of fit for different categories are given in the table below.

Rating description	**Excellent**	**Good**	**Acceptable**	**Bad**	**Rejected**
Value	10^{-5}	10^{-4}	10^{-3}	10^{-2}	$\mathbf{10^{-1}}$

Table 3.1 Rating classification levels according to the deviation of the simulation from spectra.

From these values the uncertainty for any parameter of the fit were defined as follows:

$$\eta = \frac{\beta}{\psi} \times p\,, \tag{3.1}$$

where β is the difference between a perfect fit and the deviation value, ψ the rejection value and p the parameter in question.

Since the simplified construction described above yielded poor, unacceptable fits on the R and T spectra for the HWCVD μc-SiH series the modeling had to be adapted for improvement in accuracy. A rough surface was simulated by applying a mathematically defined function to allow for light scattering that occurs from the surface of the material, taking into account that scattering is higher at longer wavelengths than at shorter wavelengths. Then a two phased mixture of amorphous silicon and polycrystallites of silicon embedded in the amorphous silicon were defined. This was achieved by the effective medium approximation (EMA) introduced by Bruggeman [3.18]. The resulting material was then treated as a single bulk layer. If μc-Si is composed of a-Si and pc-Si with volume fractions f_a and f_{pc} respectively, then the effective dielectric function of the two phased μc-Si can be described as

$$0 = f_a \frac{\hat{\varepsilon}_{\mu c} - \hat{\varepsilon}_a}{\hat{\varepsilon}_{\mu c} + 2\hat{\varepsilon}_a} + f_{pc} \frac{\hat{\varepsilon}_{\mu c} - \hat{\varepsilon}_{pc}}{\hat{\varepsilon}_{\mu c} + 2\hat{\varepsilon}_{pc}}, \text{ where} \qquad (3.2)$$

$$\hat{\varepsilon}_{\mu c} = \varepsilon_{\mu c} - i\varepsilon_{\mu ci},\ \hat{\varepsilon}_a = \varepsilon_{ar} - i\varepsilon_{ai},\ \hat{\varepsilon}_{pc} = \varepsilon_{pcr} - i\varepsilon_{pci} \text{ and } f_a + f_{pc} = 1.$$

Here ε_a and ε_{pc} are the complex dielectric functions of amorphous silicon and the embedded pc-Si respectively, while $\varepsilon_{\mu c}$ is the complex dielectric function of the effective μc-Si. The dielectric functions of typical amorphous silicon and polycrystalline silicon are shown in figure 3.1.

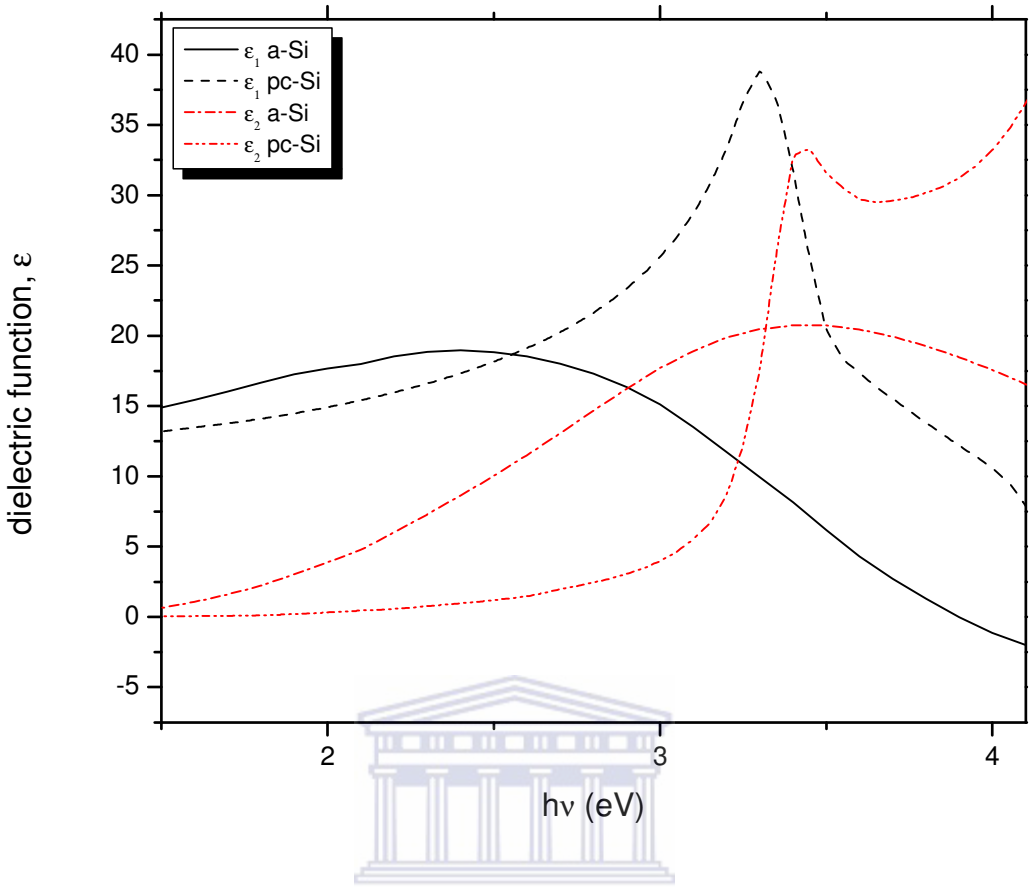

Figure 3.1 The dielectric functions of typical a-Si and pc-Si (ε_1 and ε_2 refer to the real and imaginary parts respectively).

The EMA is used again by mixing air into this new layer to approximate the presence of voids, and to account for oxygen in the films. This new mixture then constitutes the film that will be simulated and can account for the scattering of light inside the material. A simplified representation of the final mixture is shown diagrammatically in figure 3.2.

The optical properties of the new mixture are then extracted from the new effective dielectric function obtained from:

$$0 = f_{air}\frac{\hat{\varepsilon}_{porous}-\hat{\varepsilon}_{air}}{\hat{\varepsilon}_{porous}+2\hat{\varepsilon}_{air}} + f_{pc}\frac{\hat{\varepsilon}_{porous}-\hat{\varepsilon}_{\mu c}}{\hat{\varepsilon}_{porous}+2\hat{\varepsilon}_{\mu c}}, \text{ where} \qquad (3.3)$$

$$\hat{\varepsilon}_{porous} = \varepsilon_{porous} - i\varepsilon_{porousi},\ \hat{\varepsilon}_{air} = \varepsilon_{airr} - i\varepsilon_{airi},\ \hat{\varepsilon}_{\mu c} = \varepsilon_{\mu cr} - i\varepsilon_{\mu ci} \text{ and } f_{air} + f_{\mu c} = 1.$$

Here ε_{air} and $\varepsilon_{\mu c}$ are the complex dielectric functions of μc-Si and the embedded air in the μc-Si respectively, while ε_{porous} is the effective complex dielectric function of porous μc-Si.

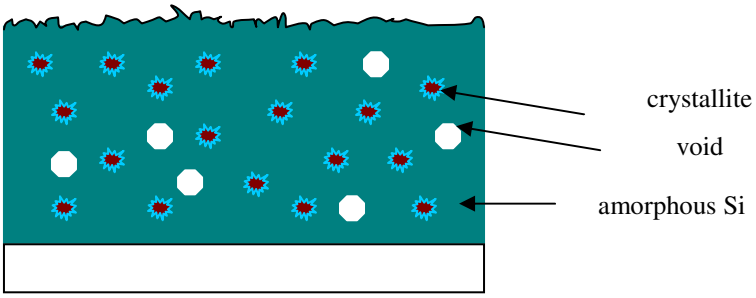

Figure 3.2 Simplified representation of three phased silicon layer.

3.3.2 APPLICATION OF THE MODEL-1.

The first application of the porous μc-Si model was on the relatively thin μc-Si PECVD film. The Raman scattering spectrum of the PECVD sample in figure 3.3 shows a definitive contribution of the 520 cm^{-1} vibration mode, indicating the crystallinity of the material and hence the applicability of an μc-Si model.

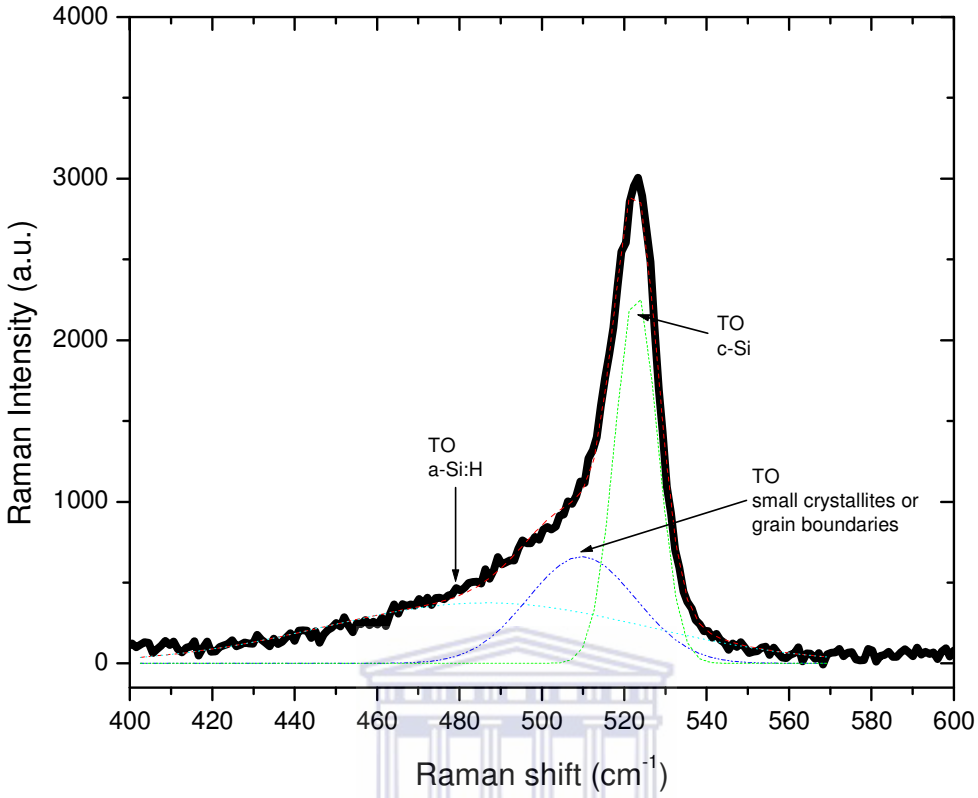

Figure 3.3 Raman scattering spectrum of the PECVD sample.

The results of the simulations on the transmission and reflection spectra are shown in figure 3.4.

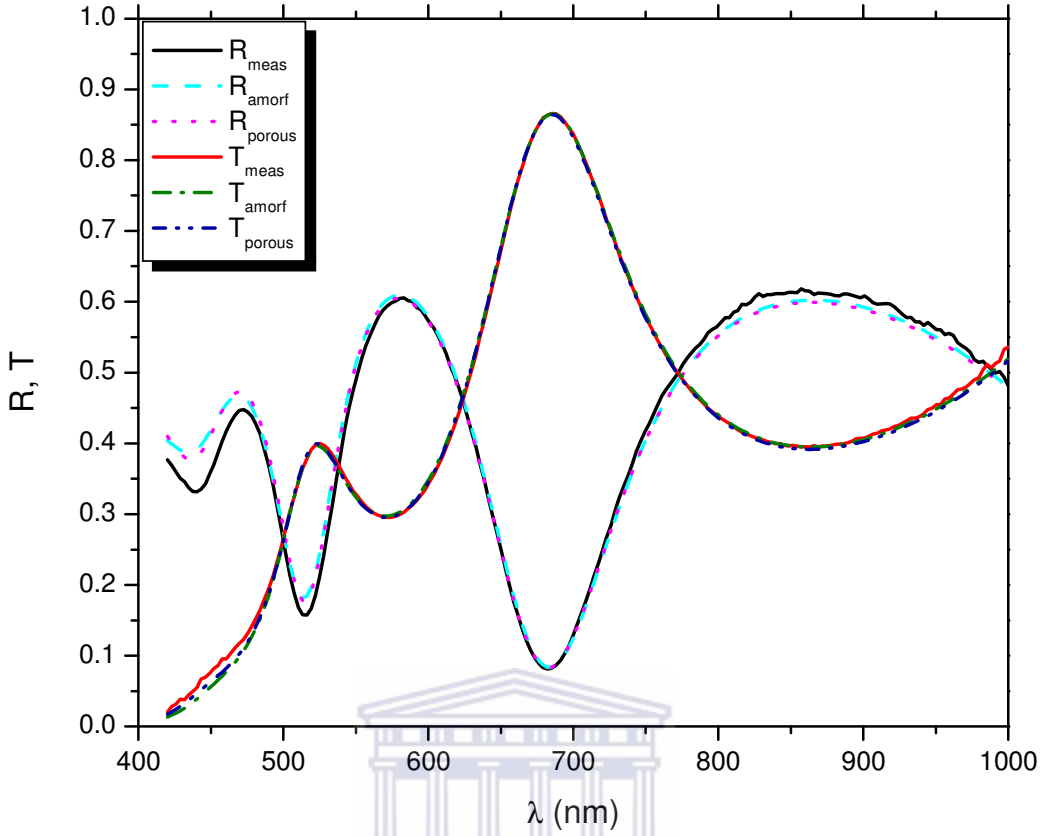

Figure 3.4 Measured and simulated R and T UV-Vis spectra with a pure a-Si fit and a one layer porous µc-Si fit..

The deviation associated with each fit is as follows: for the amorphous model it is 4.088×10^{-4}, and for treating the layer as a three phased material containing a-Si, polycrystallites and voids the deviation reduces to 3.806×10^{-4}. Thus an improvement of 6.9% in the value of the deviation was achieved when adapting the plain a-Si model to a µc-Si model. The accuracy of the fit is more evident for the regions of low and medium absorption for the transmission spectrum, while for the reflection spectrum it is more accurate for the region of medium absorption. The remaining regions for both spectra where the simulation does not follow the spectra that closely suggests that the single layer porous µc-Si model still needs to be tweaked to improve the accuracy of the fit.

3.3.3 THE OPTICAL MODEL-2.

As mentioned before, one of the main objectives was also to develop a versatile model to apply to films that underwent the metal induced crystallization process. Depending on the configuration of the metallization, the region of interest with respect to the metal layer could be the surface or region of silicon adjacent to the substrate. Thus three different regions of interest in the film can be identified during this process: the silicon region that was in direct contact with the metal layer, either on top of the a-Si:H or underneath it, and the bulk material. As the crystallization procedure normally involves a layer exchange mechanism, a great deal of uncertainty also exists regarding the retention of homogeneity across the film, namely that the surface layer or substrate-interface layer where the metal was in contact with the a-Si:H differ appreciably in electronic and optical properties from the bulk of the material after the annealing process and subsequent chemical etch. Similarly, three regions could also be postulated for the intrinsic μc-Si:H in case the optoelectronic properties differ in the substrate-interface layer, the bulk material and the surface layer. To that end, in the computer program the film was virtually split into the three afore-mentioned layers, each containing the adapted model that is inclusive of a-Si, polycrystallites and voids. The surface and substrate-interface layers were initialized to be roughly as thin as the Raman scattering depth of silicon layers, but the program was allowed to adjust the thickness of each of the three layers independently, adjusting all the parameters for each layer to describe the region best if any differences exist. A schematic of the three layers is shown in figure 3.5.

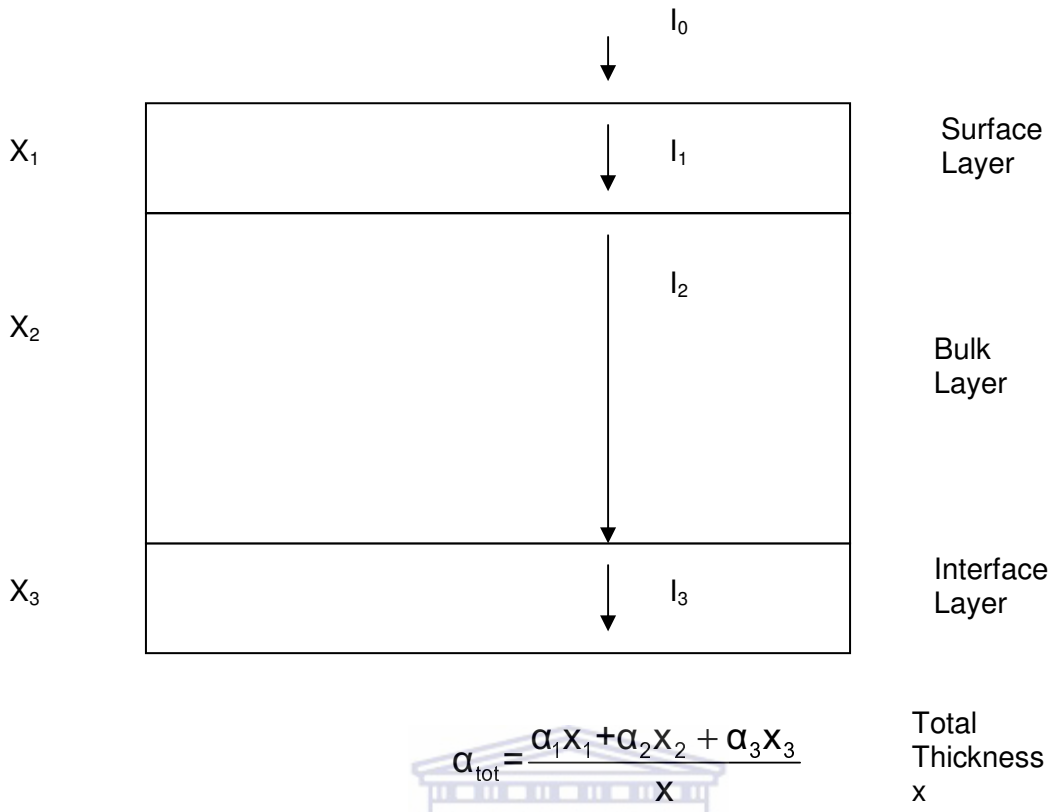

Figure 3.5 Schematic of radiation incident on the three layer system.

To investigate the effect that this virtual division of the layer may have on the absorption process, one has to consider a thin film of total thickness x on which the incident intensity of radiation is I_0. According to the Beer-Lambert Law the intensity of electromagnetic radiation after traversing the entire thickness of the film will be

$$I_{tot} = I_0 e^{-\alpha_{tot} x}, \tag{3.4}$$

where α is the absorption and x the thickness of the layer.

The complex refractive index of each layer in the whole film is:

$$\hat{n}_{total} = n_{total} - ik_{total}, \tag{3.5}$$

where n is the refractive index and k the extinction coefficient, is related to the dielectric function by

$$n = \sqrt{\frac{\varepsilon_{real} + \sqrt{\varepsilon_{real}^2 + \varepsilon_{imaginary}^2}}{2}}$$

and the absorption coefficient by

$$k = \frac{\alpha\lambda}{4\pi}, \tag{3.6}$$

where λ is the wavelength and α the absorption coefficient for each layer in the film.

If the film is virtually divided into three parts the absorption for the entire layer can be reconstituted by adding the weighted contribution of absorption for each layer.

3.3.4 APPLICATION OF THE MODEL-2.

The porous μc-Si three layer model was then applied to the PECVD sample and a further improvement in deviation value from the last improvement amounting to a 23.8% reduction was observed. The simulation produced thicknesses of 4.3 nm, 140.4 nm and 50.6 nm respectively for the surface layer, bulk layer and substrate interface layer. The contributions of the three layers to the absorption coefficient curve are shown in figure 3.6.

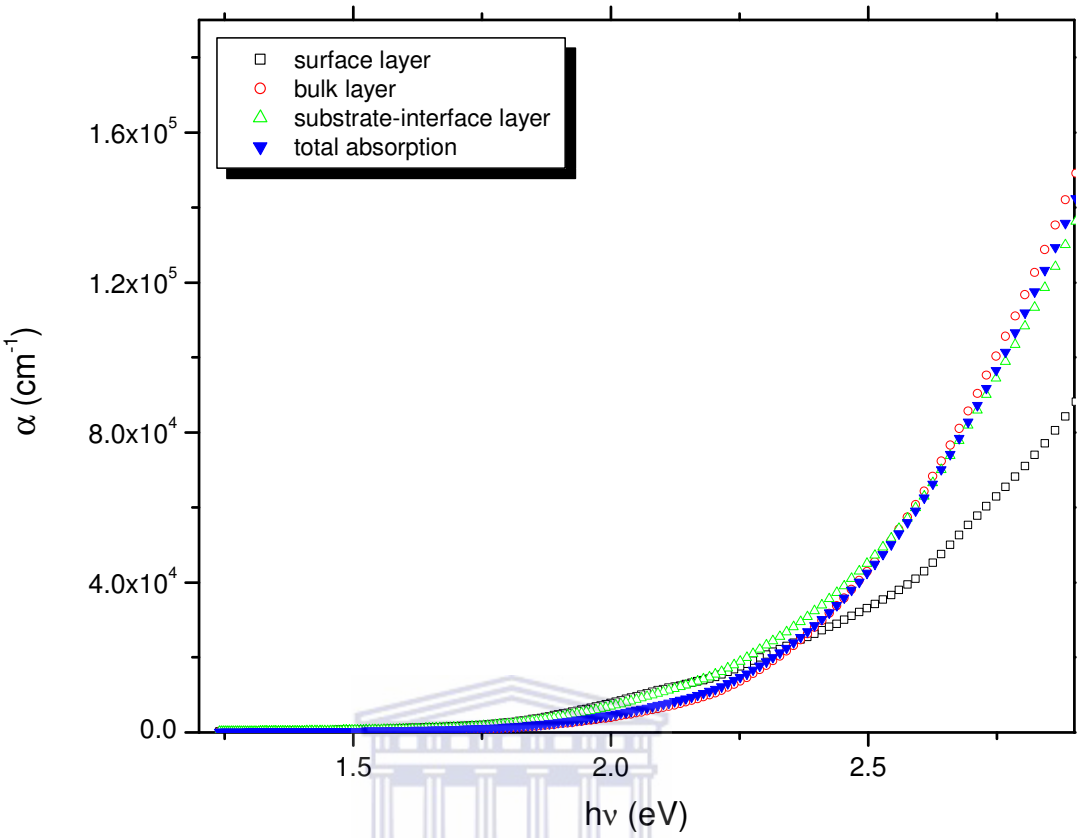

Figure 3.6 The contribution of each layer to the absorption coefficient.

From the spectra it is evident that the least absorption over the energy range takes place in the topmost, surface layer and that most of the radiation is absorbed in the bulk layer as expected. The absorption across the entire film is then determined almost wholly by the absorption in the bulk part of the film if the passage of light is not appreciably different in the other two regions of interest.

3.3.5 ANALYSIS OF THE HWCVD μc-Si:H SERIES.

Crystallinity

Figure 3.7 depicts the Raman scattering data of the HWCVD μc-Si:H series. R_c refers to the Raman crystalline ratio defined in section 3.2.

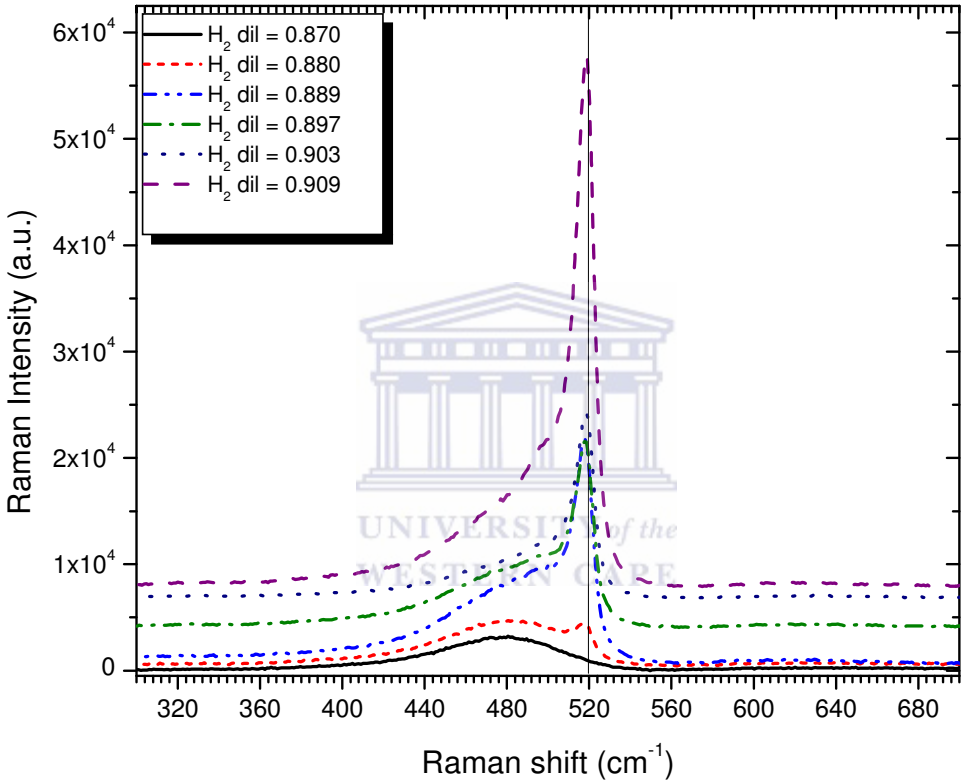

Figure 3.7 Raman shift data of the μc-Si:H HWCVD series.

An increase in crystallinity R_c is observed with increasing H_2 dilution in silane, with a shift of the 515 cm^{-1} peak towards 520 cm^{-1} with increasing crystallinity. From

$$d_{Raman} = 2\pi\sqrt{\frac{B}{\Delta\omega}}\ , \qquad (3.7)$$

where Δω is the shift in vibrational mode and B a constant [3.19], the average crystal size for the series was found to be ~ 4.5 nm.

The FTIR spectra of the series are shown in figure 3.8 to investigate oxidation effects .

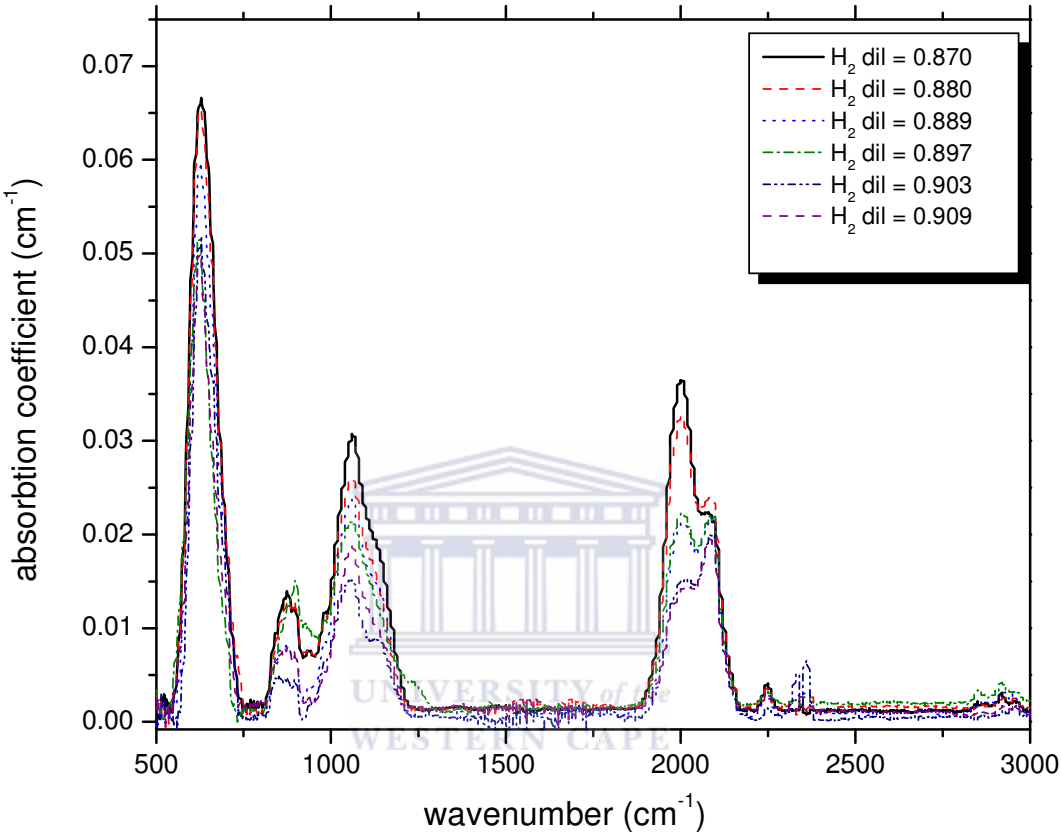

Figure 3.8 FTIR spectra of the HWCVD series.

The strong absorption bands in the region 920-1250 cm^{-1} is associated with the asymmetric Si–O–Si stretching vibration [3.20 – 3.21], whereas the peak centred around 2250 cm^{-1} is assigned to the H–SiO_3 vibration [3.22]. This could be indicative of an oxidation effect caused by a porous-like microstructure, which is a typical feature of nc-Si:H thin films, with oxygen bonding to the inside of the voids.

The 2250 cm^{-1} H–SiO_3 mode is evident for all the successive samples in the series, indicating the presence of oxygen in the films. This gives some measure of justification for mixing air into the silicon in the optical model for an approximation of the voids.

Application of the optical model on the HWCVD µc-Si:H series

In figure 3.9 the three optical models applied (amorphous single layer, single layer porous µc-Si, and three layer porous µc-Si) are evaluated for the deviation of the fit from the actual spectra on the basis of equation 3.1. In the figure R_c refers to the Raman crystalline ratio.

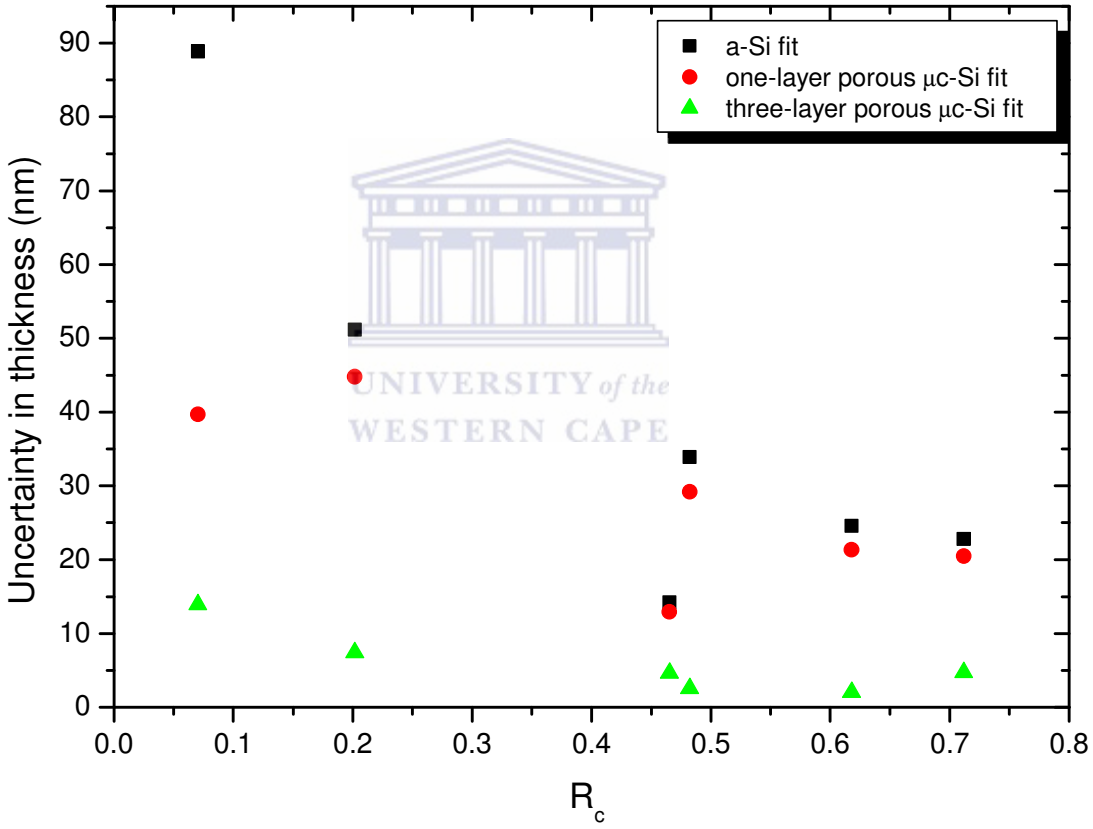

Figure 3.9 The improvement in accuracy if the virtual three layer system is used.

Here the thickness returned by the simulation of each model, a very important parameter, is given in terms of the uncertainty of each fit. The three layer porous µc-Si model clearly

reduces the uncertainty in thickness the most when it returns thicknesses that are associated with closer fits of the simulation to actual spectra. For this set of thick films of ~ 1500 nm it is also evident that the reduction in the associated uncertainty is greatest for the amorphous film and those with low crystallinity. Due to the great reduction in uncertainty when applying the three layer porous μc-Si model we adopt this method to best describe the optical functions of the series of films.

A separate calculation based on the method employed in reference [3.23] yielded rms surface roughness values of σ = 27.5, 15, 8.8, 8.3, 17.2 and 17.2 nm for the films in order of increasing crystallinity respectively. A useful optical calculation is the one-oscillator Wemple-DiDomenico equation [3.24]

$$n^2(h\nu) - 1 = E_D E_M / (E_M^2 - E^2), \tag{3.8}$$

where E_M is the single oscillator energy which is typically near the main peak of the imaginary part of the dielectric function ε_2. From the amorphous silicon and polycrystalline dielectric functions plotted in figure 3.1 the values are 3.45 and 3.65 eV respectively [3.25]. The refractive index over the energy range was extracted for each sample's three virtual regions and the relevant information for the WD relation calculated. These values are then compared with the parameters obtained when applying the envelope method of Swanepoel [3.5] on the transmission spectrum only. Extracting the refractive index of the different regions of the layer with the Scout® program makes it possible to track the passage of light in the film. The refractive index at long wavelengths, n_0, gives an indication of the optical density of the material. Figure 3.10 contains the refractive index behaviour over the energy range of the bulk layer of each film in the series, while figure 3.11 illustrates the refractive index of the surface and substrate-interface layers in, one graph.

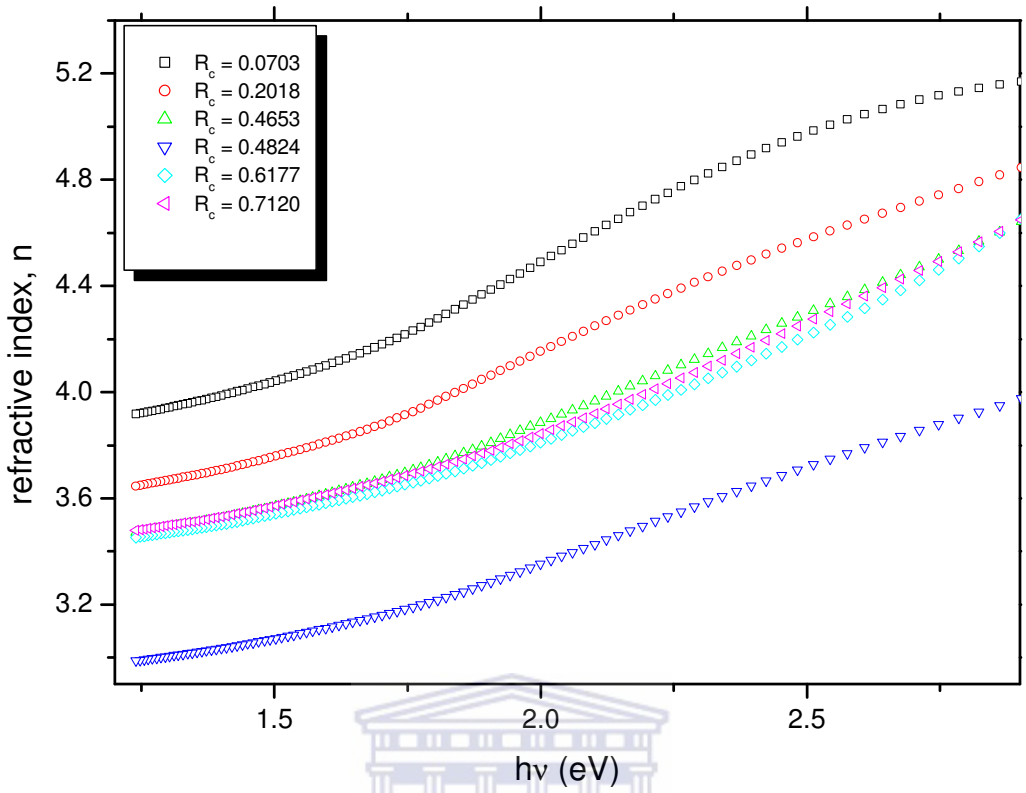

Figure 3.10 Refractive index over energy range in the bulk layers.

The bulk of the material is of course dominant in determining the optical properties of the whole film and it is generally accepted that microcrystalline silicon is less dense than amorphous silicon. The values of the refractive index of the films with higher crystallinity display in their bulk lower refractive index values than the films with lower crystallinity. The exception to this trend is the film with R_c ~0.48 which displays much lower refractive index values than even the high crystallinity films. This suggests that the film has different structural characteristics to the rest of the films in the series. We can now determine whether the refractive index values are different for the surface, and substrate-interface layer of each film compared to the bulk layer. This information is shown in figure 3.11.

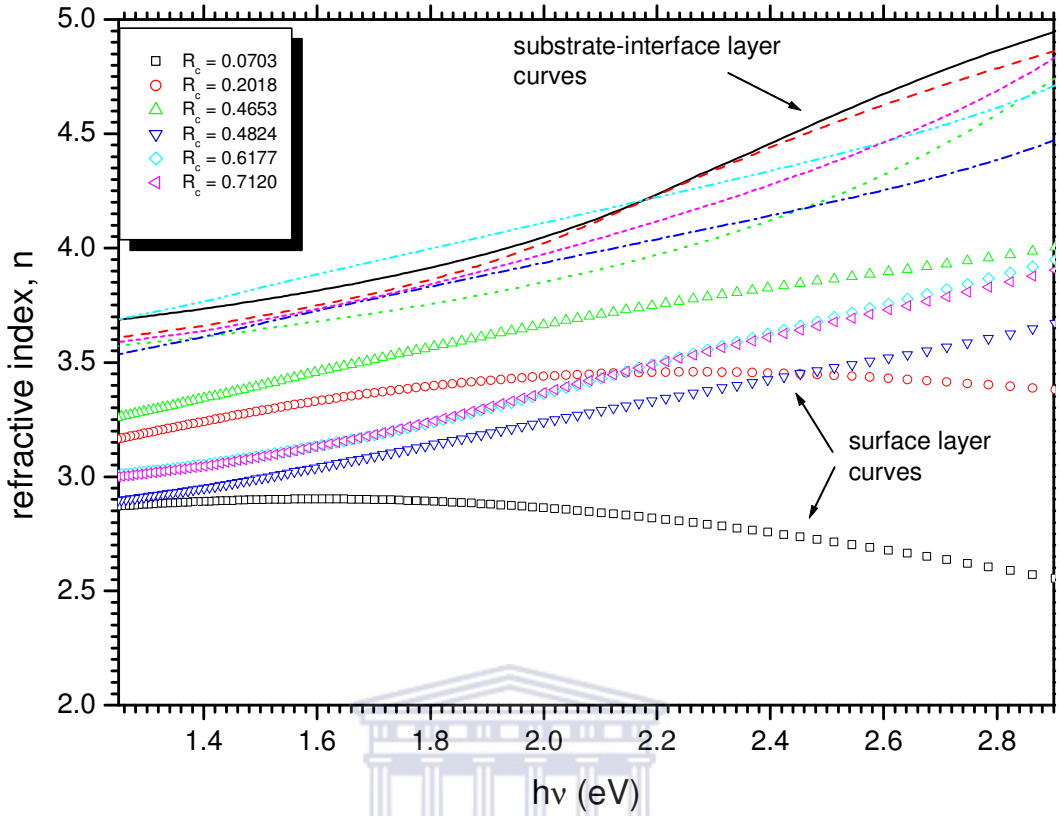

Figure 3.11 Refractive index over energy range in surface and interface layers.

The substrate-interface layer display refractive index values and shapes of the curves that are similar to those of the bulk layers of the films. However, the surface refractive index yields generally lower values than the substrate-interface, and bulk layers. For the films with $R_c < 0.48$ even uncharacteristic shapes for the refractive index dispersion can be observed. For the amorphous and low crystalline volume fraction samples the refractive index curves deviate from the normal silicon curves and only take on characteristic shapes as the crystallinity is increased to around 50%, the curves then resembling those of silicon. This implies that the passage of light through the upper layer is different for amorphous-like films compared to films that are highly crystalline. This could be related to the growth process through the densification of the network of atoms; termination of

the deposition process leaves the structures in the upper regions of the films incomplete with regards to the cross-linking process which densifies the material.

Table 3.2 contains various optical data. We have analysed the transmission spectra according to the Swanepoel method [3.5], and extracted a value for n_0 in addition to that obtained by analysing the Scout® results. The Swanepoel n_0 values on the films exhibit a general decrease with increasing crystallinity. However, we have determined n_0 for each of the three virtual layers. In the series, the surface layer n_0 suggests that the material in the upper part of the films is generally optically less dense than the bulk material, which confirms the expectation from the discussion above. For the bulk material, the n_0 values imply that the amorphous-like film is optically denser than the films of higher crystallinity, but the general trend of decreasing density with increasing crystallinity is upset by the sample with $R_c = 0.4824$, as evidenced from the lower value than for the rest of the films with crystallinity. This unusual behaviour can not so clearly be distinguished in the Swanepoel data for n_0. In general, the n_0 for the bulk and substrate-interface layers are comparable and higher than the Swanepoel values, and both show anomalous n_0 for $R_c = 0.4824$.

	n_0				E_M (eV)				E_D (eV)			
R_c	**Surf.**	**Bulk**	**Int.**	n_0 (Swa)	**Surf.**	**Bulk**	**Int.**	E_M (eV) (Swa)	**Surf.**	**Bulk**	**Int.**	E_D (eV) (Swa)
0.0703	2.80	3.69	3.51	3.49	5.11	3.56	3.97	4.10	34.8	44.8	45.0	45.9
0.2018	2.92	3.44	3.42	3.26	3.07	3.62	3.77	3.50	23.2	39.3	40.4	33.8
0.4653	3.01	3.29	3.42	3.21	3.07	3.69	4.22	3.71	24.7	36.1	45.2	34.6
0.4824	2.71	2.83	3.29	3.11	3.33	3.65	3.24	3.83	21.1	25.6	31.7	33.2
0.6178	2.84	3.28	3.43	3.15	3.62	3.82	3.27	3.83	25.6	37.3	35.2	34.1
0.7120	2.83	3.30	3.39	3.15	3.53	3.77	3.70	3.80	24.7	37.4	38.8	33.8

Table 3.2 Wemple-DiDomenico data for the HWCVD series.
(Swa refers to values calculated by applying the Swanepoel method).

A physical meaning attached to E_M is that it has also been extended to measure the energy difference between the 'centres of gravity' of the valence and conduction bands, indicative of an average gap of the material that is quantitative information on the ''overall'' band structure, differing from the conventional optical gap such as the Tauc gap which probes optical properties near the fundamental band gap of the material [3.26]. Localized states near the conduction or valence band (tail states) may have a strong effect on the optical absorption and subsequently on the optical gap, whereas if they have a small polarizability they will increase the Urbach tail but have little effect on the average gap [3.26]. The microcrystalline equivalent of the Urbach energy is normally higher than the value of amorphous silicon which is around 50 meV. There is a general increase in the single oscillator energy E_M in the bulk layer for increasing crystallinity in the series, but for the film with $R_c = 0.4824$. The dispersion energy E_D is a measure of the strength of interband optical transitions, and mass density information can also be deduced from it. From our data the anomalous sample at $R_c = 0.4824$ once again have a value in the

bulk that is lower than the rest of the values for the series. It behaves as a local mimimum for n_0 and energy values in the WD relation.

It is postulated that the surface layer for the amorphous film enhances light scattering similar to scattering off grain boundaries in a crystalline material, since the single-oscillator energy for the surface layer E_D is larger than the 4 eV of c-Si. This would imply that the upper amorphous surface layer should be very porous indeed compared to the upper layers of the rest of the samples in the series, as its bulk refractive index is quite high compared to the rest of the samples. Another fitting parameter extracted from the simulation is the void fraction of each layer. From figure 3.12 an inverse relationship for the surface layer can be distinguished between the void fraction and $n_{0,}$ the relationship between the amount of porosity and the optical density of the layer. The amorphous film exhibits high porosity in the upper layer and the sample of $R_c = 0.4824$ also stands out as the sample where the general trend is overturned, having implications for the optical properties like overall refractive index, absorption and bandgap of the whole film. The porosity in the upper layer for the other two crystalline films does not seem to affect the optical properties significantly, suggesting more homogeneous behaviour with the incorporation of crystals in the material.

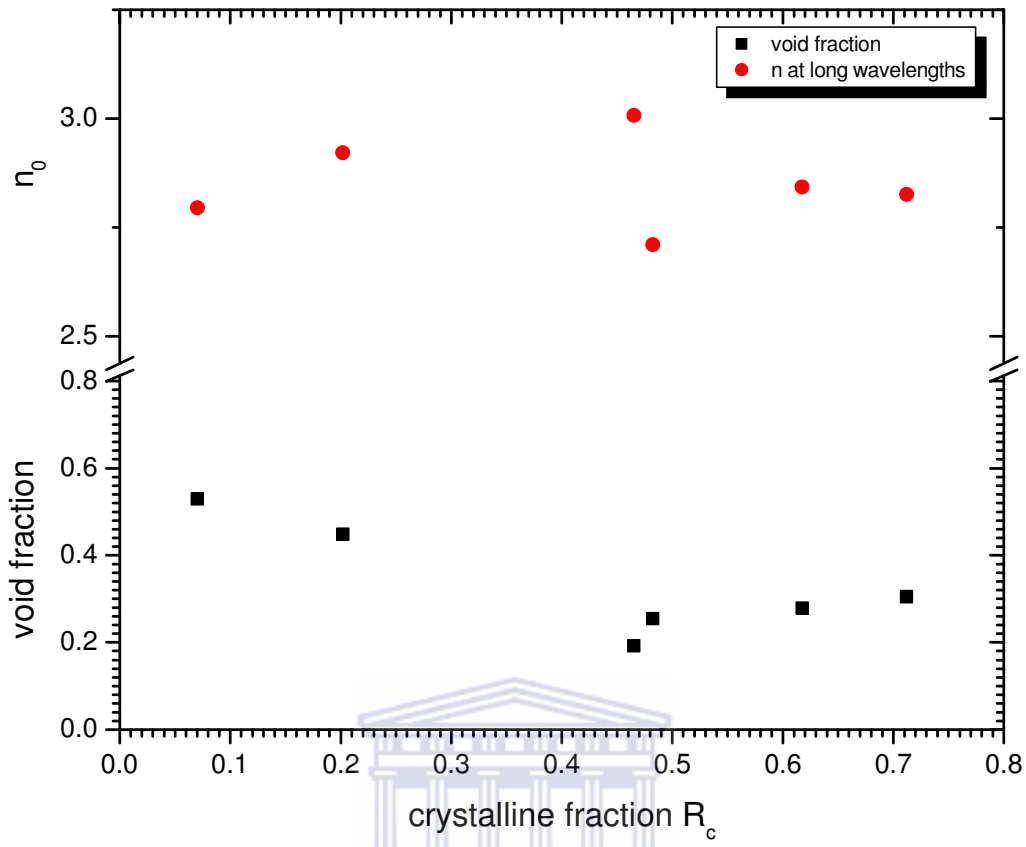

Figure 3.12 Surface layer n_0 and void fractions vs R_c.

Two samples were selected to investigate the absorption of the series. Previously, the a-Si fit in use at the time did not generate absorption curves of which the slopes in the Urbach region matched those of the PDS measured curves. Now, after the treatment described here, the overall absorption curves could be constructed by combining the RT absorption curves of the above band gap values with those of the sub bandgap values measured by PDS. The PDS spectra were normalized to the above-bandgap values generated from T and R and plotted on the natural log scale (ln pds). In addition, the contributions from the surface, bulk and interface layers are also displayed together with the effective absorption of the whole layer. Figure 3.13 displays the absorption curves for the amorphous sample and figure 3.14 displays the curves of the film with $R_c = 0.4824$.

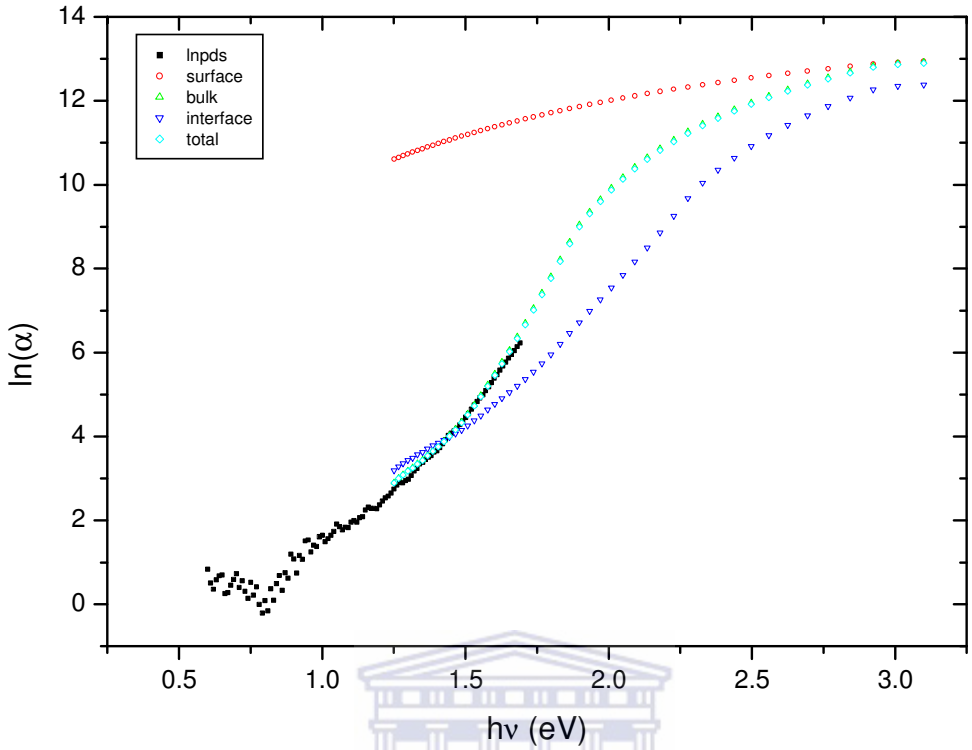

Figure 3.13 Absorption curves for the amorphous sample.

The effective absorption of the whole film follows that of the bulk layer, with enhanced absorption in the upper, more porous layer due to enhanced light scattering in that layer. This is different than in the case for the more crystalline sample in figure 3.14, where R_c = 0.4824.

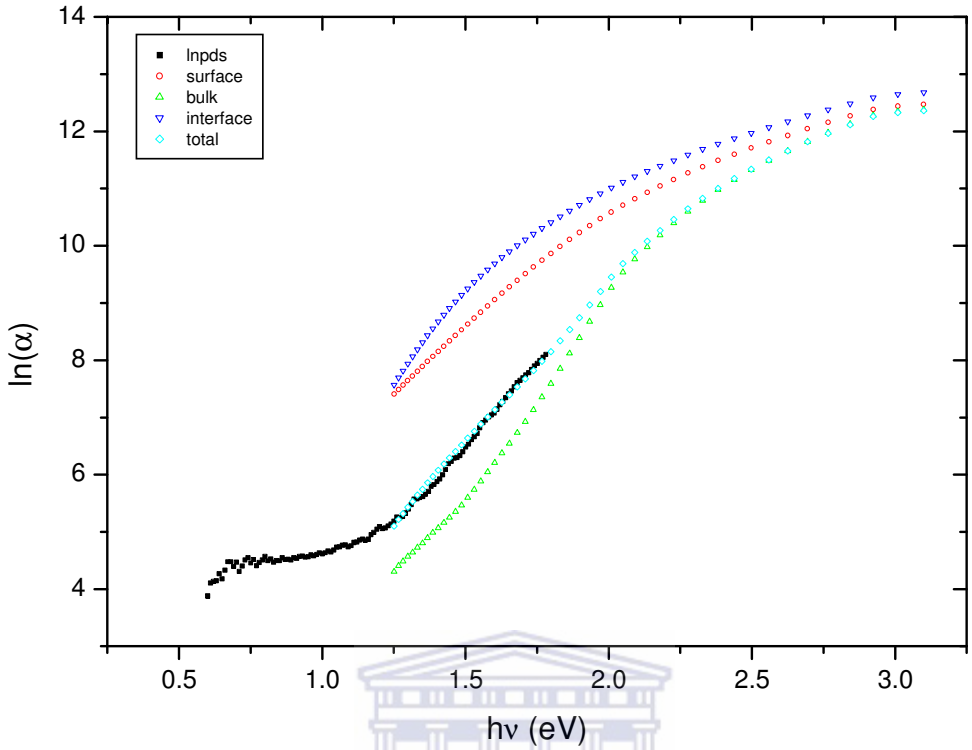

Figure 3.14 Absorption curves for the film with R_c = 0.4824.

For this sample the absorption in the substrate-interface layer is greatest, probably due to morphological differences in the layer at different depths. For the rest of the series, it only remains to be said that the general trend for series is that the absorption coefficient decreases over the energy range as the films increase in crystallinity. For the film of highest crystallinity the three regions exhibit markedly similar absorption. Thus the new model offers some explanation why the specific sample seems to upset general trends.

To investigate sub-bandgap absorption one has to fix an energy band gap for the material. The Tauc relation was used to determine an energy band gap value for the samples in question and is generally less than the value of E_{04}, the energy at which the absorption coefficient equals 10^4 cm^{-1}. For the samples in order of increasing crystallinity these

values of E_{04} are 1.93, 1.93, 1.97, 1.98, 1.96, and 1.96 eV respectively. In figure 3.15 the equivalent values are 1.83, 1.79, 1.83, 1.83, 1.83 and 1.87 eV respectively. We thus have four values centred around 1.84 eV, one value at 1.79 eV and one value at 1.88 eV. With the data that the Swanepoel method generated the Tauc method of $[\alpha n(h\nu)]^{1/2}$ vs $h\nu$ yielded band gap values of as high as 2.2 eV. Differences in the numerical calculation methods of the band gap are discussed in references [3.7, 3.27], particularly the effect of the omission of the refractive index from the product $[\alpha n(h\nu)]$, using $[\alpha/(h\nu)]$ in place of the product, and the total suppression of interference fringes in the spectra. This, in order to arrive at more accurate bandgap values.

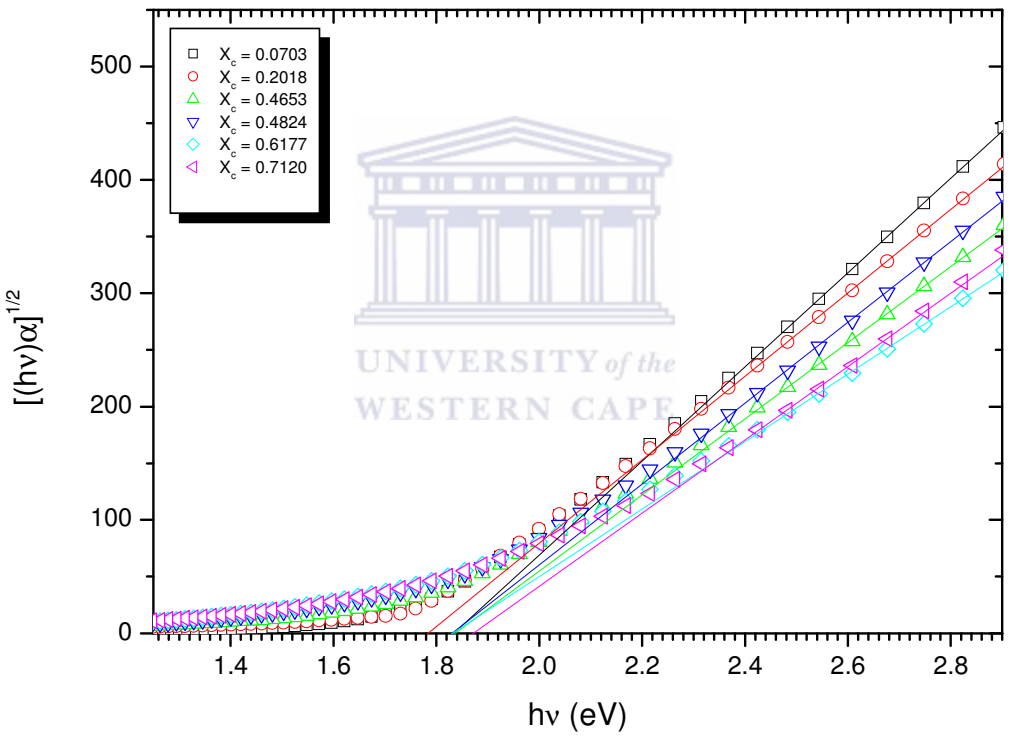

Figure 3.15 Determination of band gap from $[\alpha(h\nu)]^{1/2}$ vs $h\nu$.

However, the method proposed in this work managed to make the virtual material more realistic and hence reduced values for band gaps are achieved. It now depends on the preference in the choice of energy gap value where the regions of interest will be in the

PDS spectrum. This allows for further work to calculate the defect density from the sub-bandgap absorption region at a later stage.

3.4 CONCLUSION

The effective medium approximation was utilized to analyse optical reflection and transmission spectra for μc-Si:H films. Porosity and crystallinity were built into the optical model, with scattering from the surface incorporated, assuming a homogenous distribution of particles and voids in the film. The optical model was then tested on a μc-Si:H thin film on Corning glass. The fitting result was compared to that of an amorphous model, which resulted in a 6.9% improvement in the deviation of the simulation from the spectrum. The new model was then further refined to include three regions in the depth of the film with varying structural properties. This was done to supply a framework that may be extended and built upon when analyzing crystallized silicon thin films obtained by metal induced crystallization. The new optical model using a three layer system yielded a further improvement in the deviation of ~24%.

The model was then applied to a microcrystalline series that was suspected to be porous since the reflection and transmission spectra could only be fitted poorly, giving inaccurate optical properties. Very good fitting results were obtained on this set of samples, leading to the calculation of more accurate optical parameters like the absorption of light in the material. Specifically, due to the inclusion of porosity in the films, we could show that that the one film in the series exhibited optical properties that were at odds with trends in the rest of the films in the series. The mixing of the dielectric function of air with that of Si allowed us to make a conclusion that the film in question is highly probable to be porous in nature. This is a fast method for the screening of Si materials in terms of varying optical properties.

REFERENCES

3.1 J. Meier, P. Torres, R. Platz, S. Dubail, U. Kroll, J. A. ana Selva, N. Pellatou Vaucher, Ch. Hof, D. Fischer, H. Keppner, A. Shah, K. D. Ufert, P. Giannoules, J. Koehler, Mater. Res. Soc. Symp. Proc. 420, (1996) 3

3.2 M. van Veen, PhD thesis, Utrecht University (2003)

3.3 F. Siebke, S. Yata, Y. Hishikawa, M. Tanaka, J. Non-Cryst. Sol. 227-230, (1998) 977

3.4 H. Li, Utrecht University, private communication

3.5 R. Swanepoel, J. Phys. E: Sci. Instrum. (16), (1983) 1214

3.6 M. Mulato, I. Chambouleyron, E. G. Birgin, J. M. Martinez, Appl. Phys. Lett. 77 (14), (2000) 2133

3.7 Y. Hishikawa, N. Nakamura, S. Tsuda, S. Nakano, Y. Kishi, Y. Kuwano, Jap. J. Appl. Phys. 30 (5), (1991) 1008

3.8 C. J. Arendse, G. F. Malgas, T. F. G. Muller, D. Knoesen, C. J. Oliphant, D. E. Motaung, S. Halindintwali, B, Mwakikuaga, Nanoscale. Res. Lett. 4, (2009) 307

3.9 K. H. Jun, R, Carius, H. Stiebig, Phys. Rev. B 66, (2002) 115301

3.10 A. Gordijn, J. K. Rath, R. E. I. Schropp, Appl. Phys. Lett. 85 (21), (2004) 5096

3.11 www.mtheiss.com

3.12 P. C. P. Bronsveld, H. J. Van der Wagt, J. K. Rath, R. E. I. Schropp, W. Beyer, Thin Solid Films 515, (2007) 7495

3.13 M. H. Brodsky, M. Cardona, J. J. Cuomo, Phys. Rev. B16, (1977) 3556

3.14 N. Maley, Phys. Rev. B 46 (4), (1992) 2078

3.15 E. Ullersma, PhD thesis, Utrecht University (1998)

3.16 F. Neri, G. Saitta, S. Chiofalo, J. Phys. E.: Sci. Instrum. Vol (20) (1987) 894

3.17 S. K. O'Leary, S. R. Johnson, P. K. Lim, J. Appl. Phys. 82 (7), (1997) 3334

3.18 D. A. G. Bruggeman, Ann. Phys. 24, (1935) 636

3.19 Y. He, C. Yin, G. Cheng, L. Wang, X. Liu, G. Y. Hu, J. Appl. Phys. 75, (1994) 797

3.20 B. G. Yacobi, R. W. Collins, G. Moddel, P. Viktorovitch, W. Paul, Phys. Rev. B 24 (10), (1981) 5907

3.21 I. Montero, L. Galan, O. Najmi, J. M. Albella, Phys. Rev. B 50, (1994) 4881

3.22 G. Lucovsky, J. Yang, S. S. Chao, J. E. Tyler, W. Czubatyi, Phys. Rev. B 28, (1983) 3225

3.23 E.Dobierzewska-Mozrzymas, E. Rysiakiewiccz-Pasek, P. Bieganski, J. Polanskaand, E. Pieciul, J. Non-Cryst. Sol. 354, (2008) 3241

3.24 S. H. Wemple. M. DiDomenico, Phys. Rev. B (3), (1971) 1338

3.25 Database of optical functions, Scout® software

3.26 S. Vignoli, R. Butte, R. Meaudre, M. Meaudre, P. Roca I Cabarrocas, J. Phys.: Condens. Matter 11, (1999) 8749

3.27 R. H. Klazes, M. H. L. M. Van den Broek, J. Bezemer, S. Radelaar, Phil. Mag. B 45, (1982) 377

CHAPTER 4

Thermal annealing of protocrystalline a-Si:H

4.1 INTRODUCTION

The characteristic disorder of a-Si gives rise to unique properties such as high absorption coefficient that allows use of a thin film to absorb the sunlight in a solar cell structure. The a-Si is also characterized by weak, strained and dangling bonds that impede carrier transport [4.1]. The presence of hydrogen in a-Si removes dangling bond defects, and by using a dilute mixture of silane in hydrogen during the chemical vapour deposition superior properties can be obtained. In fact, the best amorphous silicon is grown just below the edge of the amorphous to microcrystalline transition. This distinctive class of a-Si:H materials was described by Mahan *et al.* [4.2 – 4.4] when they found that the short range order (SRO) as determined by Raman spectroscopy does not change but order on a longer or medium range scale (MRO) changes. This was apparent from the full width at half maximum (FWHM) of the first XRD peak for a-Si: H, centred at a scattering angle of ~28.5°. The narrowing of this width was seen as an indication of improved medium range ordering.

A model was proposed which consist of a nanocrystalline silicon configuration where nanocrystallites resides in a background matrix of a-Si:H; the configuration was generated with molecular dynamics simulations [4.2 – 4.4]. The model was similar in structure to that of a-Si:H grown near the amorphous/microcrystalline phase boundary in that it contains small crystallites. The local structural order of the model varies

continuously as a function of R (the distance from the centre of the crystallite). For atoms residing within a small radius R within the crystallite, the local order is very similar to c-Si, with minimal bond angle and bond length distortions. As shells of increasing radius r are considered the local short-range order exhibited by atoms residing within these shells continuously decreases from a near crystalline to an amorphous character. Thus protocrystalline silicon material has a high degree of order that implies vanishingly small bond-angle-distortion [4.1]. Protocrystalline silicon is clearly an exceptional material, as a final stabilized efficiency of ~ 9.6% in the n-i-p configuration [4.5] solar cell incorporating protocrystalline silicon as the i-layers, attests.

The proto material still falls within the a-Si:H class, but the exact nature of these transition region materials is not yet fully understood. It is known that both the atomic hydrogen concentration and structural disorder in a-Si:H are important factors in determining the eventual stability of the material [4.6]. The optical band gap of a-Si;H is related to the electronic structure of the material and the solar cell efficiency is directly related to it. Moreover, the band gap is dependent on both the hydrogen content and structural disorder [4.7 – 4.11]. It is therefore important to investigate the optical band gap of protocrystalline silicon in this regard. Since the deposition regime is exclusive to a specific deposition system it is difficult to compare films from a range of deposition conditions from the same deposition chamber. In order to study the relations between hydrogen concentration, optical parameters, and the disorder we therefore chose to anneal HWCVD protocrystalline silicon to investigate the displacement of bonded hydrogen from the film, the microstructure, optical band gap and order of the network.

4.2 EXPERIMENTAL DETAILS

Hydrogenated amorphous silicon (a-Si:H) in the protocrystalline regime was deposited by the hot wire chemical deposition (HWCVD) process in the PASTA chamber at Utrecht University. Deposition conditions were used that normally yield protocrystalline silicon for intrinsic layers of the order of 500 nm – 1 μm [4.12]. Transparent 10 cm × 10 cm Corning 2000 glass was used for the optical measurements, while c-Si substrates were

used for FTIR measurements. The large area sample was then cut into smaller 1 cm × 1 cm samples and the average thickness of the smaller a-Si:H samples was determined to be 470 nm with the optical reflection and transmission fitting procedure, described previously. A conventional tube furnace with nitrogen ambient was used for isochronal annealing. Annealing times of 30 minutes were applied for a temperature series of 150, 250, 350, 450 and 520°C, while a separate anneal for six hours at 520°C was also performed.

Raman Spectroscopy was used to obtain information about the crystalline nature of the silicon thin films, while for the UV-Vis characterization reflection and transmission spectra were analysed. The sub-bandgap absorption was measured with the photothermal deflection spectroscopy (PDS) technique. FTIR measurements were performed on films deposited on c-Si substrates.

4.3 RESULTS AND DISCUSSION

Raman scattering is a method to detect the extremely minute changes in the small-range order of the amorphous network. Like infrared spectroscopy it measures the vibrational density of states; from this information the root-mean-square bond angle variation in the amorphous network, which is a measure of the disorder of the network, can be calculated. For c-Si the conservation of crystal momentum requires that the wave vector $\vec{k} \sim 0$. This restriction causes a sharp, narrow peak at ~ 520 cm^{-1} in the Raman spectrum [4.13]. The absence of this peak verifies that there is no crystallinity present in the a-Si:H film.

Relaxation of the momentum conservation selection rule for a-Si occurs due to the network disorder. A broad band centered at about 470 – 480 cm^{-1} becomes visible. The transverse-optical peak (TO) in the vibrational density of states reflects the degree of disorder in the amorphous system. Equivalently it reflects the short-range order. The relation between the full-width-half-maximum (FWHM) of the transverse-optical (TO) peak, Γ, and the root-mean-square bond angle variation, $\Delta\vartheta_b$ is given by [4.14]:

$$\Gamma/2 \cong 7.5 + 3\Delta\varphi_b \tag{5.3}$$

where Γ and $\Delta\vartheta_b$ are measured in cm^{-1} and degrees, respectively. The range for a-Si:H films of the bond-angle variation is 7.0 to 14.1° [4.7].

The Raman crystalline ratio of the material R_c, is defined as

$$R_c = \frac{I_{505} + I_{520}}{I_{480} + I_{505} + I_{520}}, \tag{5.4}$$

with I_x the integrated absorption at the mode x from the spectrum and specifically, I_{505} the shifted signal from grain boundaries.

Structural disorder in a-Si:H is known to influence its electronic quality. From Raman scattering measurements the structural disorder can be quantified from the root-mean-square bond angle variation. Street [4.15] has investigated the effect of hydrogen on the disorder of the amorphous network; and argued that hydrogen incorporation provides more structural flexibility to the amorphous network, which may lead to a reduction in bond angle variation. Studies [4.7] have suggested that maximally ordered and maximally disordered networks have values of 7.0 to 8.2° and 11.0 to 14.1° for $\Delta\vartheta_b$, respectively.

Raman spectroscopy confirmed that the as-deposited material in this series under study were amorphous at deposition due to the absence of the transverse-optic (TO) mode of crystalline silicon at 510 - 520 cm^{-1}. The spectrum of the as-deposited material is shown in figure 4.1.

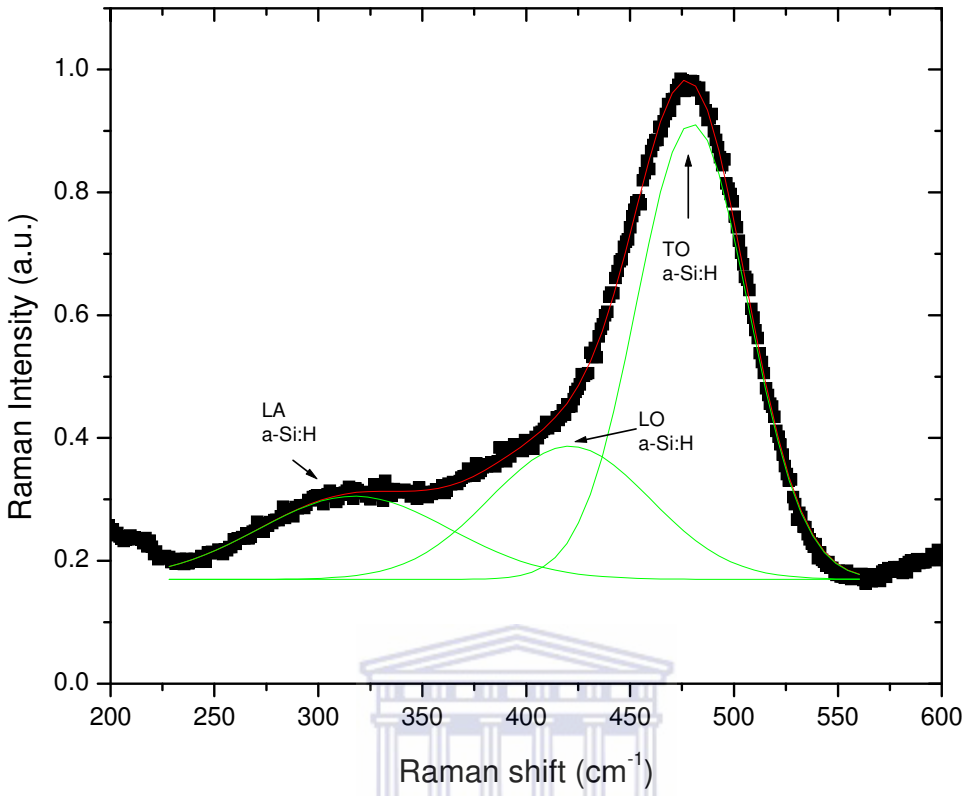

Figure 4.1 Raman spectrum of the as-deposited film.

The disorder value Γ obtained from the fit of the different optical modes for a-Si:H as shown in figure 4.1 is 53 cm^{-1}. This corresponds to a bond-angle variation of 6.4°, well below the range of values mentioned for a-Si:H by HWCVD [4.2]. This implies that the material is in such a highly ordered state that it could be considered to be locked in a transition state just before crystallization occurs. Upon annealing at a low temperature of 150°C, the Raman spectrum in figure 4.2 reveals an interesting detail; that of a slight contribution of the proportion of the spectrum centred around the TO mode of crystalline silicon at 519.7 cm^{-1}. It appears that some of the material in the film is now in the crystalline state with crystallite size detectable by Raman spectroscopy. It would thus be expected that annealing at higher temperatures should produce similar results.

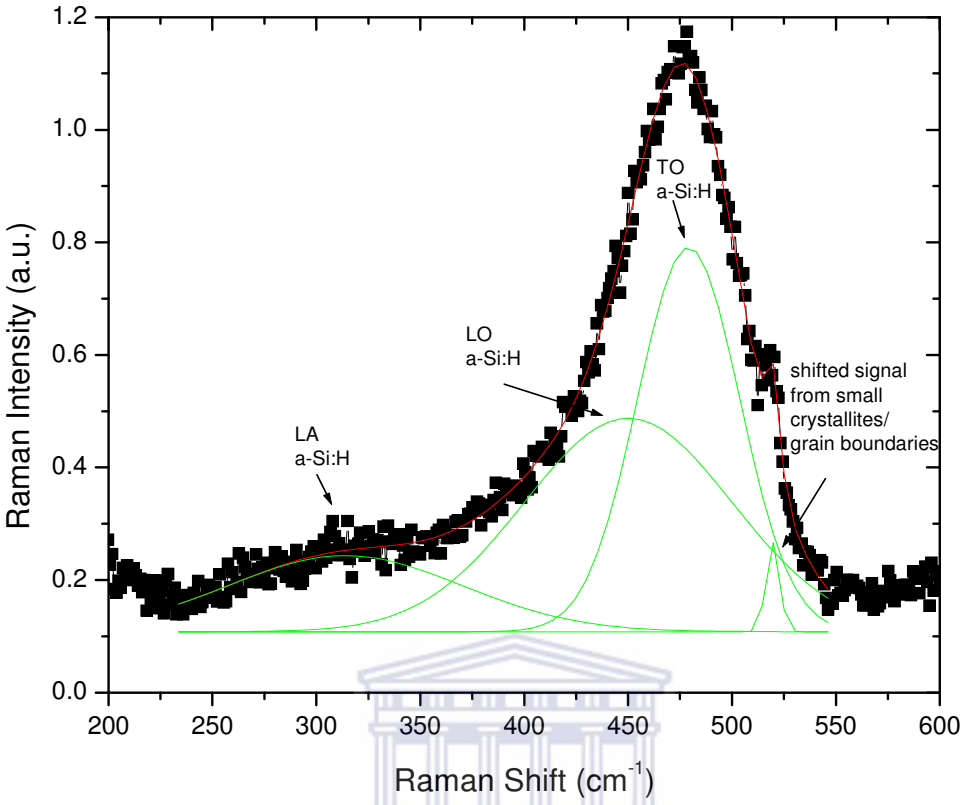

Figure 4.2 Raman shift spectrum of a-Si:H annealed at 150°C.

However, no c-Si TO modes after annealing at higher temperatures, 250°C to 520°C are evident in the Raman spectra for these samples, even if the films remain highly ordered, as evidenced by a narrow width Γ for all these spectra. Since protocrystalline a-Si:H is a material with unusual characteristics, it is not surprising that the annealing results defy the expectations and certain anomalies arise. The optical properties of the films in the series were therefore extracted using the program Scout®; the OJL model was adapted from amorphous to one that included both crystalline regions and voids, described in the previous chapter, using the Bruggeman Effective Medium Approximation and slicing the film into three virtual regions: the surface, bulk and interface regions. Scattering due to surface roughness was also taken into account. Additionally we intend to establish

whether the dielectric function of polycrystalline silicon is sensitive to the presence of small nano-crystallites in the films, as Raman spectroscopy was unable to detect crystallization during the course of the annealing process for higher temperatures. A schematic representation of crystallite incorporation in the film for the optical model is shown in figure 4.3. The ordered/crystallized regions could have crystallinity as a function of depth dependence.

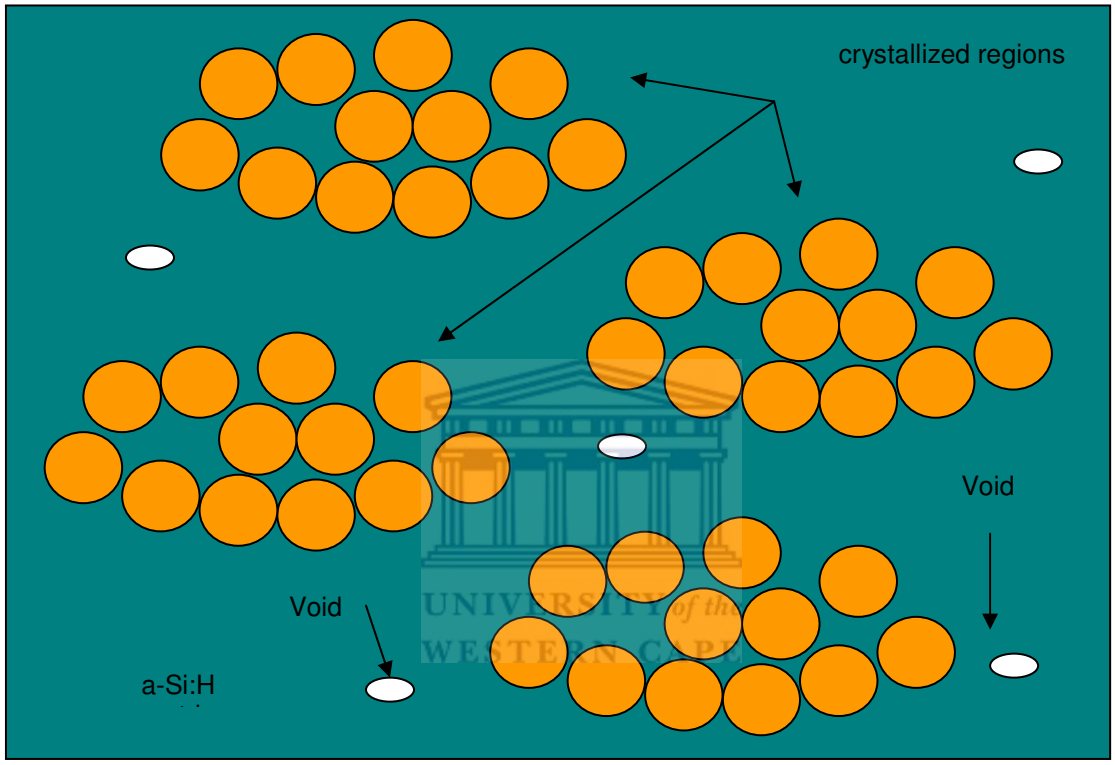

Figure 4.3 Schematic representation of the film.

Crystallinity derived from the UV-Vis optical modeling places a different perspective on the series of films. At first glance the crystallinity in the film is not a large number, but it is detected nonetheless. In the absence of corroborative results from Raman scattering or XRD it can be concluded that small crystallites, undetectable by conventional means are sparsely distributed throughout the films. Figure 4.4 gives an indication of the total film crystallinity.

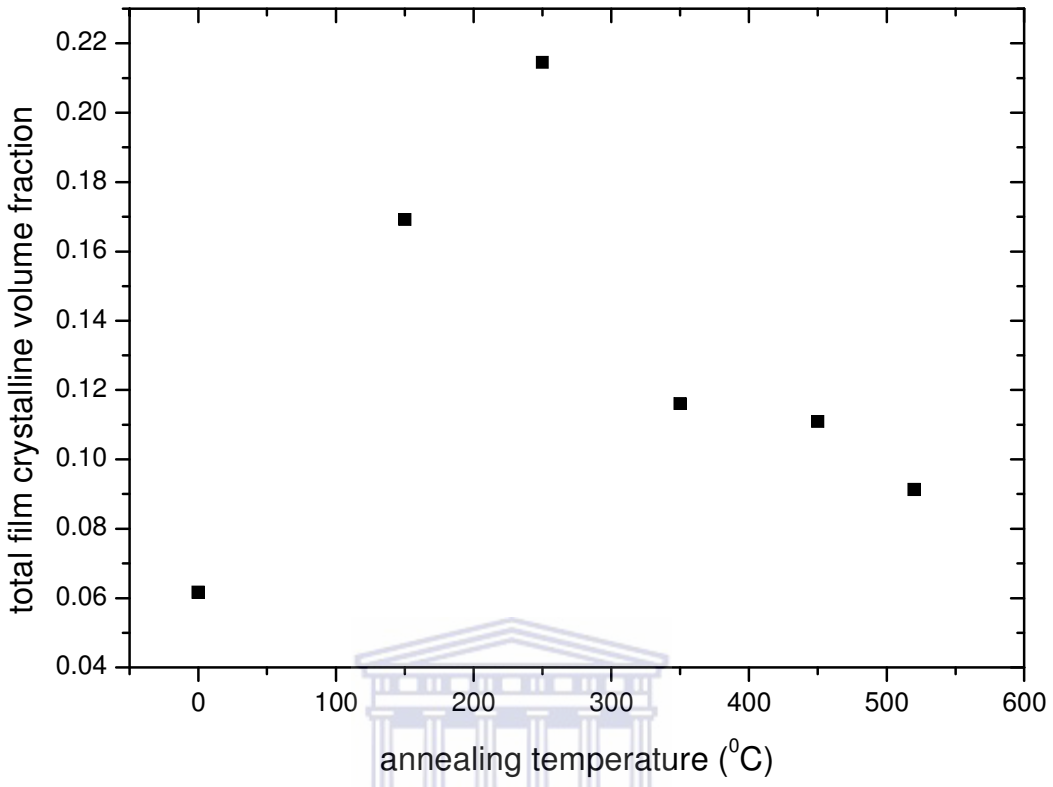

Figure 4.4 Crystallinity in the film at different annealing temperatures.

UV-Vis film crystallinity is highest at an annealing temperature of 250^0C. The expectation would have been that the film crystallinity would increase with increasing annealing temperature. However, the film crystallinity decreases again at the higher annealing temperatures. If the properties of the films depended only on film crystallinity then the 250^0C annealed film should exhibit slightly different optical properties than the rest of the films in the series. However, the information that can be extracted from the optical modeling also allows for the separate crystallinities in the three virtual layers to be ascertained. Surface layer crystallinity was increasing between 150 and 350°C. It then stabilized at higher annealing temperatures, as shown in figure 4.5. For the virtual surface layer the thickness ratio of the surface layer to total film thickness is less than 14%, which amounts to 52 nm for the un-annealed film and ~30 nm for the annealed films.

Furthermore, the existence of such high crystallinity in the thin surface layer may give rise to the overall ordered nature of the silicon atoms in the matrix, as probed by Raman scattering and X-ray diffraction, which show up as amorphous signatures due to the very small crystallites. Here the films of low hydrogen concentration, as found in the initial study by Mahan et.al. [4.3 – 4.4] for both HWCVD and PECVD which were referred to as protocrystalline or 'on the edge', comes to mind. Specifically our annealed films may exhibit the ordered regions deficient of hydrogen or hydrogen bound to very small crystallites. Our optical modeling could be a powerful tool in an enhanced description of this type of material.

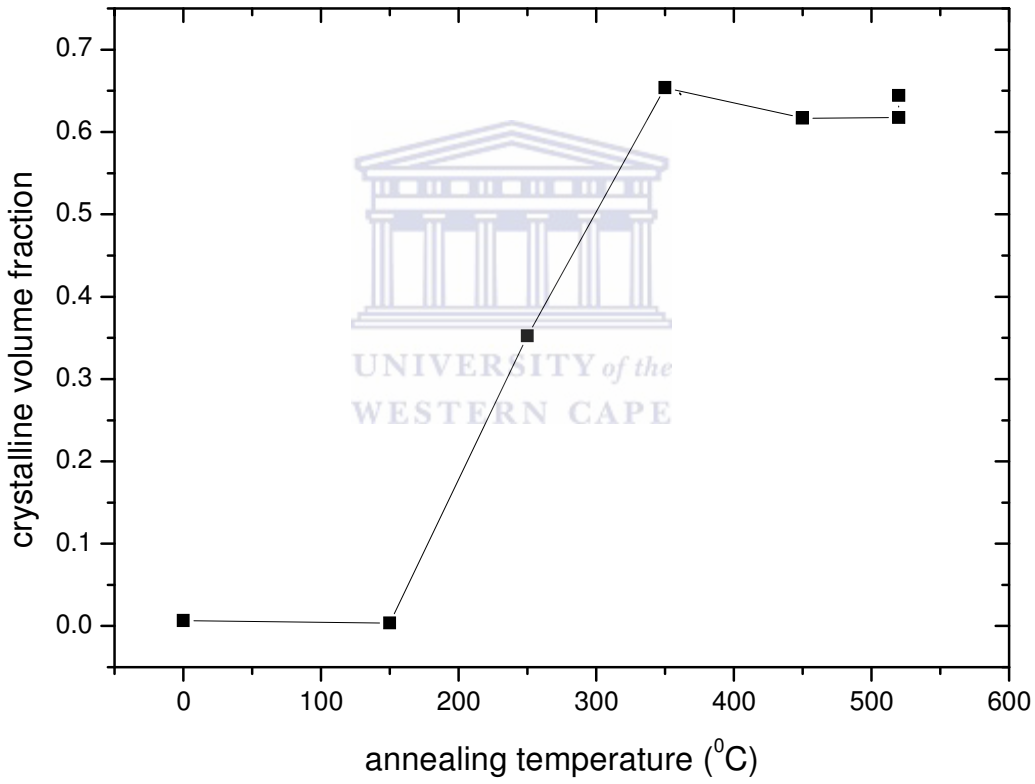

Figure 4.5 Crystalline volume fraction in surface layer vs annealing temperature.

Once again, the trend observed from figure 4.5 prompts an expectation that a change-over in the optical properties in the annealing temperature region of 150°C - 350°C should occur if the crystalline volume fraction is the driving parameter influencing the optical properties of the surface layer. We should, however consider other factors which may influence the optical properties, such as the amount of porosity in the surface layer, which plateaus at a value of less than 5% over the annealing temperature range such that no great changes in porosity of the surface layer are manifested. The role of the bonded hydrogen in its various bonding configurations may also play an important role in the optical properties. The refractive index of the surface layer, for the first three annealing temperatures, is shown in figure 4.6.

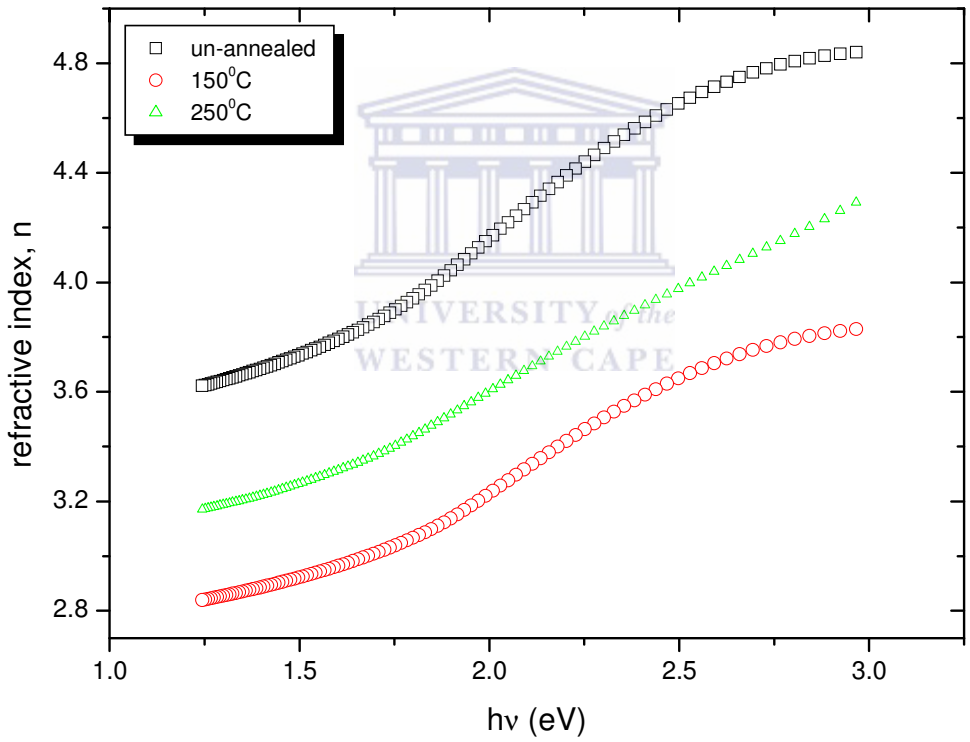

Figure 4.6 Refractive index dispersion in surface layer vs energy.

The expected downward trend in refractive index dispersion for increasing annealing temperature is arrested at the annealing temperature of 250°C. At higher annealing

temperatures no clear trend is observed, probably due to some of the reasons mentioned above. This shows that the optical properties of the film annealed at 250°C are different to expectations, in view of the changeover in surface layer crystallinity, the maximum value for total film crystallinity, and the associated changes in surface layer refractive index. The hydrogen concentration and possible bonding configurations were also investigated for possible influence on the optical properties of the annealed material.

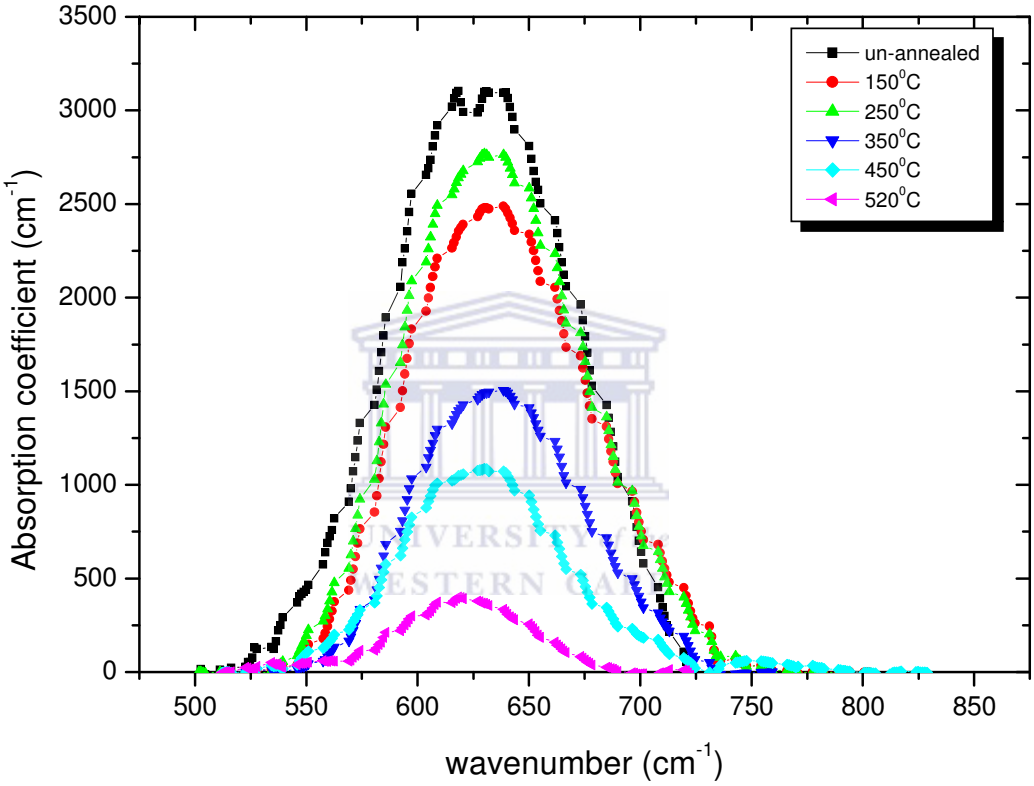

Figure 4.7 Bonded hydrogen curves at increasing annealing temperature.

As can be seen in figure 4.7, the hydrogen absorption in the films is shown to be decreasing with increasing annealing temperature (thirty minutes annealing time), as expected. There is however an anomaly for the sample annealed at 250°C. The concentration of bonded hydrogen is higher than for the film annealed at 150°C, which is a curious finding. This could be due to hydrogen adsorption from the water vapour present in the nitrogen ambient, which overshadows removal of bonded hydrogen from

the film. An inherent flaw in such an explanation is that the 150°C anneal would have produced similar results as the nitrogen ambient used was from a similar source for all the annealing experiments in this series. An alternative interpretation could be that from the crystallinity results discussed earlier, due to the higher film crystallinity in the whole film compared to the other films in the series, more crystallite surfaces exist in this film that scavenge hydrogen, leading to an increase in total hydrogen bonding. This seems like a more credible explanation. For the rest of the annealing series hydrogen content decreases until at 520°C minimal bonded hydrogen remains. The longer anneal at the same temperature yielded an unusable FTIR spectrum, suggesting that no more bonded hydrogen remained in the silicon. As the integrated intensity of the 640 cm^{-1} mode is a measure of the total bonded hydrogen in the silicon [4.15]; we now show in figure 4.8 the dependence of the refractive index at long wavelengths, on the integrated intensity or amount of bonded hydrogen. The un-annealed film has a n_0 value of 3.30. The n_0 value represents a measure of the optical density of the film, and it is evident that the film density increases as bonded hydrogen is decreased. The trend-breaking point in the right bottom of the graph is from the annealing temperature of 250^0C, discussed earlier.

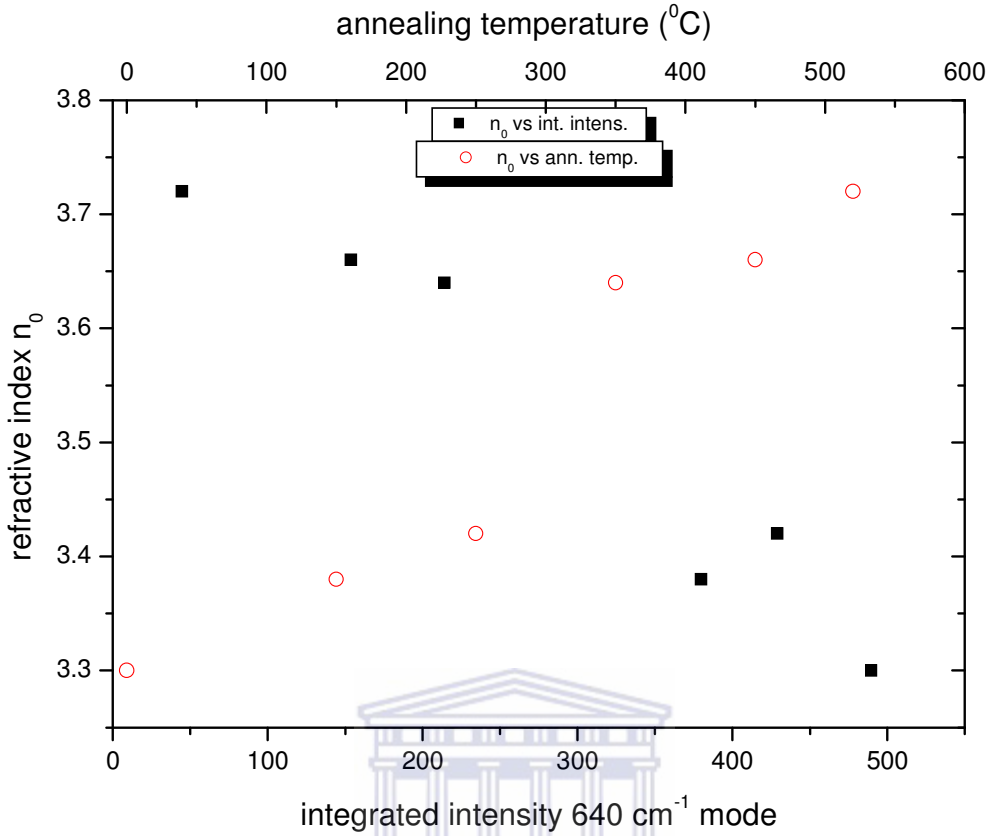

Figure 4.8 Refractive index at long wavelengths vs integrated intensity at 640 cm^{-1} mode.

The optical gap, as an important optical parameter, is influenced by a few factors. Traditionally, for a-Si:H a certain dependence of the optical band gap on the hydrogen content of the films exist, updated in reference [4.16]. The role of the hydrogen is not only just to passivate the dangling bonds, but also to reduce the magnitude of the silicon bond angle variation. In addition the hydrogen serves to reduce the internal stress in the amorphous network [4.15]. The hydrogen thus allows for a more 'ideal' structure. Another factor influencing the band gap is the strength of the bonds in the amorphous network [4.17].

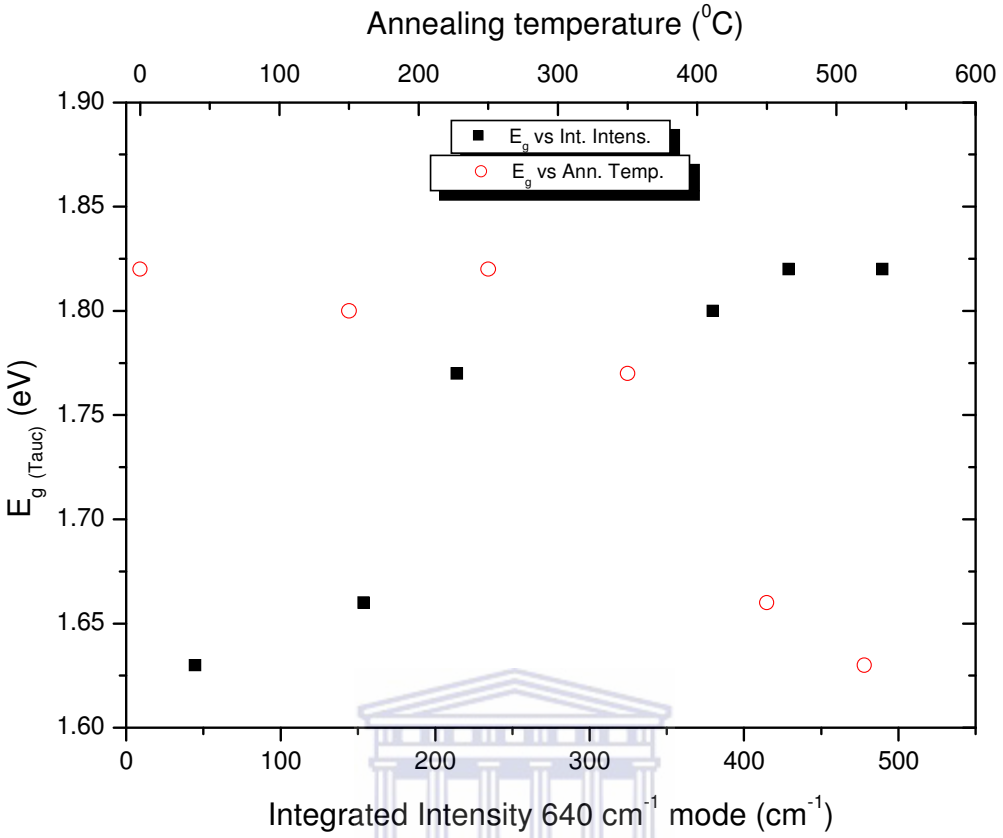

Figure 4.9 Tauc band gap vs integrated absorption at the 640 cm^{-1} mode.

A higher band gap signifies stronger bonds in the network of atoms. Hydrogen alloying of pure a-Si therefore serves to increase the band gap, since the stronger Si-H bonds replace the weaker Si-Si bonds. The other factor influencing the band gap in a-Si:H is the order of the amorphous network; a highly strained network has a lower band gap than a relaxed one, although bonding configurations may be similar. The band gap versus the integrated absorption for the annealing series is shown in figure 4.9. The trend for the annealed protocrystalline silicon is still conforming to that of a-Si:H [4.16]. At this stage it could still be surmised that the lower band gap values at low hydrogen content, alternatively higher annealing temperature, can be attributed to the small changes in structural order; these changes are very small compared to those for non-protocrystalline

a-Si;H. It is also informative to investigate the hydrogen bonding configurations. The 845 cm^{-1} mode for a-Si:H is normally attributed to $(=Si=H_2)_n$ for n≥2, and the 880 cm^{-1} mode to $(=Si=H_2)$, both being bending modes [4.15]. At 890 cm^{-1} the bending mode for $(=Si=H_2)_n$ for n≥2 can be found. Figure 4.10 illustrates the hydrogen bonding configurations at the 800 – 900 cm^{-1} vibrational modes.

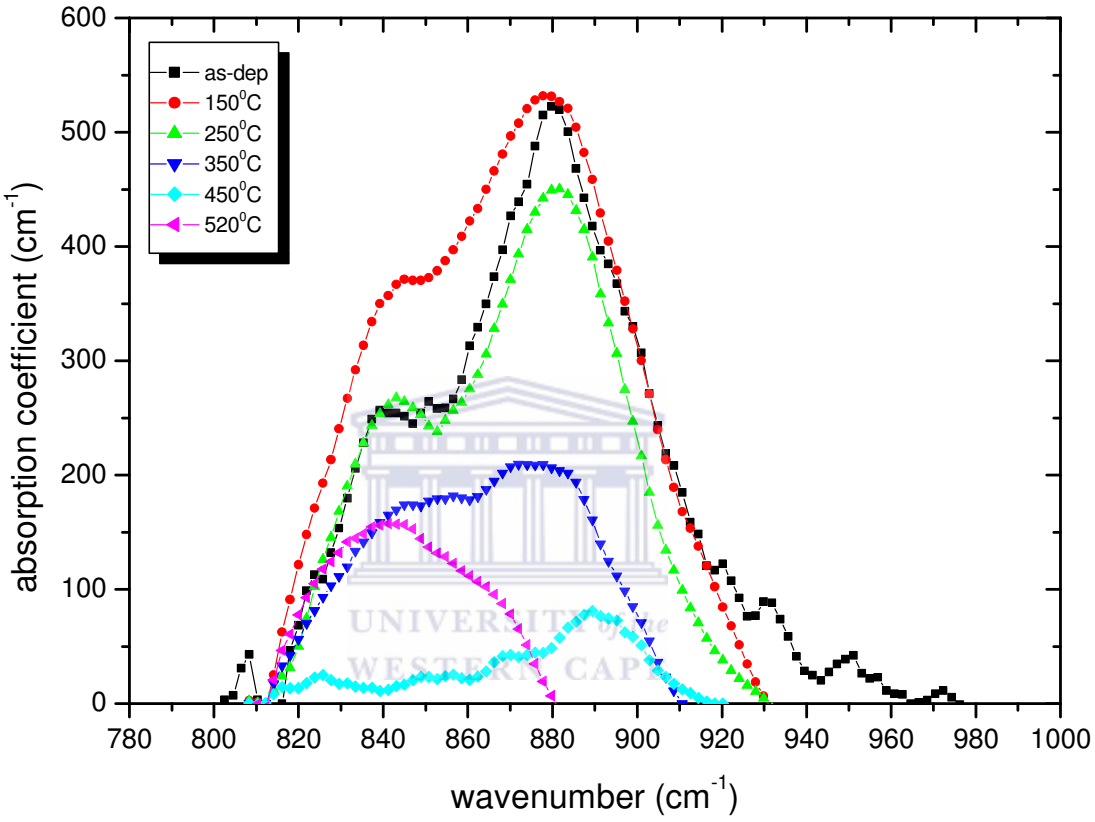

Figure 4.10 Hydrogen bonding configurations evident at the 800 – 900 cm^{-1} modes.

For our series, if the materials are considered as classical a-Si:H, then in general most of the hydrogen bonded in the $(=Si=H_2)$ phase disappears with increasing annealing temperature, until only the 845 cm^{-1} mode containing $(=Si=H_2)_n$ remains at 520°C. Moreover, identifying changes in this bonding configuration, when the material is subjected to the range of annealing temperatures, is not instructive in clarifying the nanocrystalline nature of the material. We therefore need to scrutinize the other

vibrational modes, specifically the stretching modes at 2000 – 2100 cm^{-1}. This is shown in figure 4.11.

For the un-annealed sample preferential monohydride bonding is observed, as the $R^* = \frac{I_{2100}}{I_{2100}+I_{2000}}$ for a-Si:H value of ~0.27 attests; the R* was calculated using the formula for a-Si:H and not the one used in nanocrystalline silicon studies. The sample at 250°C again displays an inconsistency with the general trend in that clustered hydrogen bonding seems to be preferred. A shift towards monohydride bonding then occurs for the next sample in the annealing series, indicative of the removal of hydrogen from the clustered phase while the remaining hydrogen is bonded in the more stable monohydride configuration. At 450°C a split in the 2000 and 2100 cm^{-1} modes starts to emerge and is very evident at 520°C. Normally this would be illustrative of Si-H bonds on voids formed in addition to the isolated Si-H bonds, or to crystals present in the more crystalline silicon material [4.18 – 4.19].

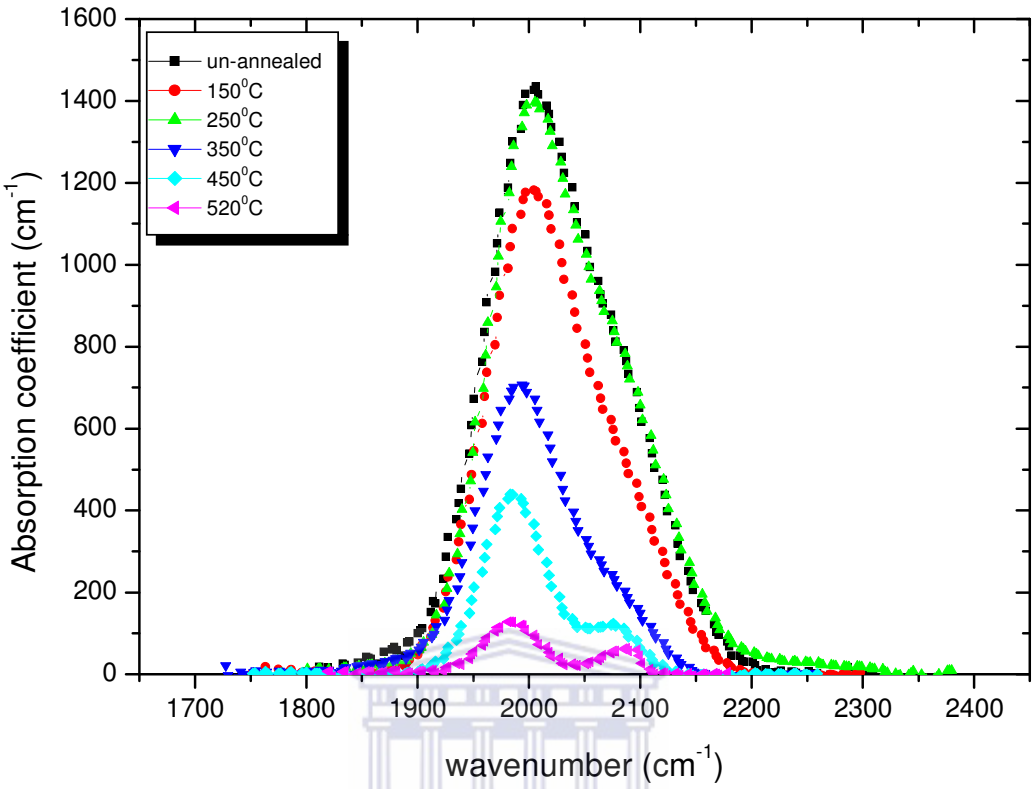

Figure 4.11 Hydrogen bonding configurations at 2000-2100 cm^{-1} mode at increasing annealing temperature.

Mahan et.al. [4.20] have described very ordered hydrogenated amorphous silicon deposited by HWCVD extensively. The films in their study exhibited primarily monohydride bonding, that is the 2000 cm^{-1} signal dominated the band at 2000 – 2100 cm^{-1}. Some of their findings were as follows: although the peak position of the stretch mode of the low bonded hydrogen content (C_H) HWCVD a-Si:H is similar to that observed in other types of low C_H a-Si:H, the shape of the peak changes dramatically by becoming more intense compared to the wag mode and at the same time much narrower. This was seen in the context of improved ordering in the lattice for films containing low C_H. For higher C_H = 11.0 at. % , but well-ordered HWCVD a-Si:H films the Si-H stretch and wag modes at 2000 and 640 cm^{-1} were the predominant features with a hint of the scissors-bending mode at 860 – 880 cm^{-1}, the isolated dihydrides. The stretch/wag ratios

of peak heights and peak areas of these higher C_H films were 0.53 and 0.17, respectively with the FWHM of the stretch mode ~ 90 cm^{-1}. However, for 1.7 at. % C_H, the difference was striking, a stretch/wag height ratio of 0.91 and stretch mode FWHM of 62 cm^{-1} was observed, which constitutes considerable narrowing. It was suggested that the narrowing of the stretch mode is an intrinsic property of low C_H a-Si:H films in general, inclusive of low C_H as-deposited or annealed films. A value of ~ 60 cm^{-1} was prescribed as universal for all low C_H films, independent of the method used to obtain the low hydrogen concentration.

We made use of Mahan et.al.'s terminology to include a table of our values in table 4.1. The FTIR data for the set of films that were annealed at the different temperatures are shown to illustrate the 'order' parameters.

Annealing temperature (°C)	**Peak frequency wag mode (cm^{-1})**	**Peak frequency stretch mode (cm^{-1})**	**FWHM Si-H mode (cm^{-1})**	**Stretch/wag height ratio**	**Stretch/wag intensity ratio**	**R***
Un-annealed	627.1	2002.1	103.2	0.39014	0.14951	0.2691
150	639.8	1998.8	90.9	0.42409	0.14471	0.27359
250	637.0	1994.2	71.3	0.25022	0.06503	0.71385
350	637.7	1995.7	100.4	0.40657	0.16671	0.09826
450	629.6	1986.5	70.4	0.37674	0.10442	0.1635
520	619.2	1984.9	61.2	0.31608	0.09195	0.21714

Table 4.1 FTIR parameters of vibrational modes for annealing series.

From the data in the table the frequency shift to ~ 620 cm^{-1} of the wag mode for the film at 520°C is ascribed to the presence of crystallites contained within the amorphous matrix [4.3], with the large majority of the H bonded on these crystallite surfaces. Further, from the un-annealed state to the anneal at 520°C, the stretch mode shift to 1985 cm^{-1} is also seen as indicative of increased ordering with increasing annealing temperature. This observation is made despite values of the stretch/wag height and intensity ratios not increasing dramatically as in the referenced work.

The interpretation of these stretch modes presents the uncertainty whether the modes should rather be interpreted as hydrogen as it would be bonded in a nanocrystalline silicon film. The FTIR absorption spectrum of a nanocrystalline silicon sample would exhibit absorption bands in the region 1900–2150 cm^{-1} as the result of a combination of several absorption bands associated with the stretching vibrations of $Si–H_x$ in different configurations. It can be decomposed into three Gaussian components. The absorption peaks centred around 1985 cm^{-1} and 2090 cm^{-1} are assigned to the stretching vibrations of Si–H monohydrides in the amorphous network (isolated) and on the surface of the Si nano-crystallites (clustered), respectively, [4.21 – 4.22]. These two vibrational modes appear in all the absorption spectra in our series, as they would also in ordered or disordered hydrogenated amorphous silicon. The weak absorption band centred at 2130 cm^{-1} is assigned to the existence of $(=Si=H_2)_n$ polyhydride complexes on Si nanocrystallite grain boundaries [4.19, 4.23]. Deconvolution of the stretching modes could not suffice to significantly quantify the 2130 cm^{-1} mode, especially for the 150°C anneal, which presumes the existence of detectable crystallites by Raman spectroscopy. This mode is also absent from all the other spectra, especially the absorption spectrum of the material at 520°C annealing temperature, but is found at the 845 cm^{-1} mode. We therefore interpret the hydrogen bonding configurations as one would normally do for classical a-Si:H.

The discussion so far leads to an interpretation of the material before and after the annealing that are similar to the a-Si:H films of Mahan et.al. deposited at elevated temperatures without hydrogen dilution [4.2]. Increased clustering leads to large spatial

regions that contain minimal bonded hydrogen. This leads to an improved structuring of the network as the bonded hydrogen content is lowered. The improved structuring occurs on a length scale of 5 – 30 Å. These hydrogen deficient regions become an even larger fraction of sample volume with declining bonded hydrogen content, leading to improved lattice ordering. The split in the absorption modes 2000 – 2100 cm^{-1} indicate some form of crystallinity, undetectable by conventional means due to the extremely small, angstrom sized protocrystallites, which should also influence the optical properties of the films. At the 6 hour anneal no bonded hydrogen could be detected, but yet no specific Raman crystalline Si signature could be detected either, probably also due to the small crystallite sizes.

This leads to the expectation that this specific sample should be different in optical properties and defect densities, due to the lack of passivating hydrogen for the dangling bonds. The absorption coefficient spectra are thus shown in figure 4.12.

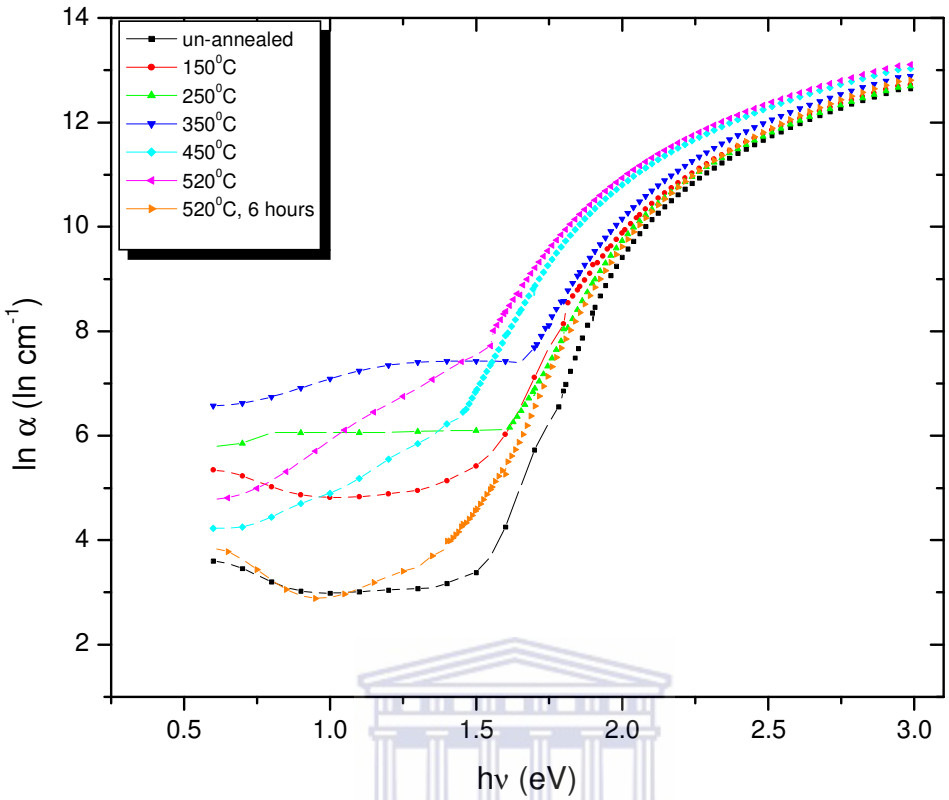

Figure 4.12 Absorption coefficient spectra of the films in the annealing series.

In the high energy region there is not much difference in the absorption curves for the un-annealed sample and up to the 350°C anneal. However, a gradual increase can be seen; a significant increase occurs up to the 520°C anneal, and then for the longer anneal at 6 hours the whole absorption spectrum resembles the un-annealed state excepting the sub-band gap absorption. For the preceding anneals the series show increased absorption in the sub bandgap states with increasing annealing temperatures, until recovery occurs to the un-annealed state at higher annealing temperatures. Although similarities in shapes and magnitudes exist for the un-annealed and annealed state at 520°C for an annealing state of six hours, there is a noticeable difference in film quality which will affect its suitability for photovoltaic device application as intrinsic layer. We therefore need to evaluate its electronic qualities for device application.

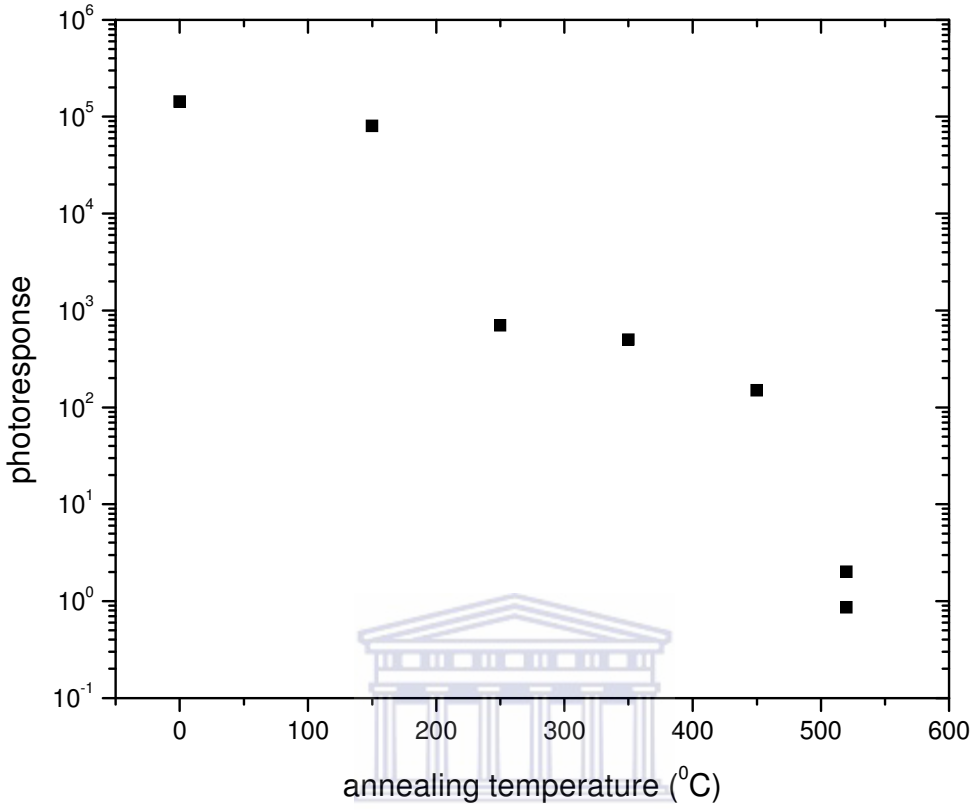

Figure 4.13 Photoresponse of annealing series.

Figure 4.13 illustrates the photoresponse dropping over several orders of magnitude from 10^5 to ~1 for the final anneal respectively, showing that annealing protocrystalline silicon degrades the electronic properties.

This could be attributed to an increase in defect densities with increasing annealing temperature, as is evidenced from the trends in the Urbach energy and defect density parameter [4.24 – 4.26] in figure 4.14. The density of defect states in a-Si:H can be directly correlated to the sub band gap absorption coefficient at a photon energy of 1.2 eV. The dangling bond defect concentration gives an indication of the defect states that

are located around the centre of the band gap where they act as efficient recombination centres, thereby reducing solar cell efficiency.

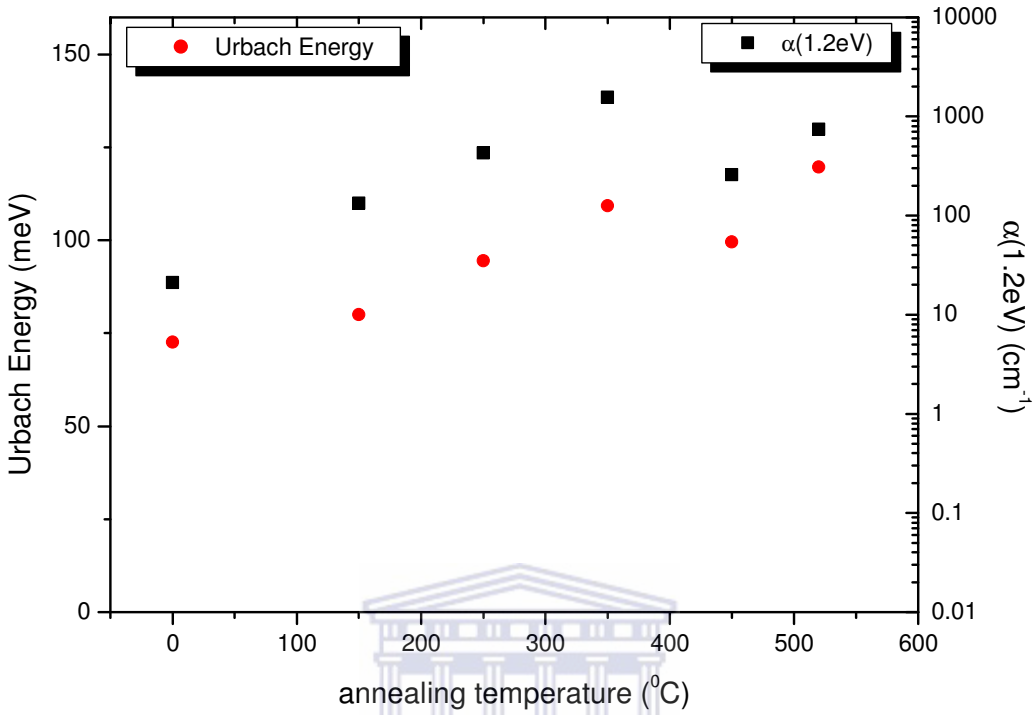

Figure 4.14 Urbach energy and defect density parameter of annealing series.

It is also enlightening to investigate the dependence of the electronic properties on the hydrogen content as shown in figure 4.15 where the photoresponse is plotted against the integrated intensity at the 640 cm^{-1} mode, whereas the photoresponse was plotted against the annealing temperature in figure 4.13. The degradation in electronic properties could be attributed to the creation of unterminated Si dangling bonds that contribute to the enhancement of defect states.

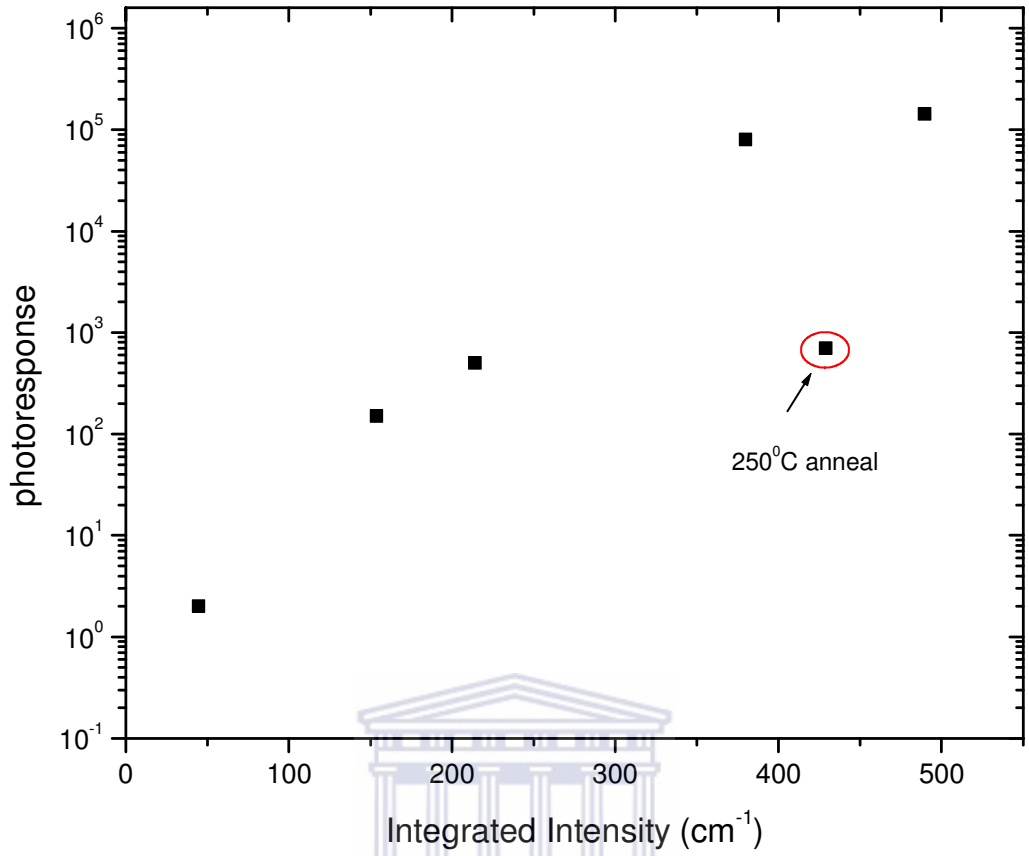

Figure 4.15 Photoresponse vs integrated intensity of 640 cm^{-1} mode.

The general trend of the photoresponse is broken by the one point in the graph pertaining to the 250°C anneal. This trendbreaking behaviour of the specific annealing temperature has been encountered before in absorption coefficient, film crystallinity from optical measurements, optical density, hydrogen content and FTIR parameters for the vibrational modes. The sample annealed at 250°C clearly has different film qualities. It appears that at this annealing temperature the film assumes an apparent crystalline nature which cannot be verified by fast detection methods such as XRD and Raman spectroscopy, yet the optical model constructed is sensitive enough to provide a more comprehensive picture.

In summary, Mahan *et al.* [4.27] found that in general for a-Si:H there is an increase in material band gap with H_2 dilution for as-deposited films. Literature also links the film band gap to the hydrogen concentration in the film; there is an approximately linear increase of the band gap for a-Si:H deposited by a wide variety of techniques. The band gap was also affected in that it increases when film order improves. For HWCVD a-Si:H improved short-range structural order widens the band gap. On the other hand a longer-range type of order (medium range order) examined by E_{04} data, the energy where the absorption coefficient is 10^4 cm^{-1}, yielded a medium range order (MRO) optical band gap parameter due to MRO only, with the effect of hydrogen alloying removed. The E_{04} MRO parameter increased with increasing order, suggesting that previous measurements in literature relating band gap to bonded hydrogen concentration C_H, the so-called alloying term, should be treated with some caution, especially the low C_H films where the alloying term could be over estimated. We therefore postulate that the contribution of the MRO band gap also influences our band values in this manner.

Further, small angle x-ray scattering on as-deposited HWCVD films [4.28] have shown elongated voids at densities highly correlated with growth rate. During the annealing process the bulk character of the a-Si:H matrix determines the SPC rate. Accompanying geometric changes of the voids with SPC annealing is a decrease in void fraction in the Si matrix. The largest change in void fraction occurs during the crystallization anneal, following the hydrogen effusion. If it is taken into consideration that in HWCVD films hydrogen incorporation during growth is distributed with roughly 90% of the H grouped in at least 14 atom clusters in 10% of the volume, then the rest of the H is sparsely distributed, leaving large volumes hydrogen-free. During annealing, hydrogen in the a-Si:H films forms high pressure bubbles of H_2 gas and this may drive the void structure formed during annealing. In the initial stages of SPC annealing, isolated hydrogen in the matrix of HWCVD samples either effuses out of the film or diffuses through the Si matrix to form bubbles at the H cluster sites. Coalescence of bubbles that are in close proximity also decreases the void fraction throughout the Si matrix. Stable H_2 forms in the bubbles and upon further annealing would increase the pressure in the bubbles, changing the shape of the bubbles. Finally H_2 begins to effuse from the bubbles until only

voids are left. In our series, it was evident from the data in figure 4.7 that the amount of bonded hydrogen at the annealing temperature of 250°C was larger than in the case of the anneal at 150°C. The amount of bonded hydrogen then decreased significantly for the higher annealing temperatures. We postulate that the hydrogen atoms are too strongly held by the Si atoms during the annealing process at 250°C, and they are not available for the formation of the high pressure H_2 bubbles as yet. The decrease in bonded hydrogen content for the higher annealing temperatures suggests that the H atoms can become available for bubble formation for the higher annealing temperatures when removed from the Si bonding sites.

4.4 CONCLUSION

The annealing series has been investigated in terms of the material disorder, hydrogen concentration and optical properties, all which play a role in the stability of the material.

The trend in n_0 for our series and the stable void volume fraction estimated from the optical modeling seems to confirm that the material gets compact upon increasing annealing temperature. The un-annealed film in our series was already in a very ordered state, as suggested by the SRO parameter from Raman scattering. Annealing the material does not make it revert to a more disordered state such as poor-quality a-Si:H with high disorder value Γ. In fact a small crystalline signature was observed from Raman scattering at the lowest annealing temperature, indicating that crystallites grew large enough to be detected. At higher annealing temperatures these suspected crystallites were too small for detection by Raman spectrosocopy; on the other hand the very ordered nature of these films were confirmed by the optical modeling of the dielectric function of polycrystalline silicon in an amorphous matrix. It showed that surface crystallinity could be substantial for the higher temperature anneals, specifically at 250°C the whole film was found to be more ordered, which affected its optical and electronic properties significantly compared to the other films. It was found that the ambiguities around the detection of the small crystallites are significant enough not to warrant a description of the annealed material as nanocrystalline. These films behave rather as if they are more in

accordance with Mahan *et al.*'s films that are ordered, but have hydrogen deficient regions. Similarities of the annealed states in this study with that of the referenced materials are achieved at high annealing temperatures in terms of low bonded hydrogen content, but we experience a lowering of material quality.

Our un-annealed or deposited material already has superior qualities, but annealing the films degrades the material quality. It was established that hydrogen remains in the film until a long annealing time at relatively high temperature removes all the bonded hydrogen from the film. Finally, the thermal budget in terms of annealing temperature and annealing time is clearly not sufficient to break the strong bonds and crystallize the material. The question now remains whether metallization and subsequent annealing will have a different influence on the bonded hydrogen and crystallization aspects of the film. This will be addressed in the next chapter.

REFERENCES

4.1 S. Guha, Sol. En. 77, (2004) 887

4.2 A. H. Mahan, D. L. Williamson and T. E. Furtak, Mater. Res. Soc. Symp. Proc. 467, (1997) 657

4.3 A. H. Mahan, J. Yang, S. Guha, D. L. Williamson, Mater. Res. Soc. Symp. Proc. 557, (1999) 269

4.4 D. L. Williamson, Mater. Res. Soc. Symp. Proc. 557, (1999) 251

4.5 W. Du, X. Liao, X. Cao, X. Yang, X. Deng, K. Sun, J. Non-Cryst. Sol. 354, (2008) 2155

4.6 R. A. Street, K. Winer, Phys. Rev. B 40, (1989) 6236

4.7 A. J. M. Berntsen, Ph.D. Thesis, University of Utrecht, Utrecht, The Netherlands (1993)

4.8 K. F. Feenstra, R. E. I. Schropp, W. F. Van der Weg, J. Appl. Phys. 85, (1999) 6843

4.9 K. H. M. Maessen, M. J. M. Pruppers, J. Bezemer, F. H. P. M. Habraken, W. F. van der Weg, Mater. Res. Symp. Proc. 95, (1987) 201

4.10 H. Meiling, M. J. van den Boogaard, R. E. I. Schropp, J. Bezemer, W. F. van der Weg, Mater. Res. Symp. Proc. 192, (1990) 645

4.11 N. Maley, J. S. Lannin, Phys. Rev. B 36, (1987) 1146

4.12 Karine van der Werff, Utrecht University, private communication

4.13 P. A. Temple and C. E, Hathaway, Phys. Rev. B 7, (1973) 3685

4.14 D. Beeman, R. Tsu and M. F. Thorpe, Phys. Rev. B 32, (1985) 874

4.15 R. A. Street, in 'Hydrogenated Amorphous Silicon', Cambridge Solid State Series, Cambridge (1991)

4.16 Marieke van Veen, PhD Thesis, Utrecht University, the Netherlands (2003)

4.17 D. Weaire and M. F. Thorpe, Phys. Rev. B 4 (8), (1971) 2508

4.18 D. Stryahilev, F. Diehl, B. Schroder, M. Scheib, A. I. Belogorokhor, Phil. Mag. B 80 (10), (2000) 1799

4.19 D. Stryahilev, F. Diehl, B. Schroder, J. Non-Cryst. Sol. 266-269, (2000) 166

4.20 A. H. Mahan, L. M. Gedvilas, J. D. Webb, J. Appl. Phys. 82 (4), (2000) 1650

4.21 D. Han, K. Wang, J.M. Owens, J. Appl. Phys. 93, (2003) 3776

4.22 J.K. Rath, H. Meiling, R.E.I. Schropp, Jpn. J. Appl. Phys. 36, (1997) 5436

4.23 C. Gonalves, S. Charvet, A. Zeinert, M. Clin, K. Zellama, Thin Solid Films 403–404, (2002) 91

4.24 M. Vaněček, A. Poruba, Z. Remeš, J. Rosa, S. Kamba, V. Vorlíček, J. Meier, A. Shah, J. Non-Cryst. Sol. 266 – 269, (2000) 519

4.25 G. van Elzakker, V. Nadazsdy, F. D. Tichelaar, J. W. Metselaar, M. Zeman, Thin Solid Films 511 – 512, (2006) 252

4.26 J. Melskens, G. van Elzakker, Y. Li, M. Zeman, Thin Solid Films 516, (2008) 6877

4.27 A. H. Mahan, R. Biswas, L. M. Gedvilas, D. L. Williamson, B. C. Pan, J. Appl. Phys. 96 (7), (2004) 3818

4.28 D. L. Young, P. Stradins, Y. Xu, L. M. Gedvilas, E. Iwaniczko, Y. Yan, H. M. Branz, Q. Wang, Appl. Phys. Lett. 90, (2007) 081923

CHAPTER 5

Optical properties of Metal Induced crystallized silicon

5.1 INTRODUCTION

In the past, long processing times and temperatures above 600°C were the norm for solid phase crystallization (SPC) of amorphous silicon (a-Si). A modification of the method uses metals as the catalysts for crystallization; resulting in a reduction of the crystallization temperature and processing time [5.1]. The process is now known as the metal induced crystallization (MIC) of silicon, which has been implemented successfully for a-Si or hydrogenated amorphous silicon (a-Si:H) grown by various deposition techniques, using both eutectic and compound-forming metals [5.2]. The proposed MIC mechanism so far interprets the reduction in processing temperature and processing time as being caused by the change in bonding type, from strongly covalent Si-Si to metallic [5.3]. This is due to the interaction of free electrons from the metal with the covalent bonds near the metal/Si interface, which reduces the elevated activation energy and thus the high crystallization temperature. The efficacy of the method was also demonstrated on other semiconductors, notably amorphous germanium [5.4 – 5.5] and amorphous silicon carbides [5.6]. It is thus expected that the MIC process will continue to play an important role in the manufacture of thin film devices.

Recently it has also been found to be of use for photovoltaic device application [5.7]. As such it is important to understand the optical properties of MIC Si, for use in photovoltaic

device incorporation, even though most studies on such material do not particularly focus on the extraction of optical functions.

In this study aluminum and nickel as eutectic and non-eutectic metals, respectively, were used as catalyzing agents in a series of experiments designed to investigate the optical properties of MIC silicon. Furthermore, the effect of silicon-hydrogen bonding configuration was studied by FTIR spectroscopy and the crystallinity investigated by Raman spectroscopy and X-Ray Diffraction. The unusual, atypical reflection (R) and transmission (T) spectra were analyzed by the construction of an optical model with the Scout® commercial software [5.8] for interpretation of the resulting absorption coefficient in above-bandgap regions of the energy range. The photothermal deflection spectroscopy (PDS) method gave information on sub-bandgap absorption of the new MIC material, which has hitherto not been much reported on.

5.2 EXPERIMENTAL DETAILS

In this section the hydrogenated amorphous silicon used were from the same batch of protocrystalline silicon as described in the previous chapter. The sample pieces were metalized by depositing the metal layers on top of the a-Si:H in a thermal evaporation chamber in which the base pressure was kept at 10^{-6} mbar, at Utrecht University. The average metal thickness was 25 nm Al and 20 nm Ni, determined with a fitting procedure using the dielectric functions of metal and glass with the Scout® software. The thickness of metal is deemed to be sufficient for initiating and inducing crystallization [5.2].

Handling of the samples exposed the material to air during the different processes, and it is not ruled out that native oxide layers could have formed. The silicon oxide layer is thought to play a role in the layer exchange mechanism, that the silicon oxide becomes available for the creation of an aluminum oxide layer that in turn enhances layer exchange during crystallization. Therefore no HF dip was performed prior to metal deposition.

After cooling the samples were transferred to a conventional furnace where nitrogen was introduced upon annealing. Annealing times of 30 minutes were applied for a temperature series of 150, 250, 350, 450 and 520°C, while a separate anneal for six hours at 520°C was also performed. After the annealing and subsequent cooling, the remaining metal was removed chemically in a HCl bath and the samples were afterwards washed in de-ionized water. Figure 5.1 schematically depicts the procedure.

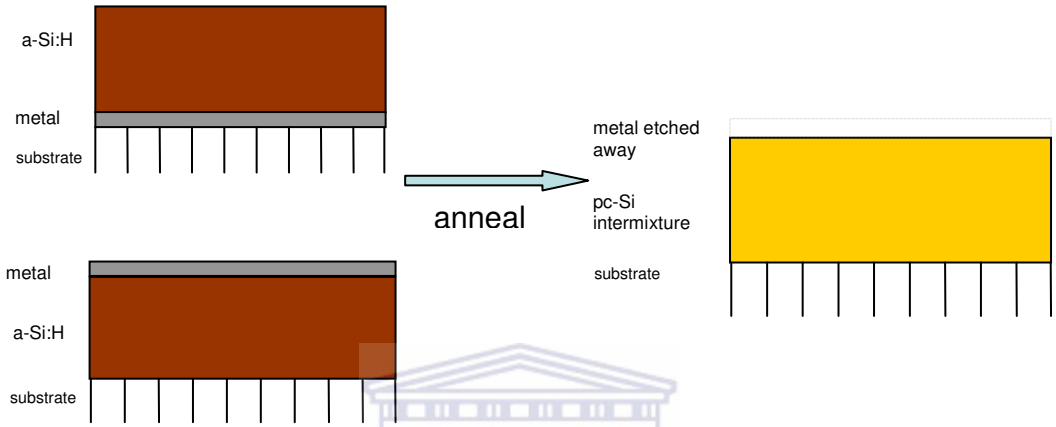

Figure 5.1 Two common configurations to manufacture MIC poly-Si.

Raman Spectroscopy, UV-VIS, PDS and FTIR characterization were performed as before at Utrecht University. XRD was performed with a Panalytical X-ray powder diffractometer operating at 45 kV and 40 mA in reflection geometry at 2θ-values ranging from 5 to 70° with a step size of 0.026°, using a Copper $K_{\alpha 1}$ radiation with a wavelength of 1.5406 Å as the X-ray source. The XRD measurements were performed at the CSIR National Centre for Nano-structured Material, Pretoria, South Africa.

5.3 RESULTS AND DISCUSSION

5.3.1 Role of hydrogen

To investigate the interaction of metals with hydrogenated amorphous silicon it is important to take cognisance of the presence of hydrogen in the silicon matrix. An effusion study of hydrogen from amorphous silicon in the metal induced crystallization process, using various metals was performed by Ohmi. *et al.* [5.11] that gives valuable information that can compliment the interpretation of the results of the annealing process. In their study the metal was also deposited on top of the silicon thin films, and the H_2 effusion was measured with temperature programmed desorption spectroscopy (TPD). For the reference sample of un-metallized a-Si:H the H_2 effusion started at a sample temperature of approximately 300°C, with the first effusion peak at around 350°C, the so-called low temperature (LT) peak, attributed to weak Si-H_n bonds in a void-rich matrix. The second peak, the so-called high temperature (HT) peak was detected around 550°C. This peak is related to strong Si-H_n bonds in a compact matrix. The activation energy for hydrogen effusion in the a-Si:H, Al/a-Si:H and Ni/a-Si:H systems were determined as 1.84 eV, 0.56 eV and 0.63 eV, respectively, which shows that hydrogen should effuse more readily from the Al/a-Si:H system.

In the case of aluminium in contact with a-Si:H the H_2 effusion was observed as low as 150°C annealing temperature, with the entire spectrum shifting to a lower temperature. The entire spectrum changed form from the reference a-Si:H, and we expect that most hydrogen depletion for our series should occur between ~ 350°C and 450°C. This strong effect of Al on H_2 effusion may be related to the diffusion of Al atoms into the a-Si:H film. The initial concentration of aluminium was found to also play an important role in decreasing the activation energy of H_2 effusion, therefore the amount of Al diffused into the a-Si:H film determines the catalytic effect. Moreover, the H_2 effusion temperature decreases with increasing thickness of Al such that for a 40 nm thick Al film a single peak was observed at 170°C. The proposed explanation is that the low temperature effusion is encouraged by weakening of Si-H bonds and the enhancement of diffusivity in

the alloyed material. The large shift in the HT peak may be due to the enhancement of H diffusivity in the alloyed material. It is known that some metals such as Ni form silicide phases with Si [5.2] and that hydrogen is released by Si-H bond breaking at relatively low temperatures. Research has shown that film crystallization at temperatures below 500°C is induced by NiSi which results in smaller grains compared to the film grains in which crystallization is induced by $NiSi_2$. Typically the larger grains are found in the temperature range 500°C to 600°C. For both these processes hours of annealing time is necessary [5.12]. For the Ni/a-Si:H system the LT hydrogen effusion peak already appeared at 150°C in the Ni/a-Si:H system, ascribed to a local catalytic reaction occurring in the metal-rich layer at the metal/a-Si:H interface. Two broad peaks at ~ 300°C and 500°C were also evident in the spectra. These temperature ranges in the Al/a-Si:H and Ni/a-Si:H gives us a good indication that most of the hydrogen should effuse in the range 300°C to 500°C for both Al/a-Si:H and Ni/a-Si:H systems.

We now investigate the hydrogen bonding configurations in our Al/a-SiH and Ni/a-Si:H during the AIC and NIC processes, respectively. The spectra appeared especially noisy in the AIC series, and we speculate that the presence of metal in the films could affect the transmission measurements due to diffuse reflections causing uncertainties in the intensities. Metal hydride formation which may alter the intensities is also not taken into account. The information will therefore not be expressed in terms of bonded hydrogen concentration C_H, which is normally used for hydrogenated amorphous or nanocrystalline silicon, but rather in terms of the integrated absorption at the different vibrational modes. The thickness was taken into account with the necessary BCC correction performed. However, the information obtained is still valuable in terms of the positions of the vibrational modes, and if we ignore the possible diffuse reflection effects we can proceed in an attempt to qualitatively interpret the FTIR spectra. In figure 5.2 we present the information on the 640 cm^{-1} mode for the annealing temperatures of interest. It should be noted that the FTIR spectra for the samples at 520°C annealed for 6 hours yielded no analytical information, suggesting that no bonded hydrogen remains at this stage. From figure 5.2 it can be seen that hydrogen is present in the material up to an annealing temperature of 520°C. For the AIC process the reduction in bonded hydrogen is enhanced

from 350°C to 450°C compared to the NIC process, which correlates very well with the lower activation energy for the Al/a-Si:H system.

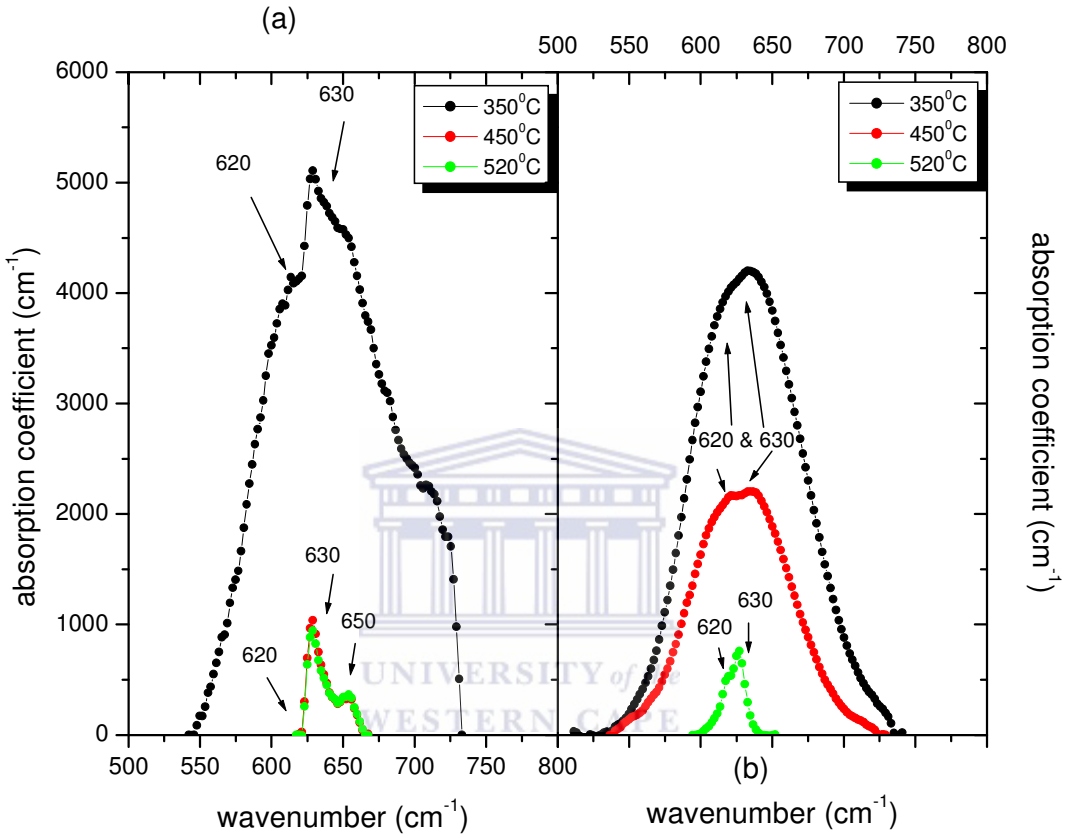

Figure 5.2 Bonding configuration of the (a) AIC and (b) NIC series at 640 cm^{-1}.

Stryahilev *et al.* [5.13] have performed a detailed FTIR study on hydrogenated microcrystalline silicon (µc-Si:H) and some of the features in the spectra above can be explained on the basis of their results, notwithstanding the fact that we had metal-silicon interactions in our systems. For the µc-Si:H they observed that the lower frequency S-H bending and Si-H_n wagging-rocking band is dominated by two sharp lines at 620 and 630 cm^{-1}, instead of a wide, well-known absorption band at 630-640 cm^{-1} for a-Si:H. For the

350°C AIC sample, these two features seem to be present, as well as a band at ~650 cm^{-1} that correlates with the 660 cm^{-1} mode in their spectra for μc-Si:H. This band should contain both monohydride and polyhydride related absorption. This sample should therefore at the least be microcrystalline in nature. These bands are not so clearly discerned in the equivalent temperature NIC sample, but the NIC sample at 450°C does start showing such minute features. At 450°C and 520°C these features can be clearly discerned for the AIC samples, while the NIC sample at 520°C features the 620 and 630 cm^{-1} lines with the 650 cm^{-1} band absent. We expect these samples to show clear signs of crystallinity, specifically SiH bonds on (111) planes [5.13] that represent the natural and shifted resonance for the SiH bending mode. We now investigate the 2000 – 2100 cm^{-1} modes as shown in figure 5.3.

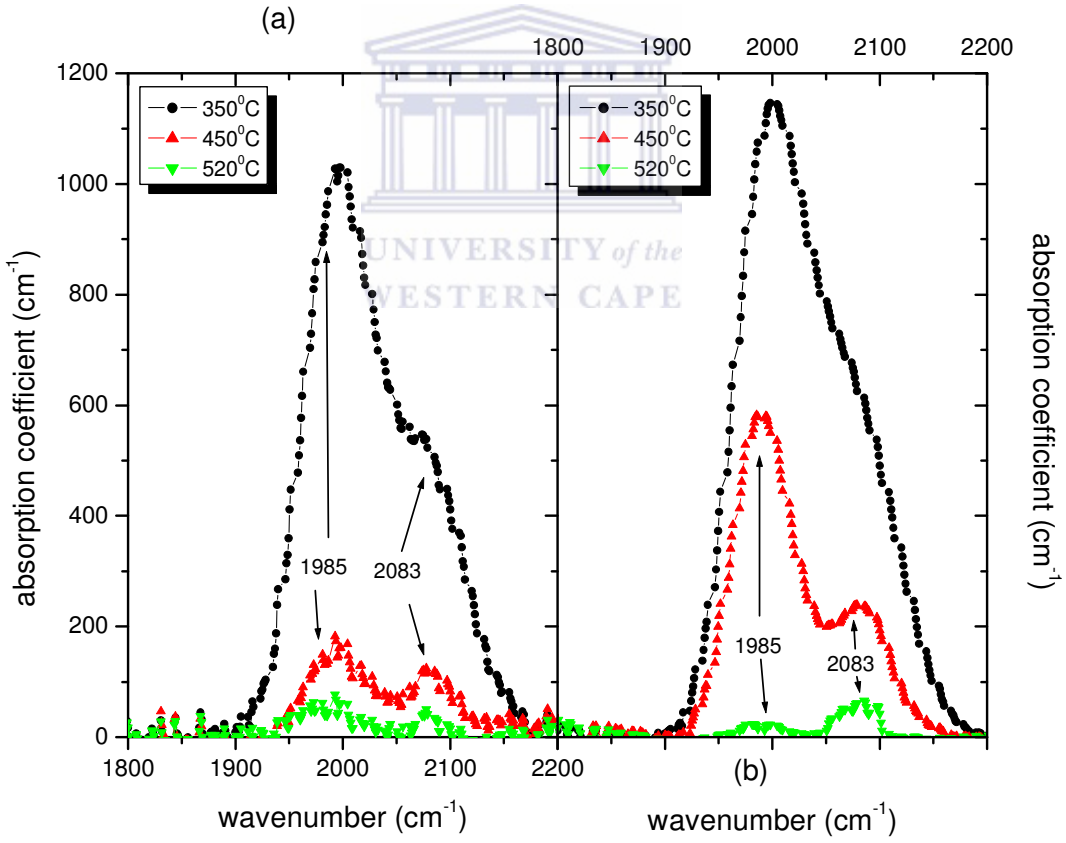

Figure 5.3 Bonding configuration of the (a) AIC and (b) NIC series at 2000-2100 cm^{-1}.

For the spectra where a clear split delineates the 1985 cm^{-1} from the 2083 cm^{-1} mode one can tentatively make the conclusion that they represent SiH stretching, natural resonance and shifted resonance on (111) planes respectively [5.13]. These are the AIC 450°C and 520°C samples and the 520°C NIC samples. Since the pure split in these vibrational modes is absent from the 450°C NIC sample we would rather not at this stage assign crystallinity, but rather confirm with structural measurements in the next discussion.

5.3.2 Structural characterization.

Figures 5.4 and 5.5 represent the Raman shift spectra of the AIC and NIC series respectively, taken from the film side in figure 5.4 and from the glass side in figure 5.5. The probing depth of the Raman beam is ~ 60 nm for amorphous silicon and is larger in the crystalline material [5.14]. For the AIC series the onset of partial crystallization is seen to occur at 350°C, as evidenced by the appearance of a slight hump for the vibrational mode at ~516 cm^{-1}. Assuming penetration of the laser beam from the glass side to probe ~ 120 nm into the interface between the glass and the silicon layer, we additionally interpret the Raman scattering measurement performed from the back of the sample. It is then evident that the film has not crystallized through to the glass-film interface, but at 450°C there is evidence of a slight contribution from crystalline material at the film/substrate interface. With higher annealing temperatures this mode is seen to shift towards 520 cm^{-1}, the TO mode of crystalline silicon such that for the AIC film at 520°C the material has crystallized after the 6 hour annealing time, throughout the film. For the NIC series the onset of crystallization only occurs at 520°C, the probe from the film side shows a very small contribution from the amorphous phase.

When the film is probed from the substrate side the well-defined peaks of c-Si can be seen, suggesting that crystallinity is preferentially induced from the substrate-interface side, as compared to the AIC films, where crystalline material could be found in the topmost part of the film, while the layer adjacent to the substrate could still remain amorphous. In contrast one can regard the film annealed for 6 hours to be crystalline

throughout. Thus the prediction from FTIR regarding film crystallinity was substantiated by Raman scattering measurements.

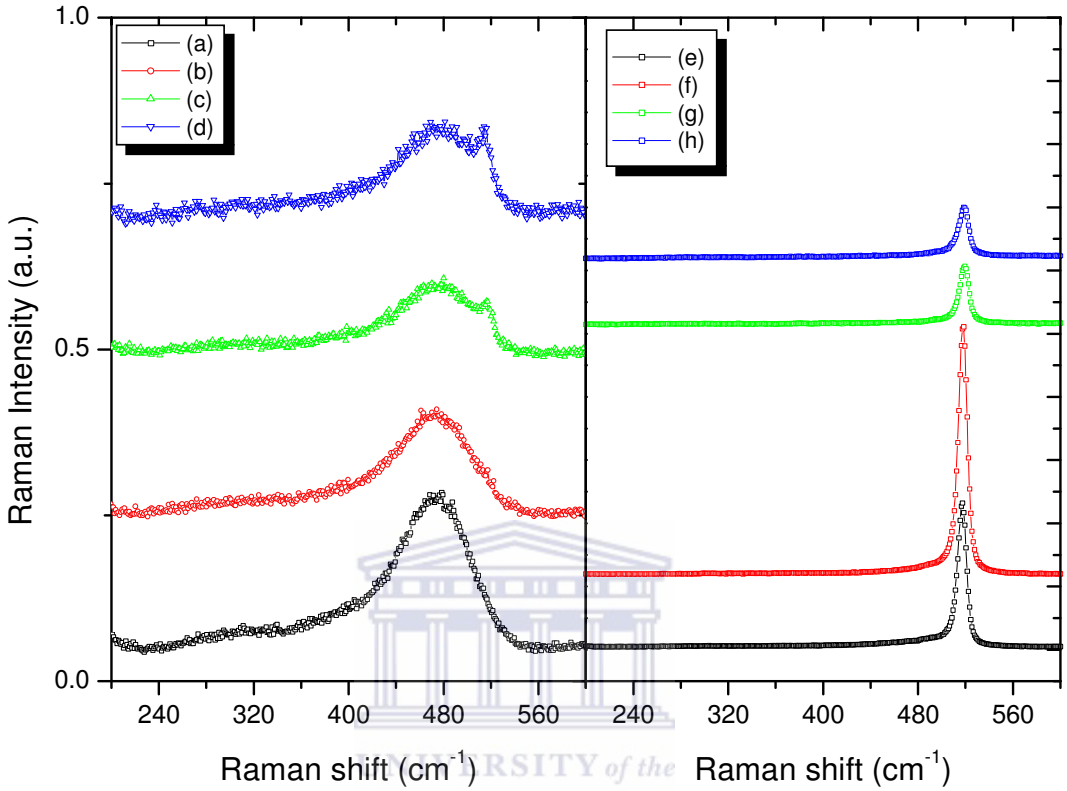

Figure 5.4 Raman shift spectra of (a) NIC 350°C, (b) NIC 450°C, (c) AIC 350°C and (d) AIC 450°C anneals. In the right hand figure the Raman shift of (e) NIC 520°C (f) NIC 520°C 6 hours (g) AIC 520°C (h) AIC 520°C 6 hours is shown. All the spectra were taken from the film side.

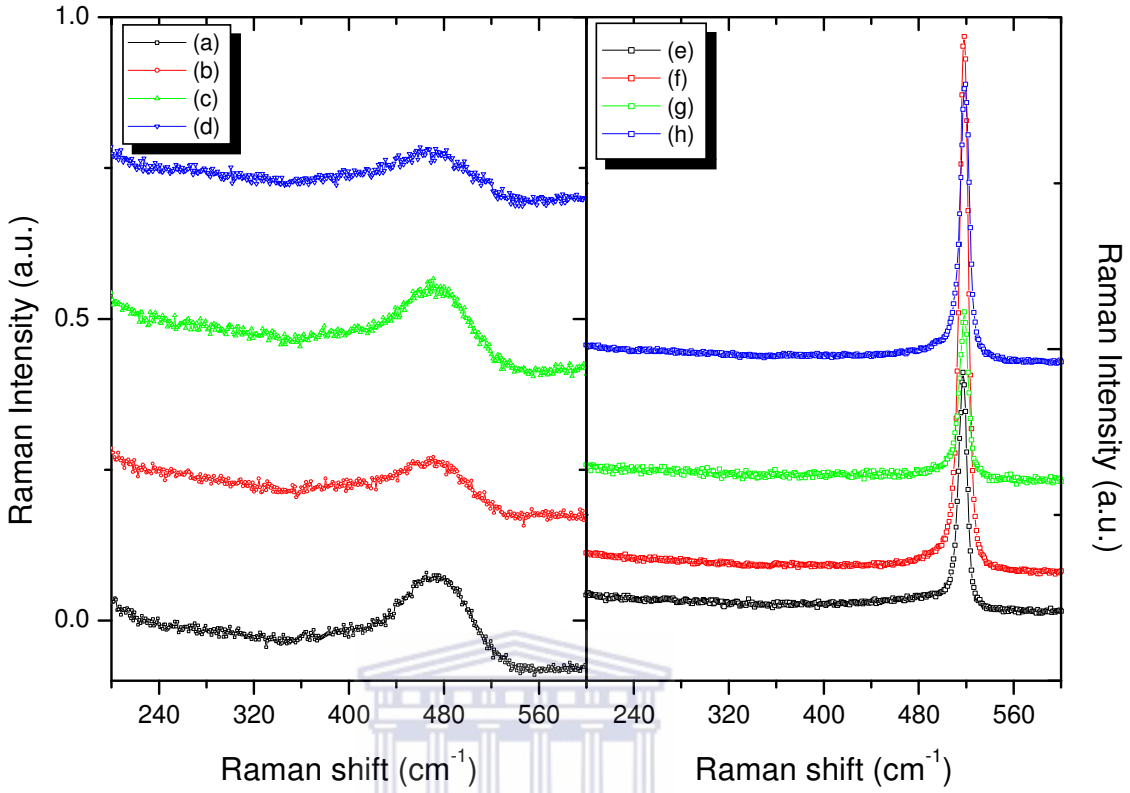

Figure 5.5 Raman shift spectra of (a) NIC 350°C, (b) NIC 450°C, (c) AIC 350°C and (d) AIC 450°C anneals. In the right hand figure the Raman shift of (e) NIC 520°C (f) NIC 520°C 6 hours (g) AIC 520°C (h) AIC 520°C 6 hours is shown. All the spectra were taken from the glass substrate side.

In figure 5.6 the XRD patterns for the AIC and NIC annealed films at 520°C show the characteristic peaks for silicon corresponding to the <111>, <220> and <311> orientations. It is evident that for the NIC film the peak intensity of the <220> orientation dominates that of the <111> orientation, while for the AIC film <111> appears to be the preferred orientation. In each case the Si (hkl) peak probably dominates because that orientation has the lowest free energy, presumably, caused by the fact that certain surfaces are energetically more favorable for growth [5.15]. Finally, for both films the crystal grain size calculated from Scherrer's formula [5.16] was 59 nm. Crystallite sizes

were estimated from reference [5.17] and amount to ~ 11.5 nm and ~ 7 nm for the AIC and NIC films, respectively.

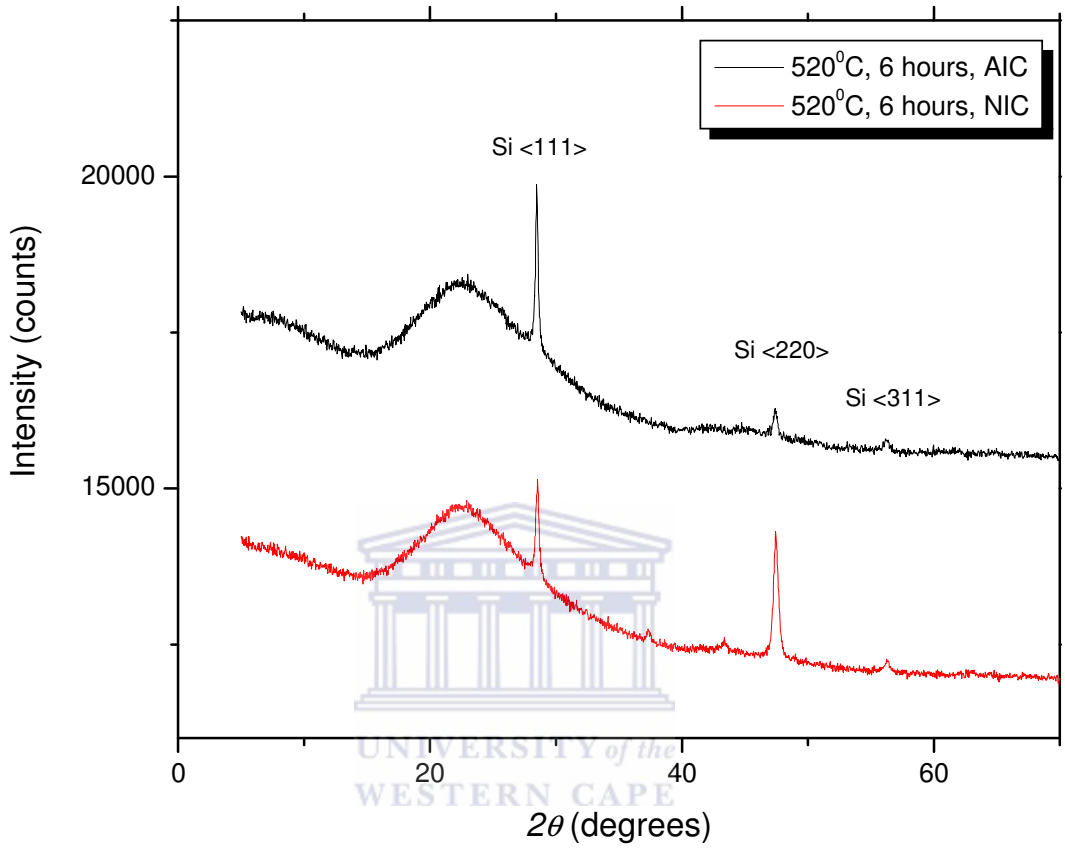

Figure 5.6 XRD spectra of AIC and NIC samples annealed at 520°C, for 6 hours.

5.3.3 The optical model

Spectroscopic ellipsometry was used in the past to describe the optical properties of crystallized silicon obtained by MIC [5.18]. However, the more readily available but yet powerful ultraviolet-visible spectrophotometer has not been extensively used to report on optical properties. This section presents the construction of a powerful model using existing software to analyse the UV-VIS spectra of MIC silicon.

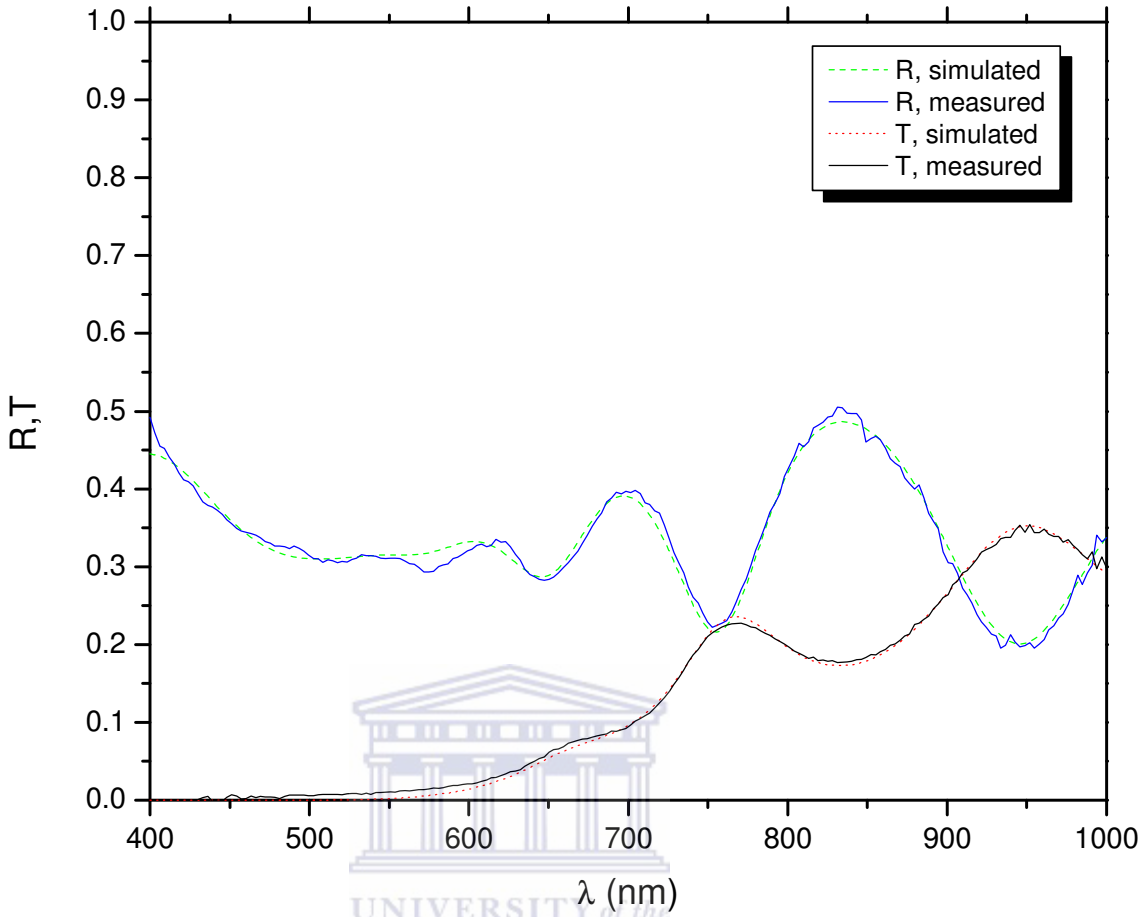

Figure 5.7 UV-VIS transmission and reflection spectra of crystallized a-SiH in the AIC series.

The UV-VIS transmission spectrum of an amorphous semiconductor thin film on glass is often used to calculate its properties with the Swanepoel method [5.19], which extracts information about the interference fringes to calculate the thickness and absorption coefficient. The fringes are normally well-defined whose intensities can be decreased if the film is not of homogenous thickness [5.20]. In all such cases interference maxima and minima can be reconstructed. These features are not discernible in the transmission spectra shown in figure 5.7. The transmission spectrum is shown together with the reflection spectrum. At these higher annealing temperatures a general suppression of

interference intensities occur compared with spectra of a-Si, such that the spectra become even more difficult to analyse. Figure 5.8 depicts the spectra for films where the onsets of crystallinity were observed, for the NIC series at 520°C. Besides the decrease in intensity for the interference fringes in both R and T spectra, we find also for the NIC film a paradoxical decrease in intensity for R in the lower wavelength region. At higher annealing temperature transmission extends into the normal strong absorption region (for a-Si) for the MIC films, which is confirmed by physical inspection to be much more transparent than a-Si films.

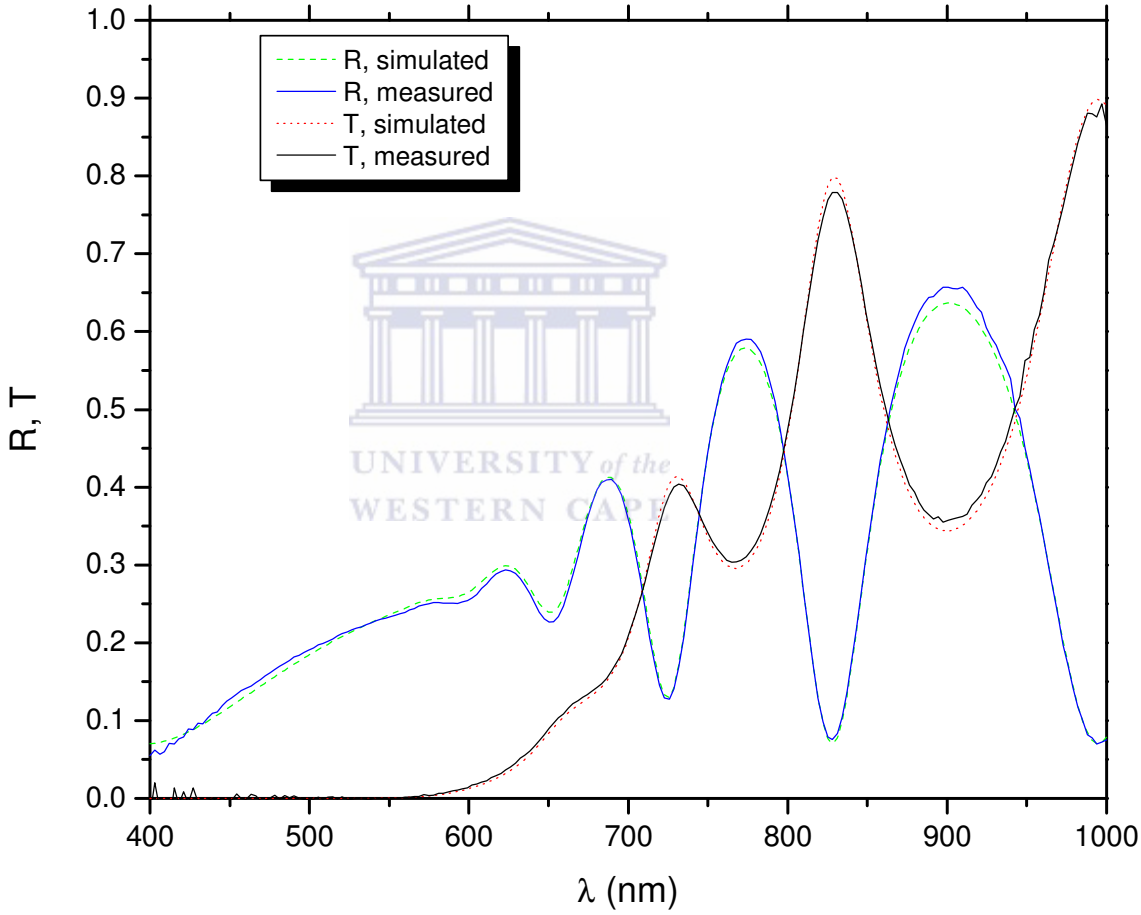

Figure 5.8 UV-VIS transmission and reflection spectra of crystallized a-SiH in the NIC series.

These effects place limitations on the manner in which the optical functions can be extracted. The effects could not merely be ascribed to variations in thickness in the probing area of the instrument beam on the sample, as the material was not homogeneous a-Si any more, after it underwent the treatment. It also implied that the Swanepoel method would not be appropriate to analyze such spectra, even though the method has been used to extract the optical functions of doped a-Si:H before [5.21 – 5.22] and even on doped poly-Si [5.23] prepared by a conventional deposition method. All the spectra in these studies looked typical, and no mention is made in an AIC study [5.24] of similar suppression of R and T spectra as is discussed here.

The difficulties that the spectra presented thus called for the construction of a realistic, workable model that takes into account metal impurities, void structures and silicon crystals. Adapting the layer structure, by including all the afore-mentioned to build a new master model in the Scout® software, allowed us to approximate the R and T spectra of the MIC material. Very good correlations of the simulations with the measured spectra were obtained, compared with previously discarded models during the course of this investigation.

We started off with a rough surface that was simulated by applying a mathematically defined function to allow for light scattering that occurs from the surface of the material, as advised in the software manual [5.8]. A viable microcrystalline silicon (μc-Si) of which the basic building block is the amorphous silicon matrix component was constructed using the built-in master a-Si model, based on the OJL interband transition model [5.25] which sets up parameters to describe an amorphous semiconductor thin film. Embedded in the a-Si matrix were porous regions which could be described by the inclusion of the dielectric function of air [5.26]. Further, we proposed that regions of the layer separate from the bulk a-Si matrix could be highly crystalline as well, depending on the annealing temperature and these regions could also be porous and metal contaminated, as the metal particles could act as seeds around which the crystalline silicon grows. This is depicted in figure 5.9.

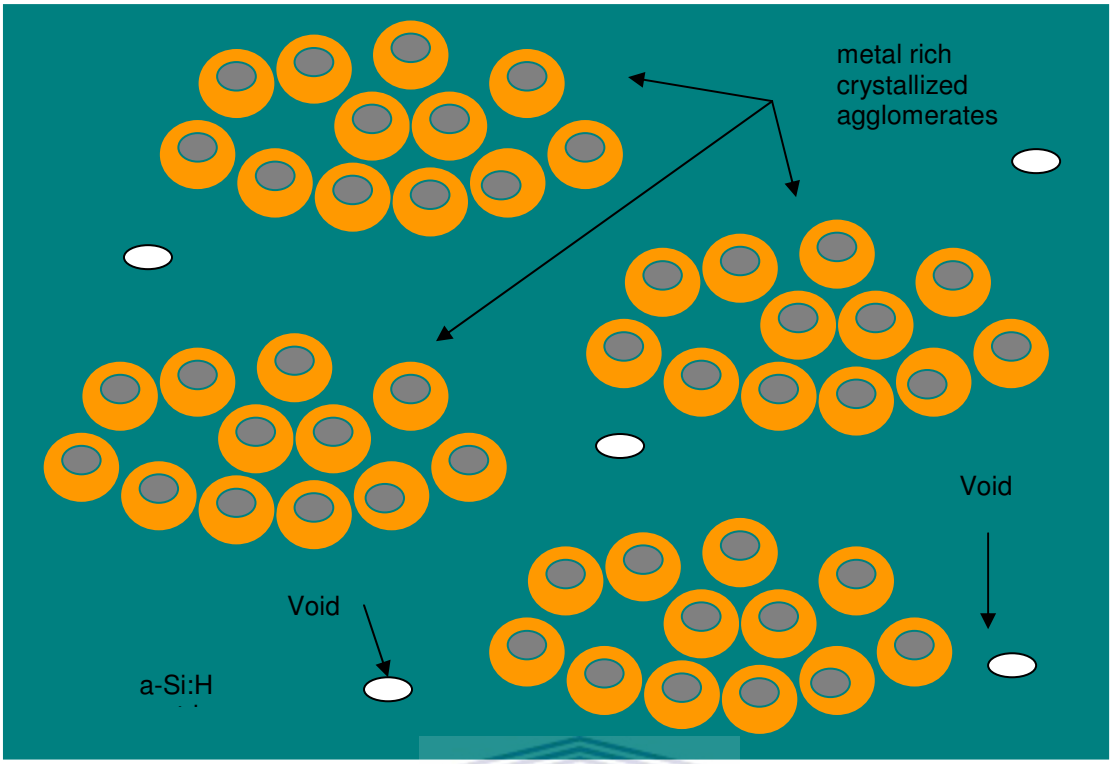

Figure 5.9 Possible distributions of crystalline regions over the film.

The dielectric functions of air, Al or Ni metal, and polycrystalline silicon [5.26] were mixed according to the Bruggeman effective medium approximation (EMA) to make up the mixtures [5.27]. The Bruggeman formula is used according to

$$0 = f_m \frac{\hat{\varepsilon}_{mix} - \hat{\varepsilon}_m}{\hat{\varepsilon}_{mix} + 2\hat{\varepsilon}_a} + f_p \frac{\hat{\varepsilon}_{mix} - \hat{\varepsilon}_p}{\hat{\varepsilon}_{mix} + 2\hat{\varepsilon}_p}, \text{ where} \qquad (5.1)$$

$$\hat{\varepsilon}_{mix} = \varepsilon_{mix} - i\varepsilon_{(mix)i},\ \hat{\varepsilon}_m = \varepsilon_{m(r)} - i\varepsilon_{m(i)},\ \hat{\varepsilon}_p = \varepsilon_{p(r)} - i\varepsilon_{p(i)} \text{ and } f_a + f_p = 1.$$

Here ε_m and ε_p are the complex dielectric functions of the matrix and the embedded particles respectively, while ε_{mix} is the complex dielectric function of the effective mixture. The subscripts *r* and *i* refer to the real and imaginary parts of the complex expression respectively. It should be emphasized that a simple a-Si fitting model which

considers a homogenous layer of material was totally incapable to simulate the spectra, as was a homogenous microcrystalline silicon layer using the EMA.

One of the main objectives was to develop a versatile model that could be used on both intrinsic a-Si, (doped) μc-Si and films that underwent the metal induced crystallization process. Three different regions of interest in the film can be identified during this process: the initial position of the metal layer, either on top of the a-Si:H or underneath it, and the bulk material. As the crystallization procedure normally involves a layer exchange mechanism, it is uncertain whether homogeneity across the depth of the film is retained. Therefore we postulated that a surface layer or substrate-interface layer where the metal was in contact with the a-Si:H, could differ appreciably in electronic and optical properties from the bulk of the material, after the annealing process and subsequent chemical etch. To that end in the computer program the film was virtually split into a surface, bulk and substrate-interface layer, as shown in figure 5.10, each containing the adapted model that is inclusive of a porous combination of a-Si, metal contaminated-polycrystallites and voids.

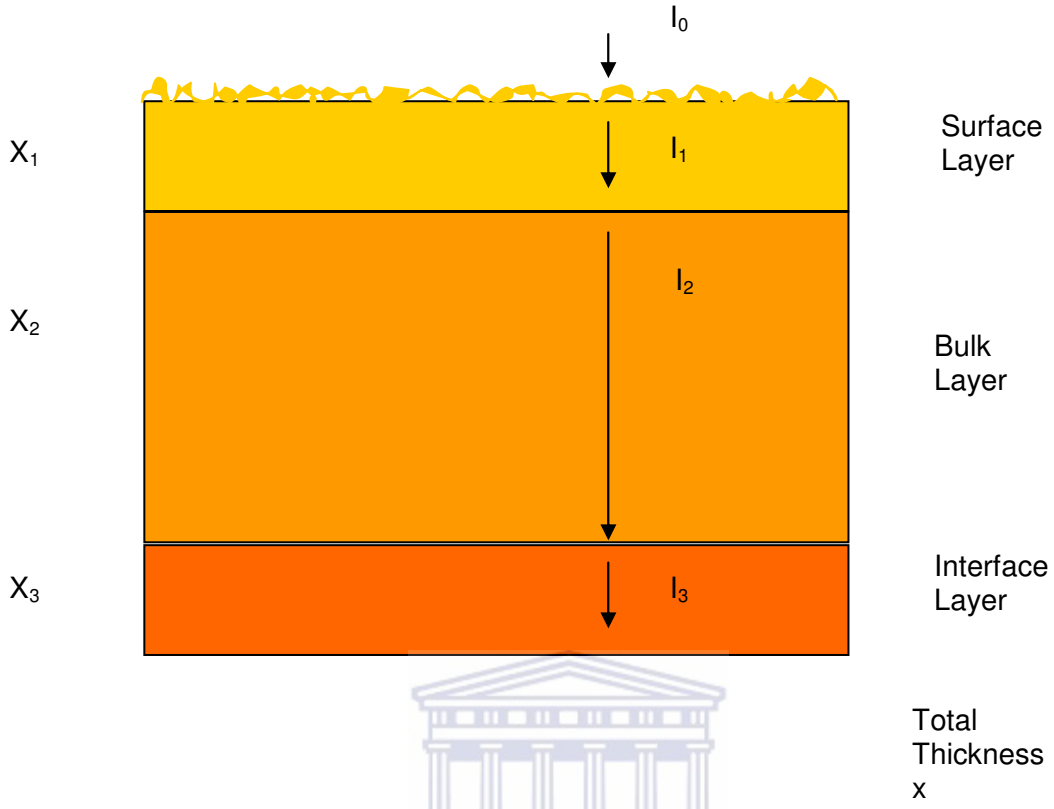

Figure 5.10 Film virtually divided such that absorption $\alpha_{tot} = \frac{\alpha_1 x_1 + \alpha_2 x_2 + \alpha_3 x_3}{x}$. Note that the original metal layer on top is etched off.

In the execution of the model the surface and substrate-interface layers were initialized to be roughly as thin as the Raman scattering depth of silicon layers, but the program was allowed to adjust the thickness of each of the three layers independently, and all the parameters for each layer to describe the region best, if any differences existed. If the film is virtually divided into three parts the absorption for the entire layer can be reconstituted by adding the weighted contribution of absorption for each layer by Beer-Lambert's Law [5.28].

From the initial fit parameters the program calculated the simulated R and T spectra together with the associated optical constants over the specified energy range. The

simulated spectra were then compared to the measured ones. The program then changed the initial fit parameters and calculated new R and T spectra, such that if the comparison with the measured spectra results in a smaller deviation then the program replaced the initial fit parameters. The iterative process was repeated until no further improvement of the deviation could be achieved. The goodness of fit value was expressed as the deviation of the simulated spectra from the measured spectra. The results of these fits were all in the 'acceptable' to 'good' categories.

It should be noted at this stage that intrinsic material constitute a less complex simulation, by removing the porous metal/crystalline particles from the simulation but retaining the voids to account for porosity, microcrystalline or amorphous films could be more accurately modeled with the three-layer system, as it does away with the assumption that the material is homogenous in depth.

5.3.4 Optical functions

The layer structure set-up allowed for the quantification for particles inside the host material, by virtue of the EMA. The crystalline regions were constructed with the expectation that metal contamination could exist. Figure 5.11 shows the amount of metal, expressed as a volume fraction of metal.

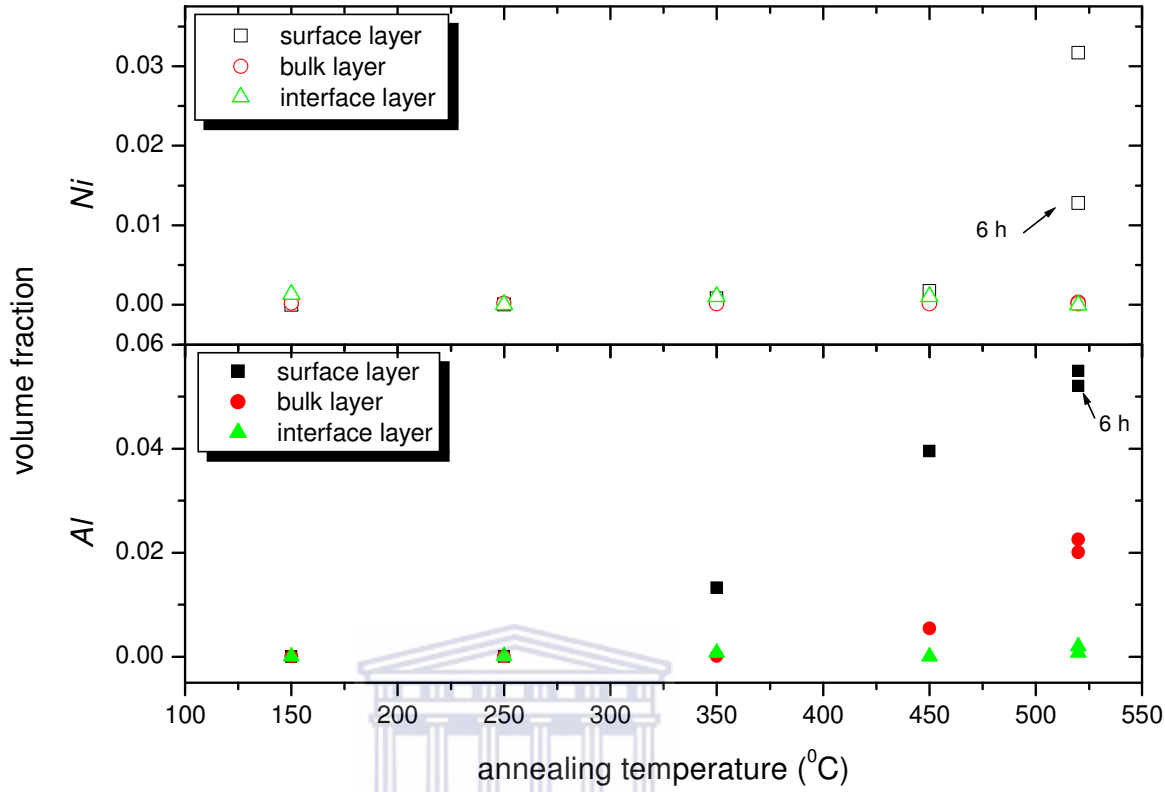

Figure 5.11 Metal quantification in the samples with the optical method.

The quantity of Al in the crystalline particles in the surface layer increases for the temperature where the onset of crystallization occurs, and then significantly for the annealing temperatures where full crystallization occurred, suggesting that the crystalline upper layer retain aluminium even after the chemical etch, not as a separate outer layer but as part of the silicon matrix in the form of metal aggregates. For the fully crystallized films the aluminium incorporation is also enhanced for the bulk layer compared to the films that remained amorphous at the lower annealing temperatures. This implies that the required amount of metal to complete the crystallization is achieved and that the diffusing species travelled across the thickness of the film. The electrical properties should thus be significantly influenced. It was also found that the nickel uptake is large in the surface

layer at the annealing temperatures where crystallization occurred. As mentioned previously the nickel probably exists in the form of nickel silicides. Overall the metal uptake or migration in the NIC series is much less than for the AIC series, both in the surface and bulk layers.

The refractive index dispersion for each film has been plotted in figures 5.12 and 5.13 for the AIC and NIC series respectively.

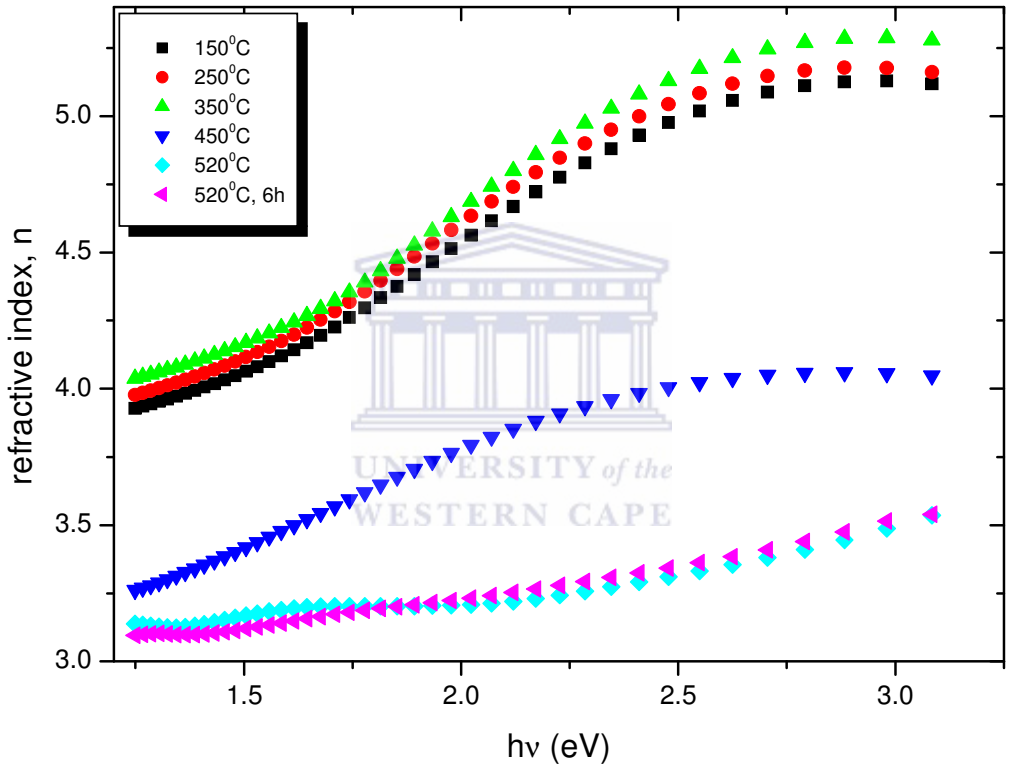

Figure 5.12 Refractive index dispersion for the AIC series films.

The behaviour of the material in terms of the refractive index over the energy range is similar for the annealing temperatures up to 350°C. Recall from the Raman spectroscopy spectra that the onset of crystallization for this series occurs at this annealing temperature. The behaviour of the refractive index drastically changes at 450°C, where crystallization

increases. The values are lower and the shape of the spectrum is also different. At the higher annealing temperatures of 520°C the refractive index spectra are completely different to those of preceding annealing temperatures, and have much lower values. The structural changes have completely changed the passage of light through the material.

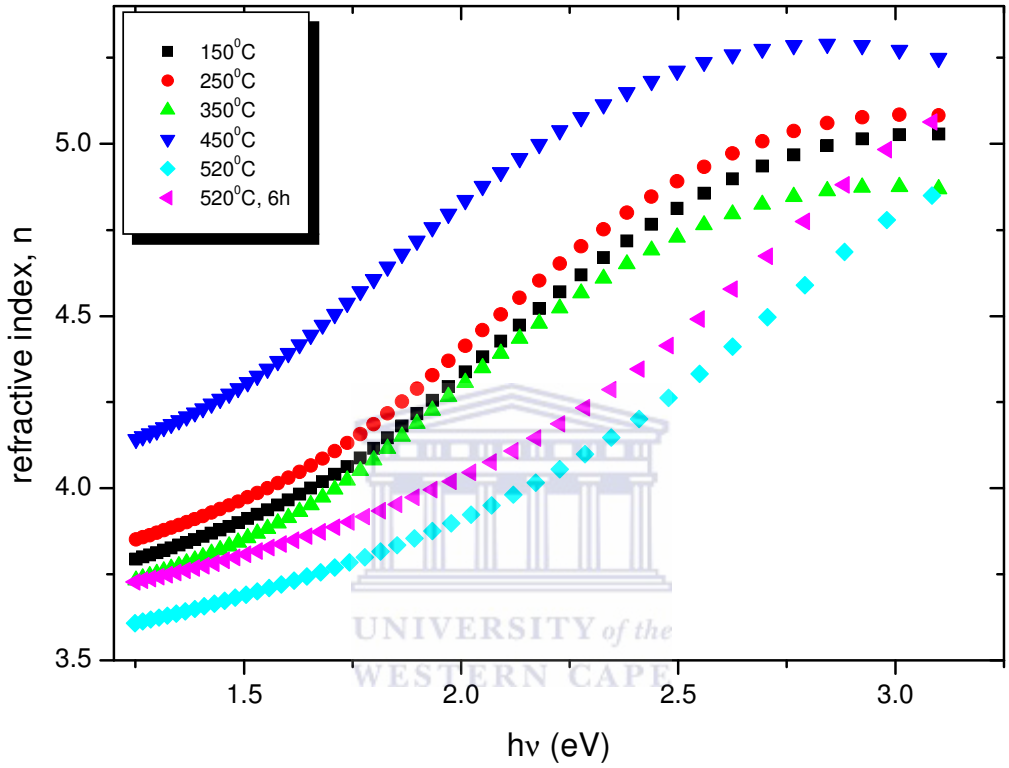

Figure 5.13 Refractive index dispersion for the NIC series films.

The general behaviour of the refractive index is not the same as that for the AIC series, since different crystallization mechanisms are involved. No general trend can be observed for the NIC series. At 450°C annealing temperature a general increase can be seen for the refractive index over the energy range. We could speculate that significant changes in refractive index could be linked to formation and migration of nickel-silicides in the films. For the crystallized material the values of refractive index over the enrgy range are lower than for preceding annealing temperatures, and the shapes of the curves are also

dissimilar. The optical density of the films expressed in terms of n_0, refractive index at infinite wavelengths, would have been a good indication of compactness of the films, and thus also possible defects. However, deviations of the shapes of the curves from those of a-Si:H, or even nc-Si:H during the plotting of $(1/n^2 - 1)$ vs $(h\nu)^2$, influence the applicability of straight line fits on the data range, especially the crystallized AIC films and the NIC film annealed at 450°C. For the NIC film the slope of the straight line is positive, which gives a non-sensical value of n_0. This rather shows that the composition of the material is different to conventional a-Si;H films and the structural changes have caused a different optical response of the material.

It was also possible to model the films such that the porosity of the film could be expressed as a percentage of voids contained within the silicon matrix for each virtual layer, shown in figure 5.14. For the AIC series the interface layer shows greatest porosity in general, which decreases until the film crystallizes; however, at full crystallization the porosity increases again. The bulk layer porosity increases upon crystallization but decreases again after the long anneal while the surface layer gets more compact upon crystallization. Here a full layer exchange between the metal layer and the thickness of silicon equivalent to that of the metal supposedly occurs, inducing complete crystallization of the film. For the NIC series the porosity of the films were also increasing most at the temperatures where the crystallization is complete for both surface and interface layers. The bulk layer porosity also slightly increases for the crystallized state.

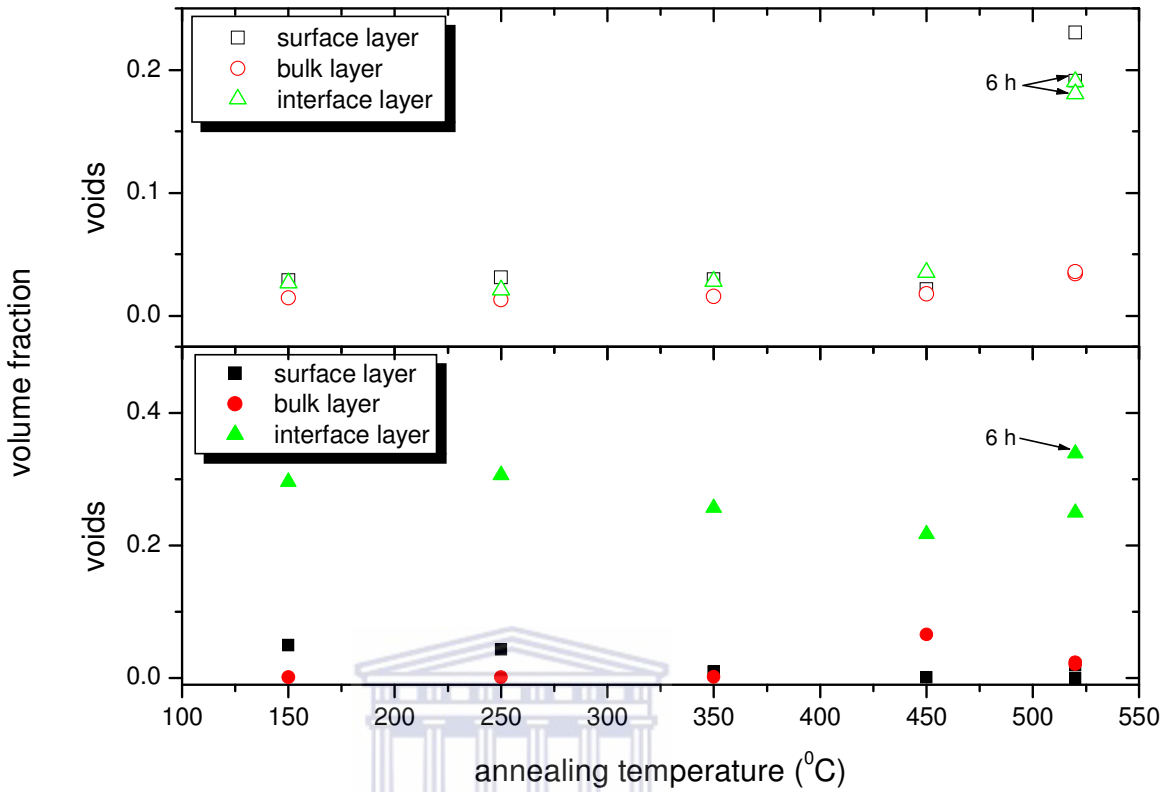

Figure 5.14 Film porosity for the AIC (bottom graph) and NIC (top graph) series'.

The porosity and metal incorporation should play an important role in determining the optical functions like refractive index and absorption across the film thickness. The powerful model built up with the software allows us now to investigate the different thickness regions of the film in detail, separately. In figure 5.15 the dispersion of the refractive index is shown in each of the three layers for the AIC and NIC films at 520°C, 6 hours. The refractive index for the surface and bulk layers compared to the interface layer are surprisingly low for the AIC sample, implying that the optically dense material is contained adjacent to the substrate. The refractive index in the bulk material is highest for the NIC sample compared to the other two layers. If one only considers the bulk

refractive index it is evident that the NIC film has higher values over the energy range, and the corresponding n_0 would be higher than that of the bulk of the AIC film. The n_0 gives an indication of the optical density.

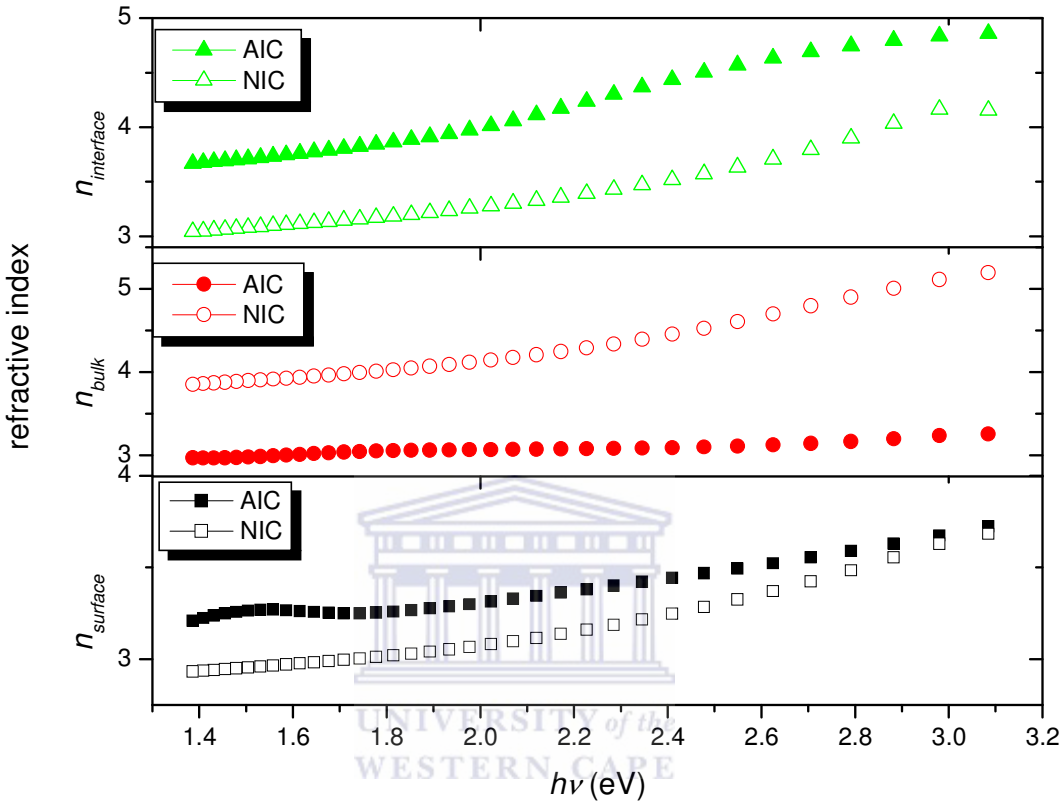

Figure 5.15 Refractive index dispersion in three virtual layers for AIC and NIC films at 520°C, 6 h anneal.

The effects of porosity and metal incorporation are rendered into the absorption coefficient, determined from UV-VIS spectrophotometry in the high energy region, while the sub-bandgap absorption is taken from the PDS data. The realistic description of the model eased the calibration of the PDS spectra with that obtained from the UV-Vis modeling.

The comparisons between the AIC and NIC series are shown in figure 5.16 which are plotted in the same range of absorption coefficient values. For each series only the data for temperatures where full crystallization occured are shown, together with standard absorption coefficient values of a-Si and c-Si [5.26]. It can be seen that the films exhibit lower absorption when they are crystallized compared to absorption by amorphous films. Higher sub-bandgap absorption is evident for the crystallized AIC sample compared the NIC sample. In addition, the sub-bandgap absorption for the 6 hour anneal at 520°C for the AIC sample is higher than for the NIC sample. This suggests increasing defect absorption.

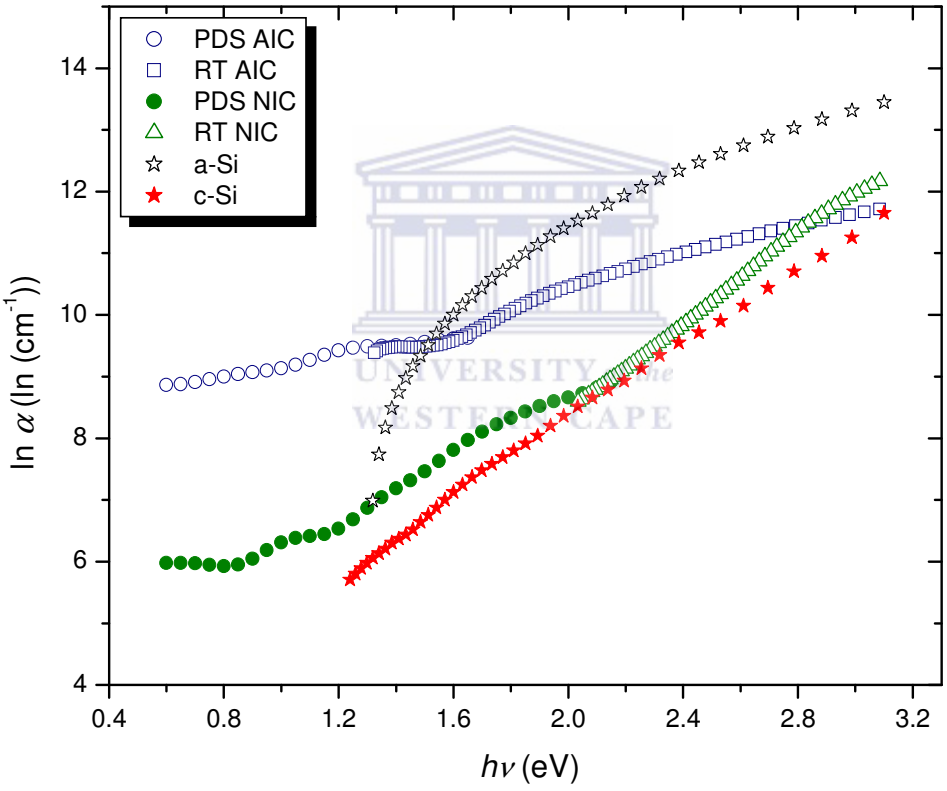

Figure 5.16 Absorption coefficient of AIC and NIC films at 520°C, 6 h anneal.

The Urbach energy value, which describes the width of the valence-band tail that can be related to the disorder affecting the material, was calculated from the PDS spectra after the scaling with RT absorption was performed, It is shown in figure 5.17.

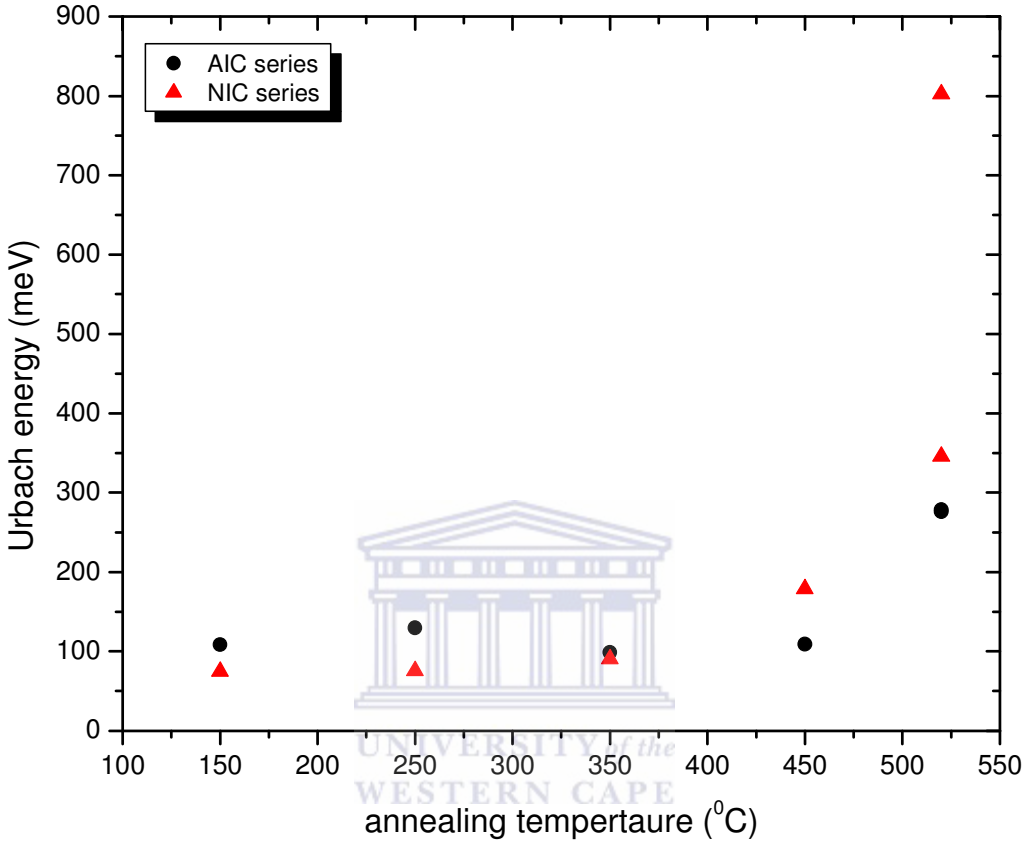

Figure 5.17 Urbach energy E_0 of AIC and NIC series.

Values for the films that were still amorphous or partially crystallized still exhibited the Urbach region in the absorption spectra, while for the fully crystallized films the spectra did not exhibit clear Urbach regions due to a reduced slope, and the spectra also did not display clear exponential tail regions. Nevertheless it was also attempted for the latter samples. The amorphous-like films in the AIC series show higher Urbach energy values than typical a-Si:H values of 50 meV, and decreases slightly for the partially crystallized films at 350 and 450°C; it then increases significantly for the crystallized films. The values also increase for the crystallized material in the NIC series. The Urbach Energy

can also be displayed in terms of the refractive index n, as an indication of optical density. We chose the value of n at 2 eV since n_0 gave non-physical values in some instances when plotting $[1/n^2-1)$ vs energy. The Urbach energy values are displayed in figure 5.18.

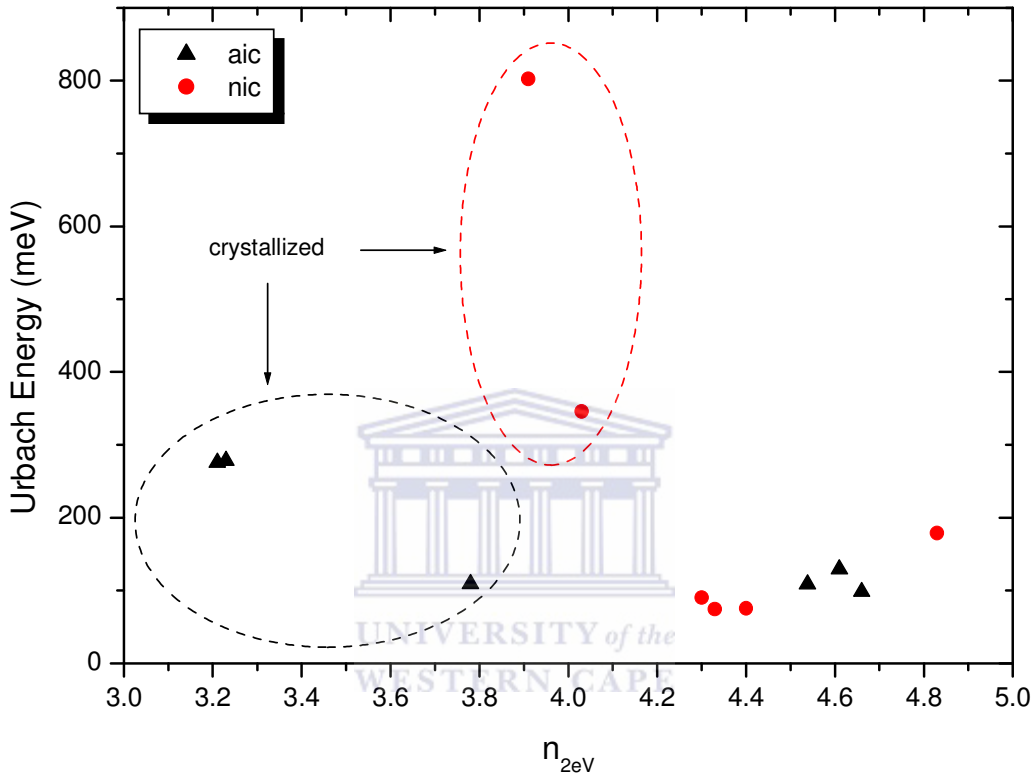

Figure 5.18 Urbach energy E_0 displayed in terms of n_{2eV} for the AIC and NIC series. (The curves are guides to the eye.)

Although no clear trend can be seen it appears as if the crystallized samples show some dependence of the Urbach energy on the optical density. Technically, crystallized material is ordered, but the preparation method could induce defect states. We postulate that the dependence in the graph imply that defects could be created by the incorporation of the metals in the silicon network, including the reaction of the hydrogen with the metals, while un-terminated dangling bonds could result in the creation of microvoids.

Further, hydrogen effusing from the film through the formation of voids or through cracks from inter-grain material could create defects. All these factors, including the defects caused by metal-silicide formation in the case of NIC, could play a role in the defect states in the mid band gap and remaining band tails. The bandgap value for c-Si is 1.1 eV, and it is expected that the Tauc plot should yield values close to that for the crystallized material. We expect that the difference in crystallization mechanisms and metal incorporation for AIC compared to silicide-formation in NIC will influence band gap values. The E_{04} value, where the absorption coefficient is 10^4 cm^{-1} was also determined and these were compared for the AIC and NIC series respectively in figure 5.19, together with the band gap calculated from the Tauc plot.

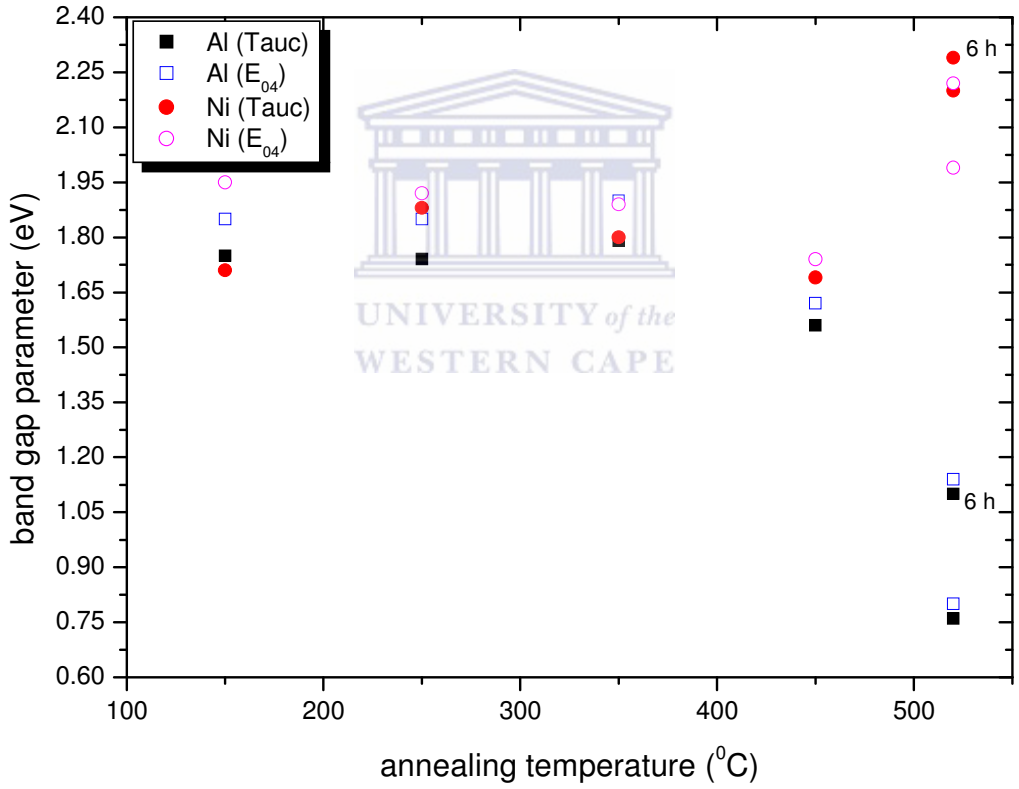

Figure 5.19 Band gap parameters for the AIC and NIC series.

For the AIC series the expected trend towards 1.1. eV was found, but surprisingly the NIC series show a significant difference to AIC, an increase rather than a decrease in band gap as the material crystallizes, probably due to the presence of the silicides, leading to a change in the resistivity of the silicon material.

Decades ago, it was found that the amorphous semiconductor dissolves in the metal film [5.4] and is transformed into the crystalline state. This is thought to be the case for Al in Si [5.29], which prefer to occupy interstitial sites [5.24], with most un-activated Al presumably segregated to the grain boundaries. This was implemented into our optical model. For our AIC series incomplete aluminium induced crystallization of a-Si:H was found for an annealing time of 30 minutes at a low annealing temperature of 350°C. With increasing annealing temperature the material was found to fully crystallize at 520°C for a relatively short annealing time of 30 minutes, which is an encouraging result. However, for Ni in Si it is thought that silicide formation occurs and that Ni_2Si is the migrating species in the a-Si and drives the crystallization process [5.30] with the silicide facilitating the formation of crystal silicon on the {111} faces of the $NiSi_2$ precipitates. The crystallization proceeds from these nuclei in the (111) direction. Further, it was suggested that Ni is a fast diffuser and possesses very low solubility in c-Si and bonds interstitially in c-Si. The Ni atoms are not strongly bonded to its Si neighbours [5.31]. For our NIC series it was found that nickel induces complete crystallization at the same annealing temperature of 520°C, and the 6 hours anneal also yields the same crystal grain sizes for both metals. Usually for a-Si:H, high hydrogen concentrations effect a decrease in refractive index and the density of the corresponding film. The density decrease is commonly explained by the appearance of microvoids. With the new three layer model it was found that porosity and metal contamination determined the optical functions of each layer, influencing the absorption of the whole film. Our improved model also achieved this successfully for the remaining a-Si films in the series. With onset of crystallization the slope of the absorption curves significantly decrease, and become similar to that of c-Si. However, the absorption in the visible range is not influenced as much as in the near infrared region. Increased metal incorporation of the AIC samples causes the bonding configurations for the silicon atoms adjacent to the Al atoms to become more metallic-

like compared to covalent bond types. According to the trend observed for the surface layer, the metal incorporation for the 520°C, 30 minutes anneal film is more than that of the 520°C, 6 hour anneal, suggesting that the longer annealing time has removed more of the metal from the film, or that out-diffusion of excess Al atoms took place. It is also known that Al forms a p-type dopant in the silicon [5.32]. In directly deposited poly-Si [5.23], effects of increasing doping were explained by the absorption of photon energy by free carriers in either conduction or valence bands due to the interaction with the impurities and also by the excitation of crystal lattice oscillations in the defect zone. We suggest a similar mechanism at work from our observations.

This has implications for the sub bandgap absorption also. For both metal series it was observed that for the crystallized films shorter annealing time has as result more metal uptake, in the surface layer, and the absorption in the subgap region is higher for the crystallized films than for the partially and uncrystallized films in both series. For the crystallized samples, the shorter annealing time also has as result more sub-gap absorption, and it is known that in PDS spectra all absorption processes are equally weighed. Generally, microscopic inhomogeneities like voids and columnar growths with high defect densities at the inner surfaces, together with quantum confinement effects [5.33] can contribute to the increased sub bandgap absorption of the deep defect states. Additionally, Ni creates deep acceptor levels above the valence band and below the conduction band in crystalline silicon [5.34], while Al creates shallow acceptor levels above the valence band [5.32]. Ni enhances carrier recombination while aluminium-related traps in polycrystalline Si was found to be responsible for electron recombination [5.35]. The PDS technique was shown to be sensitive for absorption by the defects which occur in the film. It should be noted that the majority of hydrogen has evolved at this annealing temperature and annealing time.

The band gap of the crystalline AIC films is in agreement by those found by Matsumoto *et al.* [5.24] and is in fact much lower than those for the NIC. It appears that two different mechanisms are at work for AIC and NIC; the resistivity of AIC films is very much lower than ordinary a-Si:H [5.24]. A plausible explanation for the general increase in band gap

values for the NIC series is that silicide formation is enhanced, increasing the resistivity of the material. Kumar et.al. [5.33] found that the Urbach energy, calculated from optical transmission measurements, increases with increase in Ni concentration, similar to our increase in Urbach edge calculated from PDS. The band gap in their case showed a smaller variation and was ascribed to confinement effects due to nanocrystallinity. We suggest that due to our introduction of porosity in the metal-containing crystalline regions in our optical model, we account more realistically for the effect of porous nickel silicides which may have formed in the film, which gives a truer reflection of the high band gap values for crystalline films in the NIC series. We also suggest that a possible oxidation effect in the AIC series cause compensation of the p-type material to some extent, although the films remain highly conductive. For both these series, the photoresponse is of the order of 10^0 for the crystallized material. However, for the NIC series, the crystallized material exhibit dark conductivity of the order of 10^{-3} $(\Omega cm)^{-1}$, while the AIC crystallized material exhibit dark conductivity of the order of 10^3 $(\Omega cm)^{-1}$. This suggests that the Ni as catalyst could produce material that is photosensitive to some degree, and if lower concentrations of metal are used some improvements could be made regarding the photoresponse. Another factor that could play a role in abetting this could be longer annealing times. For such highly conductive material, as they are in this experimental regime, a possible use could be window layers or by back-etching seed layers for further epitaxial growth.

5.4 CONCLUSION

The objective was to manufacture MIC silicon and describe its optical properties. The crystallization of a-Si:H, specifically protocrystalline silicon used in the attempted, but unsuccessful SPC experiment discussed in the previous chapter, was achieved with two types of metals as catalysts, the eutectic Al and non-eutectic Ni. In the previous chapter it was seen that using the short exposure time and annealing temperatures was insufficient to crystallize the protocrystalline silicon fully, while the same annealing conditions using metal catalysts achieved the desired result.

Extracting the optical properties of these two types of crystallized silicon using the analytical method for a homogenous semiconductor proved cumbersome and imprecise. Therefore an optical model making use of the EMA was successfully constructed that allowed for the addition of PDS spectra to absorption curves generated from RT measurements. It allowed for information on the defect states to be incorporated in the optical description of the material. Moreover, the optical model versatility enabled us to gain potential insight into different parts of the film, and besides the optical functions gives information about the thickness, structure and morphology. This allowed us to conclude that the AIC and NIC silicon have different optical properties, and that the crystallized films prepared by these two different catalysts can have different applications, as the low band gap AIC and high band gap NIC values imply.

We conclude from the results that lower concentrations of metal at longer annealing times, but yet shorter than conventional SPC, may improve the photoresponse of the material. Finally, the optical modeling can be seen as a useful, complementary tool to electron microscope and ion beam beam analysis techniques, for example.

REFERENCES

5.1 G. Radnoczi, A. Robertsson, H. T. G. Hentzell, S. F. Gong and M.-A. Hasan, J. Appl. Phys. 69 (9), (1991) 6394

5.2 W. Knaepen, C. Detavernier, R. L. Van Meirhaeghe, J. Jordan Sweet, C. Lavoie, Thin Solid Films 516 (15), (2008) 4946

5.3 O. Nast, T. Puzzer, L. M. Koschier, A. B. Sproul, S. R. Wenham, Appl. Phys. Lett. 73, (1998), 3214

5.4 D. Sigurd, G. Ottaviani, H. J. Arnal, J. W. Meyer, J. Appl. Phys. 45 (4), (1974) 1740

5.5 L. R. Muniz, C. T. M. Ribeiro, A. R. Zanatta, I. Chambouleyron, J. Phys.: Condens. Matter 19, (2007) 076206 1-16

5.6 S. Zhang, L. Pereira, Z. Hu, L. Ranieiro, E. Fortonato, I. Ferreira, R. Martins, J. Non-Cryst. Sol. 352, (2006) 1410

5.7 P. I. Widenborg, A. G. Aberle, J. Cryst. Growth 306, (2007) 177

5.8 www.mtheiss.com

5.9 K. Van der Werff, Utrecht University, private communication

5.10 E. Ullersma, PhD thesis, Utrecht University (1998)

5.11 H. Ohmi, K. Yasutake, Y. Hamaoka, H. Kakiuchi, Applied Physics Letters 91, (2007) 241901

5.12 Y. Z. Wang, O. O. Awadelkarim, Applied Physics A 70, (2000) 587

5.13 D. Stryahilev, F. Diehl, B. Schroder, M. Scheib, A. I. Belogorokhov, Phil. Mag. B 80, (2000) 1799

5.14 M. van Veen, PhD thesis, Utrecht University (2003)

5.15 M. D. Efremov, V. V. Bolotov, V. A. Volodin, S. A. Kochube, A. V. Kretinin, Semiconductors 36 (1), (2002) 102

5.16 B. D. Cullity, in 'Elements of X-ray Diffraction', Addison-Wesley, Reading, MA (1978)

5.17 Y. He, C. Yin, G. Cheng, L. Wang, X. Liu, G. Y. Hu, J. Appl. Phys. 75, (1994) 797

5.18 L. Pereira, H. Aguas, P. Vilarinho, E. Fortunato, R. Martins, J. Mat. Sci. 40,

(2005) 1387

5.19 R. Swanepoel, J. Phys. E: Sci. Instrum. 16, (1983) 1214

5.20 R. Swanepoel, J. Phys. E: Sci. Instrum. 17, (1984) 896

5.21 A. M. Bakry, A. H. El-Naggar, Thin Solid Films 360, (2000) 293

5.22 A. H. El-Naggar, A. M. Bakry, J. Phys.: Condens. Matter 11, (1999) 9619

5.23 Y. Laghla, E. Scheid, Thin Solid Films 306, (1997) 67

5.24 Y. Matsumoto, Z. Yu, Jpn. J. Appl. Phys 40, (2001) 2110

5.25 S. K. O'Leary, S. R. Johnson, P. K. Lim, J. Appl. Phys. 82 (7), (1997) 3334

5.26 Database of optical functions, Scout® software, based on data from literature

5.27 D. A. G. Bruggeman, Ann. Phys. 24, (1935) 636

5.28 K. J. Laidler, J. H. Meiser, in 'Physical Chemistry', second edition, Houghton Mifflin Company, Boston (1995)

5.29 K. Nakamura, M-A. Nicolet, J. W. Mayer, J. Appl. Phys. 46 (11), (1975) 4678

5.30 S. Young Yoon, J. Young Oh, C. Ok Kim, J. Jang, J. Appl. Phys. 84 (11), (1998) 6463

5.31 F. A. Ferri, A. R. Zanatta, I. Chambouleyron, J. Appl. Phys. 100, (2006) 094311

5.32 S.M. Sze, in 'Semiconductor Devices', John Wiley & Sons, New York (1985)

5.33 K. U. M. Kumar, R. Brahma, M. G. Krishna, A. K. Bhatnagar, G. Dalba, J. Phys.: Condens. Matter 19, (2007) 4962081 1-11

5.34 H. Kitagawa, S. Tanaka, H. Nakashima, M. Yoshida, J. Electr. Mat. 20 (6), (1991) 441

5.35 M. Rodot, J. E. Bouree, A. Mesli, G. Revel, R. Kishore, S. Pizzini, J. Appl. Phys. 62 (6), (1987) 2556

CHAPTER 6: SUMMARY

Silicon thin films on inexpensive substrates have contributed greatly to cost reductions in the electronics material market in the past decades. Once it was shown that hydrogenated amorphous silicon films could be doped the manufacturing of semiconductor devices from this material have greatly improved our quality of life in the form of photocopiers, flat panel displays, switching devices, and pertinently, devices such as solar cells. For the past twenty years great strides have been made in the development and implementation of newer generation materials such as nanocrystalline silicon in this industry. Deposition methods have been tailored and fine-tuned for even deposition of polycrystalline silicon thin films. However, these direct deposition methods yield small grains, and efforts have been undertaken to increase grain sizes for smooth, continuous films greater than the order of the thickness of the thin films. These include laser annealing and solid phase crystallization techniques of amorphous or hydrogenated amorphous silicon thin films. The metal induced method of crystallization has found great favour in the past few years for the formation of seed layers for further epitaxial growth or window layers in solar cells. Irrespective of its use, it is important to know the optical characteristics of such material. We have found that films that were crystallized with the most favoured metal, namely aluminum, yield deformed optical reflection and transmission spectra, when compared to spectra of amorphous or even nanocrystalline silicon thin films. There was therefore a need to develop a general technique to address these concerns, and assure that it could also be useful if another metal is used as crystallization catalyst. In this work a step-wise approach was used to arrive at a workable optical model for the thin films crystallized with the MIC technique. Thus, the result chapters reflect the evolution of the optical model to interpret the different types of silicon thin films.

In chapter 2 the experimental conditions for the preparation of the crystallized thin films are described. The analytical techniques used to characterize the films are explained in a short theoretical discussion for each method. Special attention was given to introduce the theory that is used to arrive at the analysis formulas for describing the functions,

refractive index and absorption coefficient of a solid material, and how it would relate to the methods employed in the software package used to analyse the data. The other methods of analysis included Fourier Transform Infrared Spectroscopy (FTIR) to investigate hydrogen bonding in the films, X-Ray diffraction and Raman scattering as structural characterizing tools. Photothermal deflection spectroscopy for sub-bandgap absorption and electrical characterization was further employed to describe the properties of the thin films.

In chapter 3 an intrinsic HWCVD set of films was used to showcase the applicability of effective media theory in the optical analysis nano/microcrystalline material. A model was built that incorporated reflection off rough surfaces, and crystallites in the amorphous matrix. The series of films were manufactured in a high growth rate regime, but the material was described as poor in properties and thus not useful for device application. The optical method constructed in this chapter suggested that the films were rather porous, as voids could be modeled in the overall matrix, and defining three different regions of interest where growth of crystal grains may be different. By using this model the UV-Vis technique offers a fast method of measurement for suspected porous materials that could have been modeled by the more expensive spectroscopic ellipsometry technique, which is not that commonly found in solid state laboratories compared to UV-VIS spectrophotometers.

In chapter 4 an initial comparative experiment with MIC was investigated by annealing intrinsic proto-Si:H without the metal catalysts. It was found that short-range order was retained, and the films did not crystallize during the short annealing times according to Raman scattering. Hydrogen bonding was affected, and a simple one layer a-Si approach was insufficient to successfully model the optical properties from the degraded reflection and transmission spectra. The optical model developed in chapter 3 was thus applied and in turn yielded satisfactorily results. The optical modeling confirmed the ordered nature of the films, and could detect small crystallites that could not be detected by Raman scattering and XRD. This showed the sensitivity of the optical technique and the model

promises to be a valuable aid in addition to the standard techniques for crystallite detection in silicon.

In Chapter 5 the MIC films were investigated. Two metal catalysts, Al and Ni, produced polycrystalline silicon thin films after annealing at 520°C. By modifying the optical model described in chapter 3 the metal was included in the virtual thin films with the EMA. From the application thereof, besides the crystallinity and porosity, the spread of metal or their silicides through the film could be tracked, whether the substrate-interface region or the surface region are richer in metals/metal-silicides. This highlights the use of such a model, as techniques such as ion beam analysis and electron microscopy are time intensive, while an optical measurement like this is fast and with a normal desktop computer can model such spectra in seconds, or minutes at most, depending on the quality of the spectra. The optical modeling can be used as a precursor measurement before actual crystallinity measuring techniques such as XRD, Raman spectroscopy or TEM measurements are performed. The model could also be modified such that various other materials could be included in the EMA assembly and modeled.

Besides these advantages, the inclusions of known impurities and materials in the model can only yield more realistic and accurate optical functions. Suggested further work is electron microscope studies such as HR-TEM and EELS on the films. The optical model that extracts the optical function for the MIC films was presented at the 23rd International Conference on Nano and Microcrystalline Semiconductors, and a written paper was submitted in anticipation for publication in the conference proceedings.

APPENDIX A

A1. Defining materials from the database.

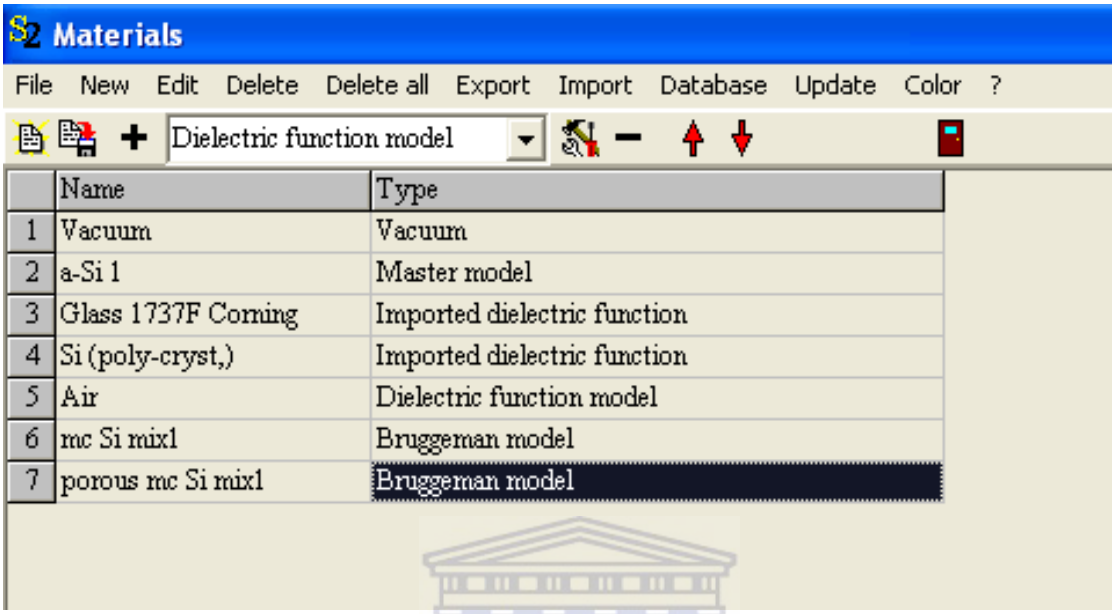

	Name	Type
1	Vacuum	Vacuum
2	a-Si 1	Master model
3	Glass 1737F Corning	Imported dielectric function
4	Si (poly-cryst,)	Imported dielectric function
5	Air	Dielectric function model
6	mc Si mix1	Bruggeman model
7	porous mc Si mix1	Bruggeman model

A2. Defining the susceptibilities of an amorphous semiconducting material.

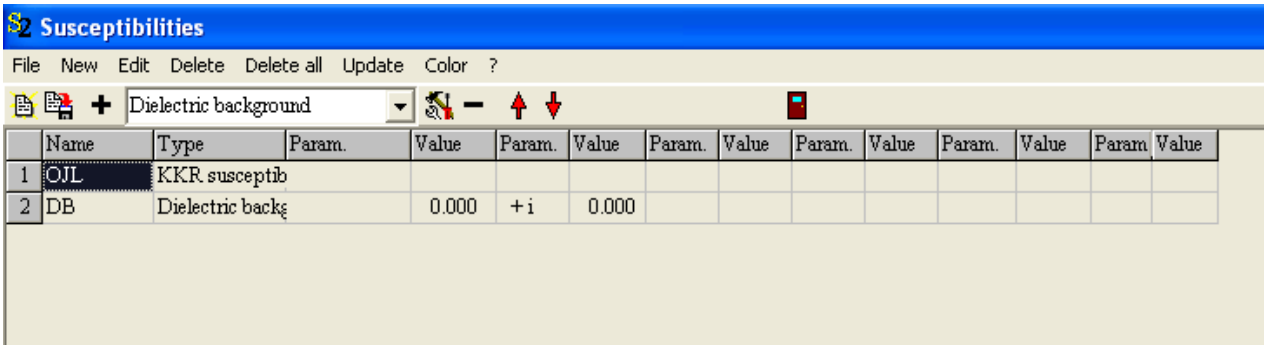

	Name	Type	Param.	Value	Param.	Value	Param.	Value	Param.	Value	Param.	Value	Param.	Value	Param.	Value
1	OJL	KKR susceptib														
2	DB	Dielectric backg		0.000	+ i	0.000										

A3. Defining the layer stack.

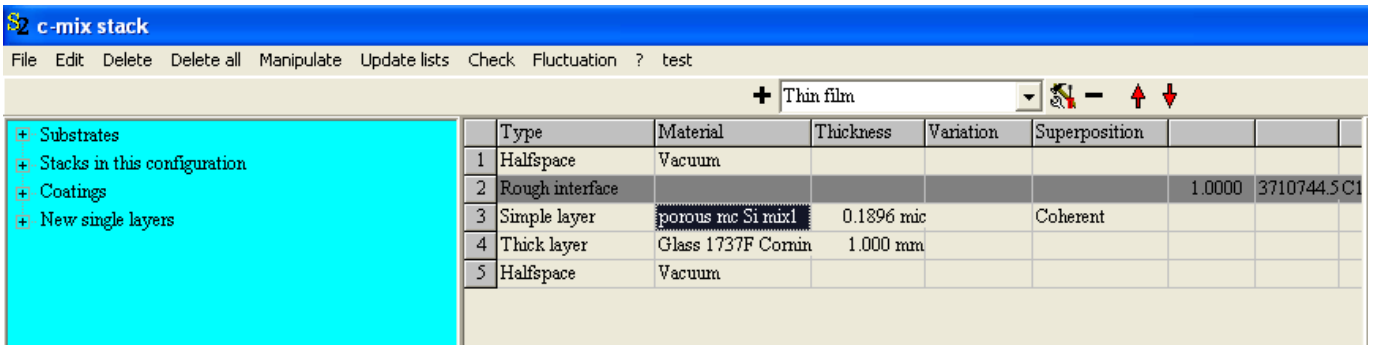

A4. Numerical values of fit parameters returned after modeling.

Fit parameters

File New Edit Delete Delete all Slider Fit on grid Limits from sliders Update ?

All

	Value	Name	Variation	Low limit	High lim	Factor	Digits
1	1.0000	Stack 1 Layer 2: Roughness parameter C1	Downhill simplex	0.0000	1.0000	1.0000	4
2	3710744.5000	Stack 1 Layer 2: Roughness parameter C2	Downhill simplex	1.0000	1000000(	1.0000	4
3	189.6218	Stack 1 Layer 3 porous mc Si mix1: Layer thickness	Downhill simplex	0.0000	3000.00(	1000.0000	4
4	7.1169	a-Si 1:a-Si 1: IB: Mass	Downhill simplex	0.5000	100.000	1.0000	4
5	18186.7520	a-Si 1:a-Si 1: IB: E0	Downhill simplex	1.0000	100000.0	1.0000	4
6	0.5381	a-Si 1:a-Si 1: IB: Ratio gamma_c/gamma_v	Downhill simplex	0.5000	5000.00(	1.0000	4
7	1328.1530	a-Si 1:a-Si 1: IB: gamma_v	Downhill simplex	50.0000	5000.00(	1.0000	4
8	0.3947	mc Si mix1:Volume fraction	Downhill simplex	0.0000	1.0000	1.0000	4
9	0.0266	porous mc Si mix1:Volume fraction	Downhill simplex	0.0000	1.0000	1.0000	4

A5. Dielectric function output.

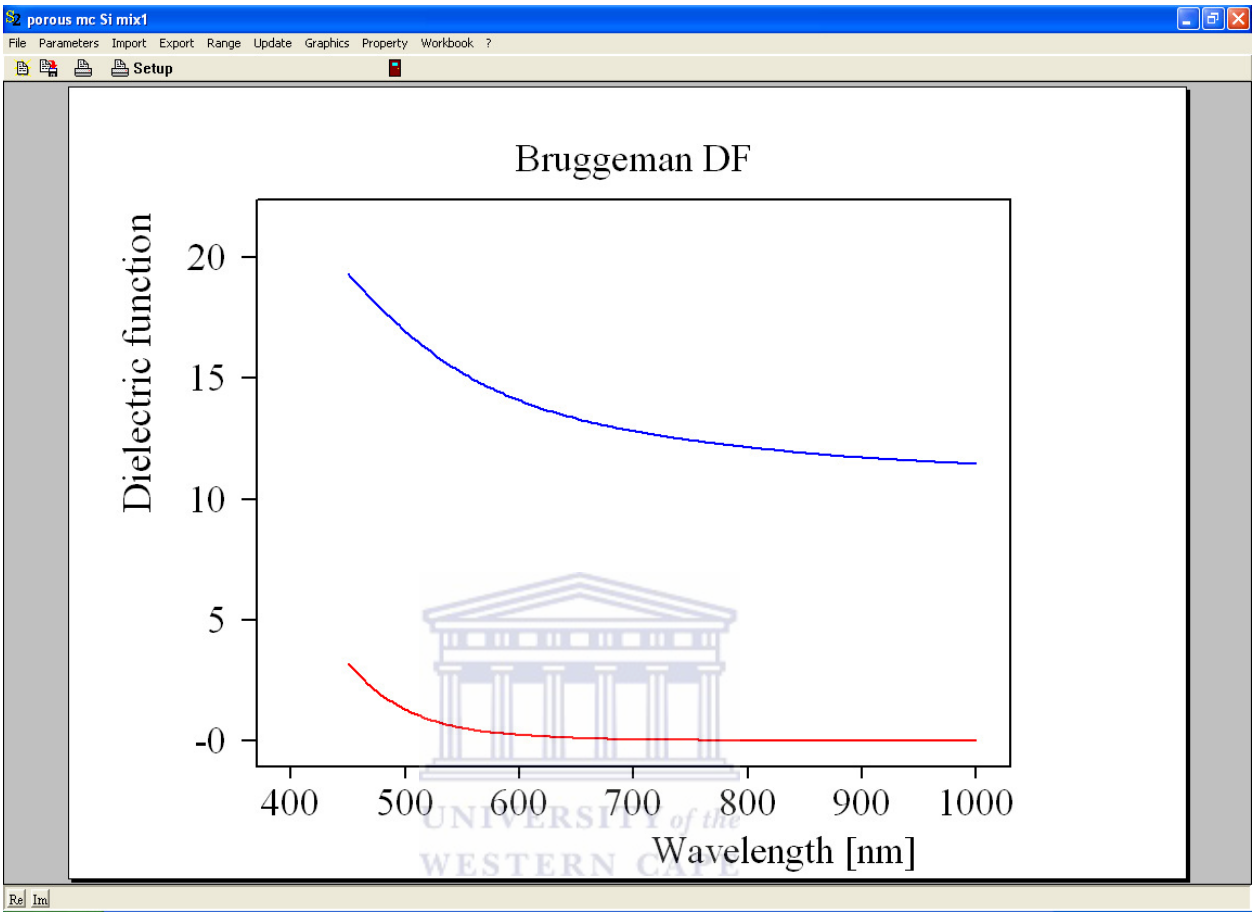

A6. Refractive Index output.

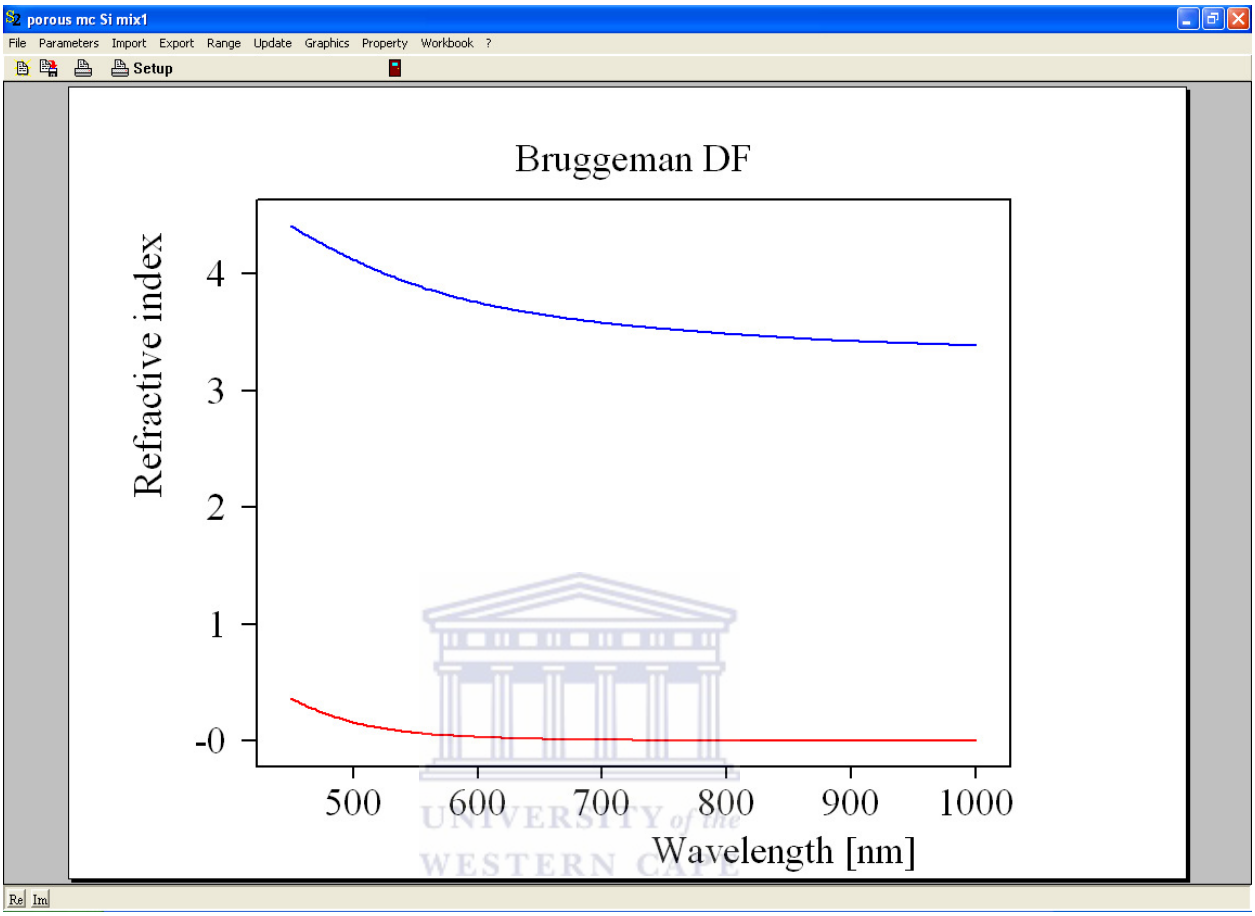

A7. Absorption Coefficient Output.